Physics | Lancaster University

Dilute Nitride GaInNAsSb for Next Generation Optical Communications

Author:

Xiao Collins

Supervisor:

Dr Andrew Marshall

Thesis submitted for consideration for the award of the degree of Doctor of Philosophy

December 7, 2020

Declaration of Authorship

This thesis has not been submitted in substantially the same form for the award of a higher degree. This thesis is the result of my own work except where the contributions by others are specifically stated. Excerpts of this thesis have been presented and published in the following conferences and academic journals respectively:

X. Collins, K. Nunna, R. Yanka, R. Pelzel, A. R. J. Marshall. "Dilute Nitride GaInNAsSb for High Speed 1.55 µm Photodiodes" *UK Semiconductors*, Sheffield, UK (2019) (oral presentation)

A. P. Craig, M. Jain, L. Meriggi, T. Cann, A. Niblett, X. Collins, A. R. J. Marshall. "Extended short-wave infrared linear and Geiger mode avalanche photodiodes, based on 6.1 Å materials" *Applied Physics Letters*, vol. 114, 2019.

X. Collins, A. P. Craig, T. Roblin and A. R. J. Marshall. "Impact ionisation in $Al_{0.9}Ga_{0.1}As_{0.08}Sb_{0.92}$ for Sb-based avalanche photodiodes" *Applied Physics Letters*, vol. 112, 2018.

X. Collins, A. P. Craig, T. Roblin and A. R. J. Marshall. "Impact ionisation in $Al_{0.9}Ga_{0.1}As_{0.08}Sb_{0.92}$ for Sb-based avalanche photodiodes" *UK Semiconductors*, Sheffield, UK (2017) (oral presentation)

Acknowledgements

First, I would like to thank my supervisor Dr Andrew Marshall for his knowledge, guidance and trust throughout the project. He has been the foundation of this study and I am incredibly grateful to have him as supervisor.

This work would not have been possible without the funding and support of IQE. In particular, I would like to thank Bob Yanka and Dr Kalyan Nunna for the valuable discussions and MBE growth of the samples.

I would also like to thank Dr Adam Craig whose support, assistance and guidance in this project has helped far beyond any expectations in both the research and writing aspects of this thesis.

I am also grateful to Cardiff University and Dr Shiyu Xie for assisting me to measure the bandwidth of my samples on their equipment.

The support staff within the department are deserving of much praise, including Dr Kunal Lulla and Dr Christopher Somerton for providing an excellent cleanroom facility which I spent countless hours in. Steve Holden, for all of his help with procurement and supplying the project. Shonah Ion, Stephen Holt, Robin Lewsey and Rupert Prudom for all the technical support.

I would also like to thank the friends and officemates who have helped throughout, this includes but is in no way limited to: Ofogh Tizno, Laura McIndo, Veronica Letka, Alex Jones, Theo Noble, Andrew Guthrie, Joshua Chawner, Ash Jennings, Andrew Bainbridge and Kat Mamic.

Finally, I would like to thank my family for their endless support and love.

Abstract

Current technology for the light detection in telecommunication revolves around InGaAs based on InP substrates. However, there is interest in switching to GaAs substrates to take advantage of the cheaper and larger substrates as well as the lattice-matched $Al_xGa_{1-x}As$ material system. Therefore, this thesis reports on the use of the dilute nitride alloy GaInNAsSb lattice matched to GaAs that can detect at wavelengths important to telecommunications such as 1.55 µm.

Molecular beam epitaxy (MBE) was used to grow GaInNAsSb p-i-n and n-i-p photodetectors on GaAs substrates with the lowest band gap reaching 0.64 eV, far below the necessary band gap required for detection at 1.55 µm (0.8 eV) and that for InGaAs (0.74 eV). However, due to the high defect concentration typically found in dilute nitride alloys, a post-growth thermal anneal was applied to the samples which has the effect of blueshifting the band gap by approximately 40 meV. The effect of a post-growth anneal on the band gap, dark current, unintentional doping concentration and quantum efficiency is investigated in order to find the most optimal temperature. This temperature is found to be related to an intrinsic dopant type switch in the GaInNAsSb as one of the samples with the lowest dark current density (2.2 mA cm^{-2} at −5 V) is one that is annealed at 735 °C, just before a switch in intrinsic type from n-type to p-type. This is further investigated with a much narrower annealing range centred around 735 °C. While this narrow annealing range did not result in a consistent type switch temperature for all samples, admittance spectroscopy indicated a large increase in a p-type defect concentration demonstrating the potential for the anneal to worsen the performance of the photodiode at sufficiently high temperatures. Furthermore, it was found that annealing at temperatures close to 730 °C results in a much better photodetector than as-grown devices, which can be quantified by comparing the quantum efficiency at 1.55 µm where the annealed sample reaches 38% as compared to the 3% in the as-grown device.

The 3 dB bandwidth was measured on the most optimally annealed photodetectors. In this measurement, the highest bandwidth reached is 9.2 GHz at −18 V which is limited

by the resistance of the photodetector and can be further improved using Ohmic contacts with a lower resistance.

Finally, a discussion on the integration of GaInNAsSb with AlGaAs in a separate absorption and multiplication avalanche photodiode (SAM APD) is held. Impact ionisation in GaInNAsSb and its effect on noise is discussed, as well as the design of a SAM APD with a very thin AlGaAs multiplication layer of 50 nm. In this study, such SAM APDs are grown with a GaAs absorber instead of GaInNAsSb to allow for any corrections required in the important charge sheet layer, however in future studies GaInNAsSb can be used instead of GaAs as an absorber.

Contents

List of Figures

List of Tables

Chapter 1

Introduction

In long-haul optical fibre communications, typical operation lies within two windows of minimal dispersion in silica optical fibres, 1.31 and 1.55 µm. Designing a photodiode for the latter wavelength requires an absorbing semiconductor with a maximum band gap of 0.8 eV. Commercial detectors are designed using $In_{0.53}Ga_{0.47}As$, hereafter referred to as InGaAs, as its low band gap of 0.74 eV provides large amounts of detection at 1.55 µm. Furthermore, the growth of InGaAs is relatively uncomplicated and the production of InGaAs devices with low dark current and high depletion width is achievable. This makes it highly suited to near-infrared detection up to 1.7 µm.

This alloy fraction of InGaAs is lattice-matched to InP, so bulk layers of InGaAs can be epitaxially grown on InP substrates defect free. However, InP substrates are, in comparison, smaller and more expensive than other substrates such as GaAs. For instance, a 4″ diameter InP substrate is less than half the area of a 6″ diameter GaAs substrate. Switching to a GaAs-based photodetector could therefore lead to cheaper and more mass producible telecommunication receivers. Significantly, an absorber lattice matched to GaAs could also take advantage of the $Al_xGa_{1-x}As$ material system either in the form of highly reflective distributed Bragg reflecting (DBR) mirrors or as a multiplication layer in a separate absorption and multiplication avalanche photodiode (SAM APD). GaAs/AlAs DBR mirrors are easily grown by MBE and allow for a much higher reflectivity than what is achievable on InP, therefore improving the quantum efficiency of the detector[2, 3, 4]. Furthermore, AlGaAs multiplication layers are capable of much thinner widths as compared to currently incumbent AlInAs layers resulting in very low noise operation [5]. This can be achieved as long as there is an absorber that can be lattice matched to GaAs and epitaxially grown defect free on GaAs substrates.

It was discovered with the addition of dilute amounts of nitrogen into the GaAs,

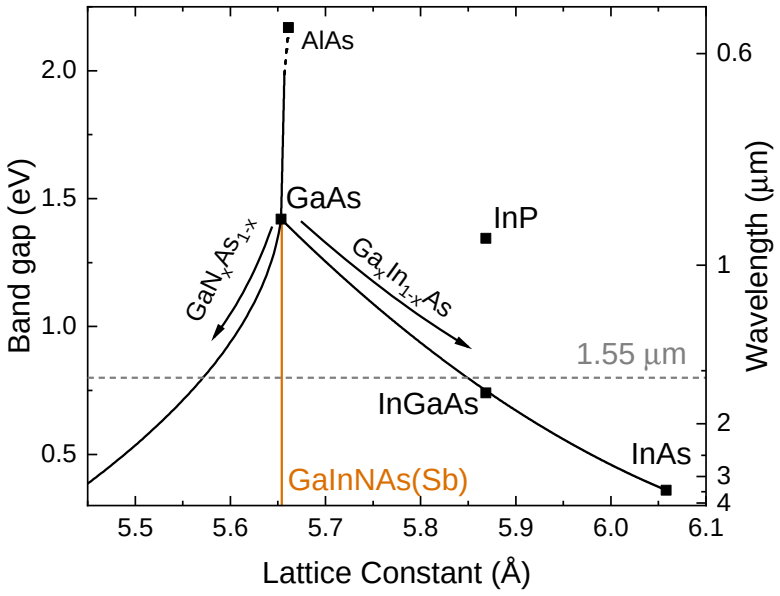

Figure 1.1: The addition of In and N into GaAs both reduce the band gap and can compensate the strain introduced by the complementary atom. The grey dashed line indicates 0.8 eV, materials with band gap below this energy will be able to detect the wavelength 1.55 µm.

the band gap dramatically decreases. By counterbalancing the tensile strain introduced by the small nitrogen atom with the larger atoms of indium and antimony, which in turn reduce the band gap further; the dilute nitride alloy can remain lattice matched to GaAs. With sufficient concentrations of nitrogen and indium, a detector can be fabricated capable of comparable absorption properties to InGaAs.

However, the process of adding nitrogen into the crystal structure is not trivial. The increased incorporation of nitrogen strongly decreases the optical qualities of the material due to the formation of non-radiative defects which are encouraged to form not only from nitrogen related defects but the low growth temperature required for reasonable nitrogen incorporation [6].

Past studies have shown improvement in quality from thermally annealing the dilute nitride alloy which are linked to the reduction of the defect concentration [7], however the application of the post-growth anneal also results in the blueshift of the band gap [8]. This anneal is therefore acting against the incorporation of nitrogen and could result in no longer being able to detect the crucial wavelengths required for long haul telecommunications.

The aim of this study is to characterise GaInNAsSb p-i-n and n-i-p devices for their suitability to function as photodetectors operating at a wavelength of 1.55 µm for the purposes of "last mile" fibre optic telecommunications. For such an application, the

photodetector should possess a band gap less than 0.8 eV and should be capable of operating at speeds of 10 Gbit/s which corresponds to a 3 dB bandwidth of at least 5 GHz. Furthermore, in order to compare with typical InGaAs photodiodes, the dark current should not be significantly above typical maximum values for dark current in incumbent commercial photodiodes. This presents a target dark current of 10 nA.

Chapter 2 summarises the background theory behind the dilute nitride photodiodes fabricated in this study along with various important parameters that are measured and are in used in quantifying the photodiodes. Chapter 3 provides a review of literature surrounding detectors that are capable of detection at 1.55 µm from the well-studied InP material system to previous advances in dilute nitride on GaAs detectors. It also discusses various material properties of the dilute nitride. Chapter 4 outlines the fabrication of the devices used in this study along with the methods of characterisation.

Chapter 5 includes a range of optical measurements undertaken on the GaInNAsSb samples including the band gap, absorption coefficient and quantum efficiency of the samples. The effect of the anneal on the band gap and the quantum efficiency is addressed and shown to be vitally important to GaInNAsSb photodiodes. The electrical properties of the GaInNAsSb photodiodes is discussed in chapter 6 with the impact of annealing on the dark current, unintentional doping concentration and the intrinsic type. Furthermore, the most optimal devices of the study are selected for additional processing into devices suitable for high speed measurements and the bandwidth of these devices are measured. A complete summary of the results of chapters 5 and 6 are detailed in chapter 7 with a discussion on the design process behind each campaign. Finally, the possibility of developing a SAM APD by using AlGaAs as the multiplication layer and GaInNAsSb as an absorber layer is discussed in chapter 8 with the impact ionisation present in GaInNAsSb detectors.

Chapter 2

Background Theory

2.1 Dilute nitrides

Despite the band gap of GaN (3.4 eV) being much larger than the band gap of GaAs (1.4 eV), the addition of small amounts of nitrogen to GaAs dramatically reduces the band gap of the alloy. This is caused by the addition of an impurity level which causes a splitting of the conduction band into two separate bands, E_- and E_+. The energy level of E_- is considered to be the new band gap of the dilute nitride. With approximately 1.5% nitrogen fraction or less, this can be modelled by an abnormally large band gap bowing parameter of 18.4 eV in GaAsN. However, beyond this concentration, the band gap is better described with the band anti-crossing (BAC) model. This is achieved by assuming the interaction of the conduction band and the nitrogen level can be treated as a perturbation. Therefore, the effect of the interaction is calculated from [9]:

$$\begin{vmatrix} E - E_M & V\sqrt{y} \\ V\sqrt{y} & E - E_N \end{vmatrix} = 0 \tag{2.1}$$

E_N is the energy of the nitrogen impurity level with respect to the valence band, E_M is the band gap of the nitrogen free alloy, V is the interaction potential between the bands and y is the nitrogen alloy fraction. The two energy levels created by the impurity can be calculated using equation 2.2.

$$E_\pm = \frac{1}{2}\left((E_N + E_M) \pm \sqrt{(E_N - E_M)^2 + 4V^2 y}\right), \tag{2.2}$$

Both V and E_N are dependent on the indium content of the alloy, as given by Vurgaftman et al. [10] for $Ga_{1-x}In_xNAs$.

$$E_N(x) = 1.65(1-x) + 1.44x - 0.38x(1-x) \tag{2.3}$$

$$V(x) = 2.7(1-x) + 2.0x - 3.5x(1-x) \tag{2.4}$$

The effect of the antimony on the band gap is discussed by Aho et al. [11] where it is incorporated into E_M since it has been verified that Sb does not have an appreciable effect on the BAC parameters [12]. The In and N concentrations required to reach a range of band gaps are shown on figure 2.1.

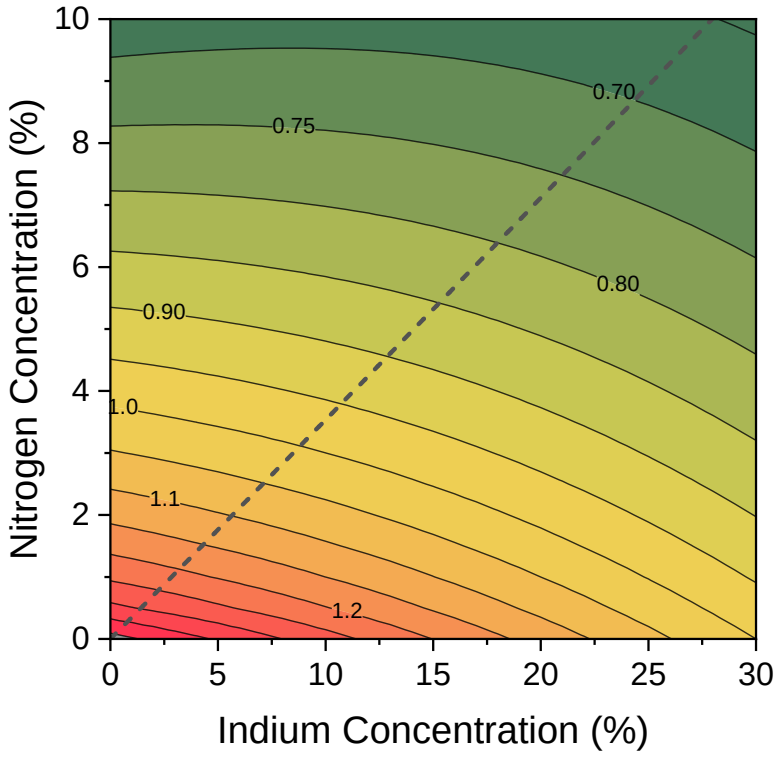

Figure 2.1: The achievable band gaps with different concentrations of In and N for GaInNAs. The dashed line indicates the ratio required to remain lattice matched to GaAs.

In order to remain lattice matched to GaAs and operate at 1.55 µm, a nitrogen concentration of 6.4% and 20% In is required to remain lattice matched to GaAs. The lattice matching condition is calculated by assuming GaInNAs obeys linear Vegard's law, so that the lattice constant of $Ga_{1-x}In_xN_yAs_{1-y}$ (a(GaInNAs)) is calculated by equation 2.5. However, Vegard's law only remains true when arsenic atoms are substituted for nitrogen atoms so that it is only in group V lattice sites. Deviations from Vegard's law are observed to occur when there is a significant concentration of interstitial nitrogen [13].

$$a(\text{GaInNAs}) = a(\text{GaAs})(1-x)(1-y)+a(\text{GaN})(1-x)y+a(\text{InAs})x(1-y)+a(\text{InN})xy \quad (2.5)$$

Figure 2.1 is plotted without considering the addition of Sb. If Sb is incorporated than the required concentrations of In and N are lower as Sb also works to reduce to band gap of the alloy.

2.2 Photodiodes parameters

2.2.1 Dark current mechanisms

The dark current in a photodiode is the current that is flowing through the photodiode without any source of illumination present. Minimising the dark current is highly preferable in a photodiode in order to increase the signal to noise ratio. The dark current can typically originate from four sources: diffusion, Shockley-Read-Hall (SRH), tunnelling and surface currents.

Diffusion current

Diffusion currents are caused by the thermal generation in the n and p regions which diffuses to the internal electric field leading to dark current.

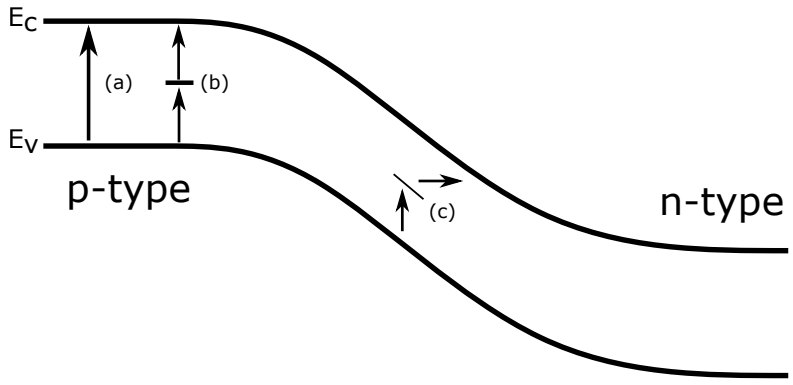

Figure 2.2: A schematic representation of some dark current mechanisms in a reverse biased p-i-n junction. Adapted from Razeghi and Rogalski [1]. Mechanism (a) represents diffusion currents, (b) trap assisted thermal generation and (c) trap assisted tunnelling.

Diffusion current in a p^+-n junction is described by equation 2.6 [14], where D_p is the hole diffusion coefficient, τ_p is the minority carrier lifetime of the hole, n_i is the intrinsic carrier concentration and N_D is the donor concentration.

$$J = q\sqrt{\frac{D_p}{\tau_p}}\frac{n_i^2}{N_D} \propto T^3 \exp\left(-\frac{E_a}{k_B T}\right) \tag{2.6}$$

Despite the injection of holes from the p-side to the n-side causing the diffusion current, the magnitude is determined by the properties of the n-type side such as: N_D and τ_p [14]. The same is true in the case of a heavily doped n-type layer:

$$J = q\sqrt{\frac{D_n}{\tau_n}}\frac{n_i^2}{N_A} \propto T^3 \exp\left(-\frac{E_a}{k_B T}\right) \tag{2.7}$$

The process has a significant temperature dependence due to the n_i^2 term which is shown on equation 2.8.

$$n_i^2 \propto T^3 \exp\left(-\frac{E_a}{k_B T}\right) \tag{2.8}$$

Where T is the temperature of the photodiode and E_a is an activation energy of the process which should be approximately equal to the band gap (E_g). Typically, the effect of the T^3 is not significant compared to the exponential and is subsequently ignored.

Shockley-Read-Hall generation

In SRH generated dark current, electrons are allowed to transition from the valence to the conduction band by a trap state positioned in the band gap caused by a defect in the crystal structure. The generation rate is given by:

$$U = \frac{\sigma_n \sigma_p v_{th} N_t (pn - n_i^2)}{\sigma_n \left[n + n_i \exp\left(\frac{E_t - E_i}{kT}\right)\right] + \sigma_p \left[p + n_i \exp\left(\frac{E_i - E_t}{kT}\right)\right]} = -\frac{n_i}{\tau_g} \tag{2.9}$$

where σ_n and σ_p are the electron and hole capture cross-sections, N_t is the density of traps, v_{th} is the average thermal velocity, E_t is the trap energy level and E_i is the intrinsic Fermi level [14]. From equation 2.9, U is maximised when the trap state energy and the Fermi level coincide in the middle of the band gap, which is the case in intrinsic semiconductor regions. The resulting temperature dependence of the dark current, from the proportionality with n_i, is given by equation 2.10. In this case, E_a is approximately equal to $E_g/2$.

$$J_{\text{SRH}} \propto n_i \propto T^{\frac{3}{2}} \exp\left(-\frac{E_a}{k_B T}\right) \tag{2.10}$$

Tunnelling mechanisms

Another possible mechanism is the tunnelling of electrons directly from the valence band to the conduction band at sufficiently high voltages. The tunnelling current of a p-n junction is given by equation 2.11, where m^* is the electron effective mass, V is the applied reverse bias and E is the average electric field in the inside the junction [14].

$$J_t = \frac{\sqrt{2m^*}q^3EV}{4\pi^2\hbar^2\sqrt{E_g}} \exp\left(-\frac{4\sqrt{2m^*}E_g^{3/2}}{3qE\hbar}\right) \tag{2.11}$$

As opposed to equations 2.6 and 2.10, tunnelling current does not contain a temperature term in the exponential, however the band gap is a temperature dependent term and therefore, the dark current generated by band to band tunnelling is reduced at low temperatures. However, as this is a relatively weak dependence, the activation energy of band to band tunnelling will be lower than that for diffusion or SRH dark currents. This process can also be assisted by defects where the carrier tunnels via a trap state inside the band gap. This trap-assisted tunnelling is also weakly dependent on temperature and is proportional to the trap density of the semiconductor [15].

Surface current

The previous three mechanisms are all bulk-limited, meaning that the magnitude of the dark current is proportional to the area of the mesa. However, surface dominated dark currents are proportional to the device perimeter. These dark currents originate from dangling bonds at the abrupt edge of the semiconductor surface. Usually they can be avoided by the passivation of the surface using dielectrics such as SU-8. Typically, surface currents are differentiated from Auger and SRH processes by their weak temperature dependence and from tunnelling currents by their proportionality to the perimeter rather than area.

2.2.2 Capacitance

At a p-n junction, the holes in the p-type layer diffuse to the n-type layer and recombine. Electrons from the n-type layer will behave similarly and recombine after diffusing to the p-type layer. These carriers leave behind charged, immobile acceptor or donor atoms respectively. This results in the p-type and n-type layers becoming negatively or positively charged. This creates an electric field which causes a current in the opposite direction to the diffusion of carriers. Eventually, these processes reach equilibrium and form a space-charge region which is analogous to a parallel plate capacitor given by:

$$C = \frac{\epsilon_r \epsilon_0 A}{W} \tag{2.12}$$

where ϵ_r and ϵ_0 are the relative and vacuum permittivity of free space, A is the area of the junction and W is the width of the space charge region. The width is also known as the depletion width and is referred to as such throughout this thesis.

The depletion width is required to overall remain charge neutral so that the sum of the positive charges equals the sum of the negative charges.

$$p + N_A = n + N_D \tag{2.13}$$

Typically, the doping concentration is much higher than the number of free electrons or holes (n or p). Therefore, charge neutrality is preserved if:

$$N_A w_p = N_D w_n \tag{2.14}$$

where w_p and w_n are the depletion widths in the p-type and n-type layers respectively. Typically, in a p-i-n, the intrinsic region contains several orders of magnitude less doping than the p or n-type layers it is junctioned with. Therefore, in the case of a p-i-n with an n-type intrinsic region, N_A is much greater than N_D which causes w_n to be much greater than w_p according to equation 2.14. This means that the intrinsic region is more easily depleted which is important in designing photodiodes and is discussed further in sections 2.2.4 and 2.2.5.

2.2.3 Absorption coefficient

The absorption coefficient (μ) is a measure of the distance light can travel through a medium before it is absorbed and has the dimension of inverse distance. Theoretically, in intrinsic semiconductors, the lowest energy photon that can be absorbed is determined by the band gap and the absorption of higher energy photons is given by:

$$\mu \propto (E_p - E_g)^{1/2} \tag{2.15}$$

where E_p is the energy of the photon that is to be absorbed. This equation is only valid for direct band gap semiconductors and only for parabolic band structures. Therefore, it is only applicable at photon energies close to the band gap energy [16].

However, in real semiconductors, some absorption at lower energies is possible due to a manifestation of structural disorder in the lattice. In semiconductors the exponential slope of the absorption coefficient is referred to as the Urbach edge and is expressed as:

$$\mu(E) = \mu_g \exp\left(\frac{E - E_g}{E_0}\right) \tag{2.16}$$

where E_0 is the characteristic energy of the Urbach edge, also referred to as the Urbach energy, and μ_g is the absorption coefficient at the band gap energy. In general, the larger E_0 is, the larger the concentration of defects or impurities in the structure. Typical experimental results for epitaxially grown III-V semiconductors give an Urbach energy of around 10 meV [17], while Urbach energies as low as 7.5 meV have been found in crystalline GaAs [18].

2.2.4 Responsivity and quantum efficiency

The responsivity (R) and the quantum efficiency (QE) are both parameters used to describe the signal generated when light is incident on the photodetector. The responsivity is the ratio of the photocurrent generated in the detector to the power of the incident light has units of $\mathrm{A\,W^{-1}}$. Commercially available detectors typically use the responsivity rather than the quantum efficiency for a more convenient method of measuring the power of a light source.

On the other hand, the quantum efficiency (QE) is the ratio of the number of photo-generated electrons (N_e) to the number of incoming photons (N_p) which can be described further by equation 2.17, where I_p is the photocurrent, P is the incident power on the surface and λ is the wavelength of the incoming light. For semiconductor photodiodes, both the responsivity and QE are wavelength dependent, so the incident light must be monochromated for a reliable power measurement.

$$\mathrm{QE} = \frac{N_e}{N_p} = \frac{I_p hc}{Pq\lambda} \tag{2.17}$$

Since I_p/P is the definition of the responsivity, it can be related to the quantum efficiency by:

$$\mathrm{QE} = \frac{Rhc}{q\lambda} \tag{2.18}$$

Quantum efficiency limitations

In vertically illuminated p-i-n photodiodes, the maximum quantum efficiency, which is the proportion of incident light that is absorbed by the semiconductor, is limited by reflection that occurs on the surface of the photodiode and the amount of absorption

that can occur given the thickness of the absorbing width of the p-i-n (L). Therefore, the maximum quantum efficiency is given by:

$$\mathrm{QE}_{\max} = (1 - R_s)(1 - \exp(-\mu L)) \tag{2.19}$$

where R_s is the reflection coefficient at the surface of the semiconductor caused by a large mismatch in refractive indices of air and semiconductor, for the air-GaAs interface this is approximately 0.3. If the reflection at the surface is included in equation 2.19, the resulting value is known as the external quantum efficiency. If an anti-reflection coating is used so that $R_s = 0$, the resulting value would be known as the internal quantum efficiency ($\mathrm{QE}_{\mathrm{int}}$). Typically, studies will measure the external quantum efficiency using equation 2.17 and divide by $1 - R_s$ to show the potential internal quantum efficiency.

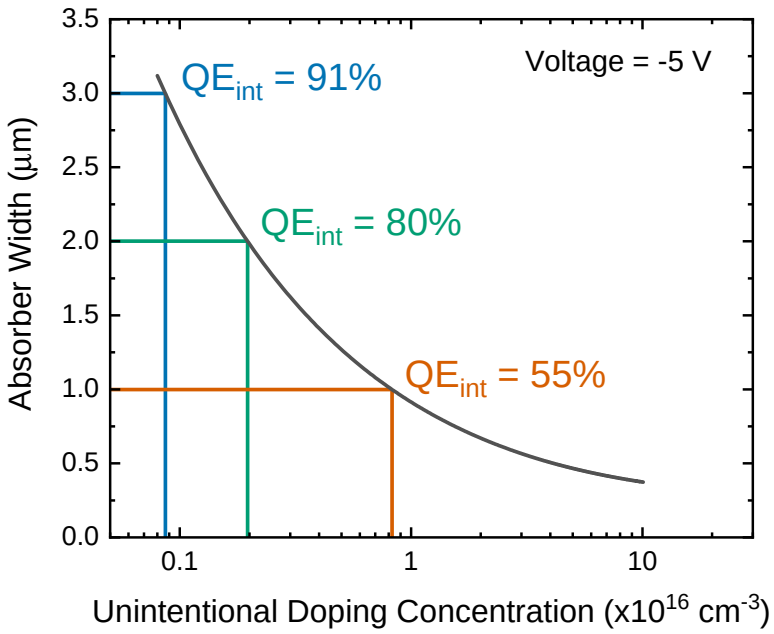

Figure 2.3: The effect of the unintentional doping against depletion width with several internal quantum efficiencies calculated from an absorption coefficient of $8000\,\mathrm{cm}^{-1}$.

While increasing the width of the semiconductor improves the amount of light absorbed, this may not necessarily increase the measured quantum efficiency. Carriers must be collected by the internal electric field in the photodetector once they are generated by an absorbed photon. The width of the space-charge region is limited by the unintentional doping concentration of the intrinsic region. Figure 2.3 shows the intrinsic width that can be depleted with different unintentional doping concentrations with an applied bias of $-5\,\mathrm{V}$. The internal quantum efficiencies with an absorption coefficient of $8000\,\mathrm{cm}^{-1}$ at several thicknesses are also indicated.

However, even if a layer is not depleted, it is possible for carriers to diffuse to the space-charge region. The following section details the calculation required to account for carriers generated by absorbed photons before and after the electric field.

Modelling the quantum efficiency

In a homojunction p-i-n, photons will be absorbed both inside and outside the electric field in the cladding layers, as shown in figure 2.4a. The carriers that are generated outside the electric field may contribute to the photocurrent by diffusing into the depletion region, which is modelled by equation 2.20 [14].

$$I_f = \frac{qF(1-R_s)\mu L}{\mu^2 L^2 - 1}\left(\frac{\frac{SL}{D} + \mu L - e^{-\mu x_j}\left(\frac{SL}{D}\cosh(x_j/L) + \sinh(x_j/L)\right)}{\frac{SL}{D}\sinh(x_j/L) + \cosh(x_j/L)} - \mu L e^{-\mu x_j}\right) \tag{2.20}$$

Since the equation can be applied to either a p-i-n or n-i-p, D, L and S in equation 2.20 are the diffusivity, diffusion length and surface recombination velocity of the electron or hole respectively. F is the incoming photon flux per bandwidth and x_j is the position of the start of the electric field.

The photocurrent generated due to the absorption of light beyond the depletion region, which diffuses to the electric field, is modelled by equation 2.21.

$$\begin{aligned} I_b = {} & \frac{qF(1-R_s)\mu L}{\mu^2 L^2 - 1}\exp(-\mu(x_j + W))\times \\ & \left(\mu L - \frac{\frac{SL}{D}\left(\cosh(H/L) - \exp(-\mu H)\right) + \sinh(H/L) + \mu L\exp(-\mu H)}{\frac{SL}{D}\sinh(H/L) + \cosh(H/L)}\right) \end{aligned} \tag{2.21}$$

where H is the width of absorber beyond the depletion width, W.

Inside the depletion width, the photocurrent due to drift collection is given by:

$$I_{dr} = qF(1-R_s)\exp(-\mu x_j)\left(1 - \exp(-\mu W)\right) \tag{2.22}$$

The total photocurrent generated is the sum of I_f, I_b and I_{dr}. Since the quantum efficiency is the ratio of the number of charge carriers that reach the contacts to the number of incoming photons, the photocurrent can be divided by qF to obtain the QE.

In order to use these equations, accurate knowledge of the diffusivity is needed for both electrons and holes. Fortunately, in double heterojunction devices, absorption can only occur in the intrinsic region therefore carriers can only diffuse from one direction, as shown on figure 2.4b. For instance, using figure 2.4b as an example, only holes can

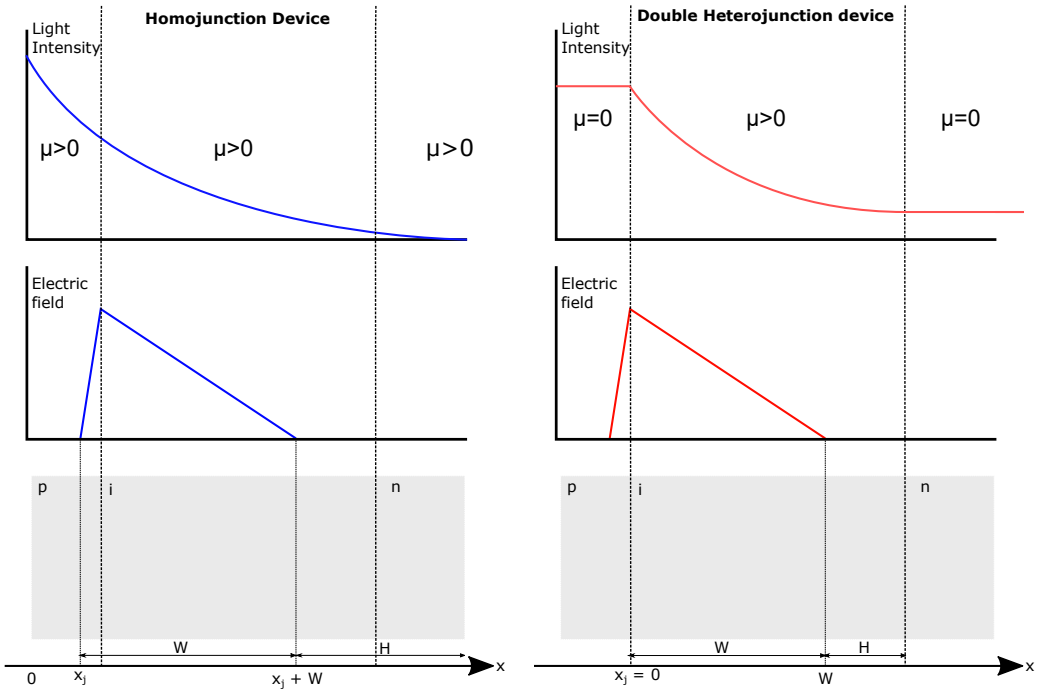

(a) A homojunction p-i-n

(b) A double heterojunction p-i-n.

Figure 2.4: The differences between the quantum efficiency of a homojunction and double heterojunction device. No light will be absorbed in the cladding layers in the double heterojunction device so that we only consider the absorbing region. Illumination in both cases is from the left side.

be collected from beyond the depletion width where $x > W$. Therefore, only the hole diffusivity and carrier lifetime are needed as equation 2.20 will go to zero. Reliable measurements of the depletion width are required for this model to work and were obtained through capacitance-voltage measurements as described in section 4.4.2.

The surface recombination velocity is another parameter that requires optimisation. Previously, the surface recombination velocity in GaAs has been shown to be $1 \times 10^5\,\mathrm{cm\,s^{-1}}$ at a doping concentration of $1 \times 10^{15}\,\mathrm{cm^{-3}}$ [19], a similar doping level to the intrinsic doping in the GaInNAsSb layers. Therefore, the surface recombination velocity for GaInNAsSb is predicted to be similar. This parameter is expected to have a more significant impact at shorter wavelengths, therefore the diffusion parameters can be fitted using the long wavelength data before attempting to optimise the value for surface recombination velocity.

The reflection due to the GaAs substrate can be calculated using wavelength-dependent refractive index (n_{GaAs}) from Adachi [20] and equation 2.23.

$$R_s = \frac{(1 - n_{\mathrm{GaAs}})^2}{(1 + n_{\mathrm{GaAs}})^2} \tag{2.23}$$

2.2.5 Bandwidth limitations

The two limitations of bandwidth of a photodiode are the time required for a carrier to travel through the sample, and the RC limit. Both of these factors are related in opposite ways to the intrinsic thickness of the p-i-n diode.

The transit time bandwidth is governed by equation 2.24, where v_s is the saturation velocity of the charge carriers.

$$f_{3db}^{tr} = 0.5\frac{v_s}{W} \tag{2.24}$$

The RC limitation arises from the capacitance of the photodiode as given by equation 2.12. This gives a bandwidth as described by equation 2.25, where R is the resistance in series with the p-i-n photodiode.

$$f_{3db}^{RC} = \frac{1}{2\pi RC} = \frac{W}{2\pi R\epsilon A} \tag{2.25}$$

Combined, they give an overall bandwidth of:

$$f_{3dB} = \frac{1}{\sqrt{f_{RC}^{-2} + f_{tr}^{-2}}} \tag{2.26}$$

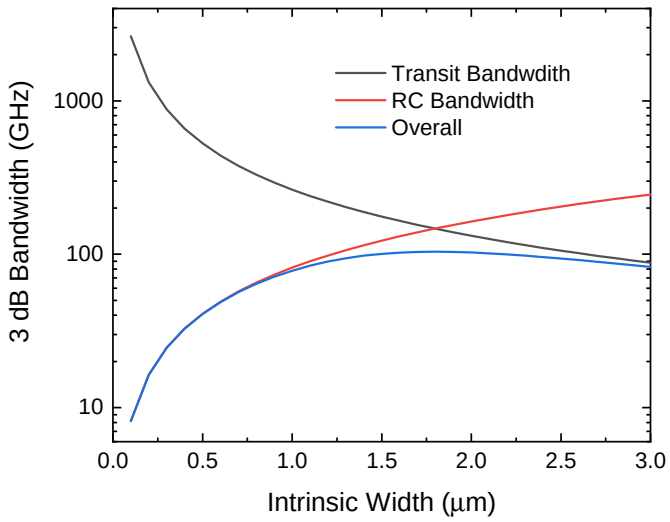

Figure 2.5: The fundamental bandwidth limitations of vertically illuminated p-i-n photodiodes due the thickness of the intrinsic region. Model assumes negligible depletion in cladding layers, drift velocity of $6 \times 10^6\,\mathrm{cm\,s^{-1}}$, device diameter of 20 µm and resistance of 50 Ω.

This is modelled in figure 2.5 for an InGaAs p-i-n of a diameter 20 µm with a resistance of 50 Ω and a saturation velocity of 6×10^6 cm s^{-1} [21]. This figure shows that an intrinsic width of approximately 1.5 µm provides a compromise between the transit time and RC bandwidths. Though in practice, the transit time bandwidth may be higher due to the overshoot velocity found in InGaAs [22].

Eye diagrams

An eye diagram is a way of showing the signal quality, a detector is illuminated by a light source set at a certain transmission rate and waveforms generated by the detector are captured and super imposed on each other. If the waveforms closely match each other, then good signal to noise ratio is demonstrated and the detector can be operated at such speeds. An example of an "eye"-diagram is shown on figure 2.6.

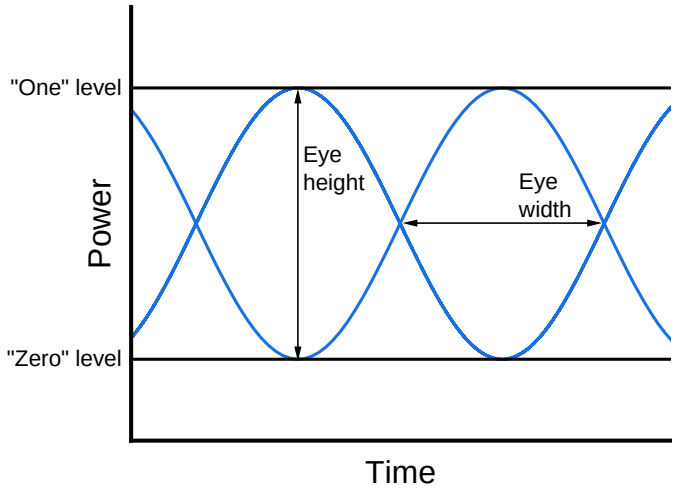

Figure 2.6: An example of an "eye"-diagram illustrating the two power levels of the detector as well as the transition to each level. This is an idealised example with zero noise and therefore the eye height and width are clearly visible, indicating an open eye and good level of signal integrity.

2.3 Other detector types

The previous section was based around the optimisation of vertically illuminated p-i-n photodiodes, which are preferred for the purpose of this study due to their ease of designing, processing and characterisation. However, there are different device designs that are utilised in other studies and represent potential future avenues of research.

Uni-travelling carrier photodiodes (UTC-PD) use a thin, doped absorber layer instead of the thicker intrinsic region of p-i-n photodiodes, and a wider band gap carrier-collection layer [23]. Electrons generated in the absorption layer can diffuse to the

collection layer and, due to the higher mobility and drift velocity of the electron, the response limit caused by transit time is increased. This design can be advantageous to use with dilute nitrides as the unintentional doping concentration can be high, preventing depletion in thicker photodiodes [24], as well as due to a lower mobility as compared to InGaAs.

Resonant cavity enhanced photodiodes (RCEPD) utilise an absorber within a Fabry-Pérot cavity to maximise the quantum efficiency despite a small normalised absorption coefficient (μW). On GaAs substrates, GaAs and AlAs have a much larger difference in refractive index compared to what is achievable on InP substrates allowing for much higher reflectivity DBRs. Furthermore, due to the selectivity of the DBR, RCEPDs provide a very narrow spectral bandwidth of detection such as Balkan et al. [25] who produced a GaInNAs RCEPD with a full width half maxima of 5 nm. This could be advantageous in applications where wavelength selectivity is a requirement.

Waveguide structures, as opposed to the vertically illuminated UTC-PD and RCEPD, are illuminated from the side, perpendicular to the growth axis. The responsivity of the device is therefore no longer limited by the depletion width in the photodiode, instead it is limited by the dimensions of the ridge created in the device processing step. Furthermore, most devices are grown with relatively thin absorbing regions (approximately 400 nm), therefore the transit time of carriers through the electric field is kept to a minimum while maximising the absorption length and width (typically >20 µm and 5 µm respectively). Similar to UTC-PDs, the limiting factor in the speed of the detector is the RC limit which is small due to the small depletion width resulting in a large capacitance.

2.4 Avalanche photodiodes

2.4.1 Explanation of avalanche gain

The physical process driving the internal gain in APDs is impact ionisation. It occurs when a carrier (either an electron or a hole) gains enough energy travelling through an electric field and collides with an electron in the valence band and promotes it to the conduction band, creating an electron-hole pair. The initial carrier and the two extra carriers will continue travelling through the crystal and can ionise further carriers should they gain enough energy. By this mechanism, APDs allow for the amplification of small photocurrents generated by weak incoming signals. With sufficiently high fields, the ionisation process will continue indefinitely leading to an avalanche breakdown.

The probability of a carrier initiating impact ionisation can be described by an extended version of Chynoweth's expression shown in equation 2.27, where α and β represent the electron and hole impact ionisation coefficients respectively, E is the magnitude of the electric field the carrier is experiencing, while A, B and C are material parameters that are different for electrons and holes. α and β have dimensions cm^{-1} so that $1/\alpha$ and $1/\beta$ represent the mean ionisation length of the electron or hole.

$$\alpha, \beta = A_{e,h} \exp\left(\frac{B_{e,h}}{E}\right)^{C_{e,h}} \tag{2.27}$$

Since avalanche gain is a stochastic process, the amount of multiplication each injected carrier generates is variable. The noise factor, F, is a measure of the increase of noise with increasing variance in the amount of gain and is strongly dependent on the ratio of the ionisation coefficients ($k = \frac{\beta}{\alpha}$) and the multiplication factor (M). For the case of pure electron injection, the noise factor is given by:

$$F = kM + (2 - \frac{1}{M})(1 - k) \tag{2.28}$$

The noise factor can be minimised by the choice of material used as an avalanche medium. A larger ratio of impact ionisation coefficients will tend F to 2 at sufficiently high multiplication.

2.4.2 Random path length model

The model that is chosen to calculate the gain is the random path length model (RPL) described by Ong et al. [26] The program that we developed based on this model initialises a carrier at the first position the electric field is non-zero. This carrier passes through very small strips of the device, gaining energy according to:

$$E = \Sigma_i D_i x_i \tag{2.29}$$

Where D_i is the electric field in the strip and x_i is the thickness of the strip. Thin strips are used in this model to allow for electric field changes over thick layers whereas the original model by Ong et al. assumes a constant electric field across the device. The process continues until the carrier has gained an amount of energy greater than the minimum energy required to initiate impact ionisation. This energy is referred to as the threshold energy and can differ between electrons and holes. The distance that the carrier travels is called the dead space and is a crucial part of non-local models as the effect of the dead space is used to reduce the noise in thin APDs. This part of the

model relies on the assumption that the path of the ionising carrier is purely ballistic and no energy loss occurs due to any collisions before ionisation takes place. Therefore, in comparison to models in which scattering is taken into account the threshold energy in the RPL model is higher.

Once the required amount of energy is accumulated, the model calculates the probability of ionisation over a short length, $P(\delta x)$, which is given by:

$$P(\delta x) = \alpha^* \delta x \tag{2.30}$$

where α^* is the ionisation probability per unit distance after the dead space, given by:

$$\alpha^* = \frac{\alpha}{1 - d\alpha} \tag{2.31}$$

where d is the dead space.

In the situation where the particle does not ionise after reaching the threshold energy and passing through the first strip, the cumulative probability is calculated by considering the probability that the particle will ionise over the next strip and the probability that it has not ionised over previous strips.

If the cumulative probability of ionising is greater than a random number generated at the start of the ionisation process, the program considers the carrier ionised and creates two extra carriers – one of the same type as the primary carrier, and one carrier of the complementary type. Both primary-type carriers continue in the same direction while the secondary carrier will proceed in the opposite direction. If the probability never exceeds the required value, the original primary carrier reaches the end of the device and does not impact ionise. The result of M = 1 is returned. This process is repeated and averaged over 10^5 times for a consistent and accurate measurement. Either electrons or holes can be specified as the primary carrier so that pure electron or hole initiated multiplication can be modelled.

2.4.3 Separate absorption and multiplication avalanche photodiodes

In many materials, the electric fields required for avalanche multiplication are too high for normal operation and can lead to high dark currents from band to band tunnelling. Therefore, it can be advantageous to use a separate absorption and multiplication APD (SAM APD) which combines the absorption properties of a low band gap material with the multiplication properties of a wider band gap material. The electric field is kept to

a controllable level by the presence of a thin, highly doped charge sheet layer which is the same material as the multiplication region.

Depending on the doping type of the absorber and charge sheet, either electrons or holes generated by the absorption of light can be injected into the multiplication region.

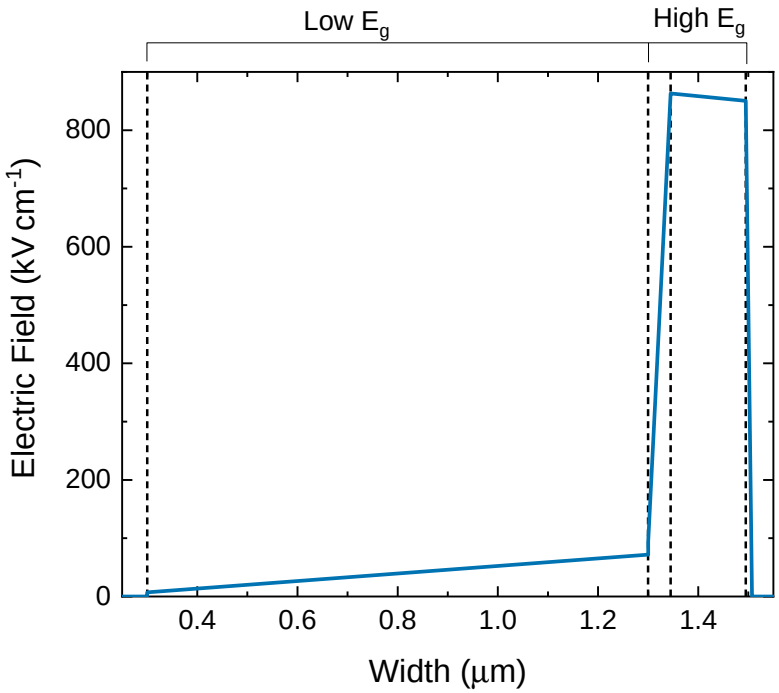

Figure 2.7: An example of the electric field in a SAM APD. The thin charge sheet located at 1.3 µm limits the electric field in the low E_g absorber.

Chapter 3

Literature Review

This chapter will summarise options for detection at telecommunication wavelengths including those lattice matched to other substrates such as InP, GaSb and outside of III-V research, Si. After that, this chapter discusses the current state of detectors that are epitaxially grown on GaAs substrates including lattice mismatched absorbers and dilute nitride alloy growth and detectors.

3.1 InP-based detectors

InGaAs photodiodes

InGaAs p-i-n photodiodes are currently the incumbent commercial device for detection at NIR wavelengths, most notably 1.55 µm. The most commonly used structure is the vertically illuminated photodiode, due to its uncomplicated device design and packaging. As mentioned in sections 2.2.4 and 2.2.5, the thickness of the depletion width can control the quantum efficiency and bandwidth of the detector. A wide depletion width can increase the quantum efficiency but would decrease the transit time bandwidth. Therefore, past studies have used thin intrinsic InGaAs widths such as Wey et al. [27] who fabricated InGaAs/InP photodiodes with an intrinsic thickness of 0.2 µm. Fabricated devices with an area greater than 25 μm^2 were limited in bandwidth by RC effects. For the smallest photodiode (hence smallest capacitance), the bandwidth reached 110 GHz. This bandwidth is not required for the applications of this study, and instead may degrade other qualities such as dark current in order to gain more improvements in bandwidth, however it does show the incredibly high potential speeds that can be obtained.

Furthermore, the leakage current for the device was measured to be 40 nA at −1 V which corresponds to a dark current density of 0.16 $A\,cm^{-2}$. Other studies, with lower

bandwidths, have presented InGaAs photodiodes with a lower dark current of $0.08\,\mathrm{A\,cm^{-2}}$ [28] or $2.2 \times 10^{-6}\,\mathrm{A\,cm^{-2}}$ [29]. The latter dark current is more representative of 10 GHz photodiodes as the other two are sacrificing dark current in order to gain a larger bandwidth. Typical dark current values of commercial photodiodes are around 5 nA for devices with diameters of approximately 30 µm [30].

Wey et al. also report a quantum efficiency of 31%. However, this value was measured with the illumination of a 1.06 µm laser. At a longer wavelength such as 1.55 µm, the internal quantum efficiency is expected to only be approximately 12%, or a responsivity of $0.15\,\mathrm{A\,W^{-1}}$. Therefore, if a bandwidth as high as 110 GHz is not a requirement, it is beneficial to increase the thickness of the intrinsic layer to improve the quantum efficiency.

Since decreasing the size of the device further would not increase the bandwidth, the response is transit time limited. Therefore, improvements to vertically illuminated photodiodes have originated from device design. The photocurrent in UTC photodiodes is purely reliant on the transport of electrons. Shimuzu et al. [31] fabricated InGaAs/InP UTC photodiodes with a bandwidth of 150 GHz with a device with an area of 10 and $20\,\mu\mathrm{m}^2$. This indicates that despite the improvement to the bandwidth, the limiting factor is still the transit time limit. Further improvements on the device design come from developments on the near-ballistic UTC (NBUTC). This allows for the electrons to reach near the maximum overshoot velocity of $4 \times 10^7\,\mathrm{cm\,s^{-1}}$. Shi et al. [32] designed a NBUTC device, with an active area of $16\,\mu\mathrm{m}^2$ to have a bandwidth of 250 GHz. However, reaching bandwidths that are this high is the result of a thin absorption layer of 150 nm, leading to a responsivity of only $0.08\,\mathrm{A\,W^{-1}}$.

InGaAs waveguide photodiodes

In order to achieve high responsivities and high speeds, a waveguide photodetector can be used to minimise the distance carriers are required to travel. Kato et al. [33] fabricated a "mushroom-mesa" waveguide which not only has a quantum efficiency of 50% at 1.55 µm, but also had bandwidth of 110 GHz. However, despite the large QE-bandwidth product that waveguide photodiodes can offer, they are subject to very low tolerance on the coupling between incoming light and the detector. Evanescently coupled waveguide photodiodes can help reduce the tolerance on light coupling by placing the absorber region near the waveguide as shown in figure 3.1. Typically, a layer is added in between the waveguide structure and the absorption region. This leads to devices with high

bandwidths of 100 GHz and a high bandwidth-efficient product of 53 GHz [34].

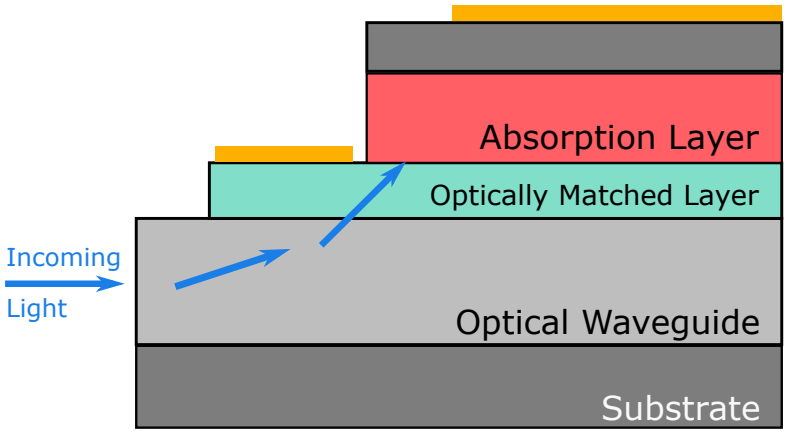

Figure 3.1: A schematic diagram of an evanescently coupled waveguide photodiode.

InGaAs resonant cavity photodiodes

Several solutions have emerged as possible methods of obtaining high reflectivity DBR mirrors based on InP substrates. An option proposed by Murtaza et al. [2] used Burstein-shifted InGaAs and InP to form a DBR mirror on the bottom of the photodiode. The Burstein shift, also known as the Moss-Burstein effect, is the effective increase of a band gap as a result of conduction band states becoming populated. The shift occurs when the n-type doping is sufficiently high so that the Fermi level lies within the conduction band. This causes an electron in the valence band to be excited above the Fermi level, which subsequently causes the apparent band gap. With a doping of $1 \times 10^{19}\,\mathrm{cm}^{-3}$, Murtaza et al. fabricated an InGaAs/InP DBR with a reflectivity between 95-97% using 20 mirror periods. This result is quite high for InP-based materials and corresponds to an absorption of less than 3%. A quantum efficiency of 65% was measured where a similar thickness p-i-n would result in a quantum efficiency of 16%.

Kimukin et al. [3] proposed the use of quarter-wave stacks of $In_{0.53}Al_{0.13}Ga_{0.34}As$/InAlAs layers as a bottom DBR for a high reflectance at 1.55 µm. However, these two materials have a closer refractive index than InGaAs/InP as shown in table 3.1. This results in a theoretical maximum of 95% reflectivity with the use of 25 mirror periods, which is lower than the value achieved by Murtaza et al. Regardless, a quantum efficiency of 66% is measured along with an operating bandwidth of 31 GHz.

However, in comparison to GaAs/AlAs, there is still room for improvement. GaAs/AlAs have a much greater difference in refractive index as shown in table 3.1. With 15 mirror periods, a reflectivity of over 99% can be reached with GaAs/AlAs [4].

Author:	Murtaza et al. [2]		Kimukin et al. [3]		Jasik et al. [4]	
Material 1:	InGaAs [35]	3.43	InAlGaAs [36]	3.43	GaAs [35]	3.3
Material 2:	InP [35]	3.1	InAlAs [36]	3.20	AlAs [35]	2.86

Table 3.1: The refractive indices used in DBR mirrors in InP-based RCEPDs compared with GaAs/AlAs.

A method with a more complex fabrication was presented by Huang et al. [37], by using the refractive index difference of air and InP to fabricate a Bragg reflector. This is achieved by initially growing periods of InGaAs and InP before the p-i-n. A wet etch is applied which selectively removes the InGaAs, while leaving the InP untouched. Despite the bottom mirror comprising of only two air-gap layers, it reaches a reflectively of 95% at 1.55 µm. Furthermore, a peak quantum efficiency of 59% was measured as well as a 3 dB bandwidth of 8 GHz. However, the processing for this method is very complex compared to the previous studies.

InGaAs avalanche photodiodes

An avalanche photodiode can also improve the responsivity by the use of its internal gain mechanism. Initial SAM APDs were fabricated with an avalanche layer of InP [38]. While InP is a more suitable material than InGaAs for multiplication due to its larger band gap suppressing tunnelling currents, $Al_{0.48}In_{0.52}As$ (hereafter referred to as AlInAs) is more commonly used in recent research. In comparison with InP, AlInAs has a larger band gap and a greater ratio of impact ionisation coefficients which leads to low noise operation of the AlInAs APD. Kinsey et al. [39] fabricated a waveguide APD with a gain-bandwidth product of 320 GHz, where the relatively thin avalanche region of 150 nm produced an excess noise corresponding to $k = 0.15$. Lahrichi et al. [40] fabricated a backside illuminated APD with a gain bandwidth product of 240 GHz with a thinner avalanche region of 100 nm. In order to decrease the excess noise factor, typically the avalanche region is thinned. However, thinning the AlInAs layer to 100 nm and under can lead to large dark currents caused by band to band tunnelling, furthermore similar impact ionisation coefficients limit the overall gain-bandwidth product [41].

The most recent advance in InP-based APDs has been a shift away from AlInAs avalanche layers in favour of $AlAs_{0.56}Sb_{0.44}$. Initial studies into the impact ionisation coefficients showed a very low excess noise factor corresponding to $k = 0.05$ for a multiplication width of 80 nm [42]. An example of an APD was fabricated and demonstrated

to have high sensitivity with a very wide avalanche width of 660 nm [43].

3.2 GaSb-based detectors

GaSb-based APDs have potential to operate at 1.55 µm and beyond due to the availability of absorbers lattice matched to GaSb such as InAsSb. However, suitable multiplication materials have not been fully explored. Recently, digital alloys of $Al_{0.7}In_{0.3}As_{0.3}Sb_{0.7}$ were demonstrated with a value for $k = 0.015$ [44]. This result is achieved without using a thin multiplication layer and instead uses an 890 nm intrinsic region.

This was advanced further by Bank et al. [45] who developed a SAM APD using a different composition of AlInAsSb as an absorber capable of operating at 1.55 µm. The k-value of this APD was found to be around 0.01 up to multiplication values of approximately 20. The low noise-operation of this APD is similar to Si and is attributed to a large impact ionisation coefficient ratio due to high scattering rates and high effective mass.

3.3 Si-based detectors

3.3.1 Ge photodetectors

While the integration of III-V materials with CMOS is possible, it remains a complicated and expensive process. However, using Si to fabricate NIR photodetectors is not efficient due to the indirect band gap with a cut-off wavelength of 1.1 µm. Instead, Ge can be used to provide absorption at important communication wavelengths including the L and C bands. Ge is also indirect, but with a much smaller indirect band gap of 0.66 eV and a direct band gap of 0.8 eV, this leads to an absorption coefficient of approximately 1000 cm^{-1}. An example of a Ge on Si photodiode is demonstrated by Jutzi et al. [46]. Since a relatively thin Ge intrinsic region of 300 nm is used, a small responsivity at 1610 nm was measured to be approximately 0.2 mA W^{-1}. Furthermore, the dark current density of the sample is relatively high at 100 mA cm^{-2} at a voltage of −1 V. This is likely caused by the lattice mismatch that does appear between Ge and Si. Despite this, a bandwidth of 9.9 GHz was measured with zero bias for a device with diameter 20 µm.

It is possible to introduce tensile strain to the Ge layer by the thermal expansion mismatch between the epitaxial Ge and the Si substrate. This reduces the direct band gap of Ge from 0.801 to 0.773 eV and a longer cut-off wavelength of 1.6 µm [47]. Liu et al. [47] epitaxially grew a Ge layer with a thickness of 2.3 µm. The Ge p-i-n has

a responsivity of $0.56\,\mathrm{A\,W^{-1}}$ which corresponds to an absorption coefficient of approximately $2000\,\mathrm{cm^{-1}}$. In comparison to an unstrained sample with an absorption coefficient of $1000\,\mathrm{cm^{-1}}$, this is not a significant improvement. However, the dark current density of the device is kept relatively low despite the strain at $20\,\mathrm{mA\,cm^{-2}}$.

An alternative to strained Ge is the addition of Sn, which also reduces the band gap. With a Sn content of 1.78%, a p-i-n photodiode has been fabricated with a responsivity of $0.181\,\mathrm{A\,W^{-1}}$ at $1.55\,\mu\mathrm{m}$ with a GeSn thickness of 300 nm [48]. The effect of the addition of Sn is difficult to extract due to the 410 nm Ge cladding layers which can also absorb at $1.55\,\mu\mathrm{m}$. The dark current increases very rapidly from $1\,\mathrm{mA\,cm^{-2}}$ in a Sn-free sample to $50\,\mathrm{mA\,cm^{-2}}$ in the previously mentioned sample. This is attributed to an increase in defects with increasing amounts of Sn.

Other detector structures are also possible with several groups producing waveguide photodiodes [49]. These designs can accommodate for the low absorption coefficient of Ge by providing a much larger absorption width without sacrificing speed. This is demonstrated by Vivien et al. [50] who fabricated a Ge on Si waveguide photodetector with a responsivity of $0.8\,\mathrm{A\,W^{-1}}$ at $1.55\,\mu\mathrm{m}$ as well as operation at 40 Gb/s. The viability of operating the detector at 40 Gb/s was verified by the use of "eye"-diagrams. In the study by Vivien et al., even with a data transmission rate of 40 Gb/s, the eye is clearly open, especially with $-1\,\mathrm{V}$ applied bias. Dark current remains a problem as the detector reaches a dark current of $4\,\mu\mathrm{A}$ which corresponds to a density of $80\,\mathrm{A\,cm^{-1}}$.

Furthermore, APDs developed with this material system are able to take advantage of the large difference in impact ionisation coefficients of Si with a SAM APD. This large impact ionisation coefficients ratio provides extremely low noise operation without the need for extremely thin layers. For example, Kang et al. [51] fabricated Ge/Si APDs with a gain-bandwidth product of 340 GHz and a k-value of 0.08 which was achieved using a total of 600 nm Si-width with a 100 nm charge sheet and a 500 nm multiplication width. Theoretically, this gain-bandwidth could improve further by the use of a thinner multiplication width which is well demonstrated with InAlAs and InP.

More recently, Huang et al. demonstrated high quality growth of Ge on Si in order to fabricate Ge/Si APDs [52]. An annealing process was used to improve the absorption coefficient of Ge at $1.55\,\mu\mathrm{m}$. Although it was not experimentally verified, it was predicted to increase the absorption coefficient to $3200\,\mathrm{cm^{-1}}$. The most optimal APDs were used to test over various encoding schemes, where a record sensitivity was demonstrated at 25 Gb/s NRZ and 56 Gb/s PAM4 applications. PAM4 is the encoding of two signals of

different amplitudes in order to double the amount of bits transferred. Therefore it is approximately twice as fast as NRZ applications. However, the gain in bandwidth comes with a requirement for an increased signal to noise ratio which is well demonstrated by Huang et al.

3.3.2 Wafer-bonded photodetectors

In addition, it is possible to integrate III-V semiconductors onto Si substrates using wafer bonding techniques [53]. This involves the joining of two semiconductor surfaces so that bonds can form across the interface. A thermal anneal can be applied to increase the strength of the bonds. This technique can be used to avoid the formation of defects that arise from the highly mismatched growth of InP-based materials on Si.

InGaAs photodetectors epitaxially grown on InP and then wafer bonded to Si have been demonstrated with bandwidths of up to 20 GHz [54], which is lower than those previously mentioned in section 3.1 as the length of the InGaAs absorber is 1 µm and the area of the mesa is larger. Furthermore, the dark current of this device is relatively low at 100 nA at -10 V, the same voltage that used to measure the bandwidth. This corresponds to a dark current density of 22 mA cm^{-2}.

Wafer bonding InP-based detectors to Si also allows RCEPDs to be fabricated using Si/SiO_2 as DBR mirrors. Salvador et al. [55] fabricated an RCEPD using a 0.1 µm InGaAs layer. A p-i-n of this thickness would only be capable of a quantum efficiency of 5%, whereas by using a single pair Si/SiO_2 stack on top and a near unity reflection stack on bottom the quantum efficiency was raised to 48%. The process was completed without an anneal which is typically applied to strengthen the bonds on the interface between the Si and InP.

Furthermore, APDs with a gain-bandwidth product of 300 GHz can be fabricated by using Si as the multiplication layer and InGaAs as an absorption layer [56]. In this study, the multiplication layer is found to be 650 nm and it results in a similar gain-bandwidth product to that of a Ge/Si SAM APD fabricated by Kang et al.

However, wafer bonding techniques have limitations. The surfaces of Si and InP must be extremely flat and smooth. Flatness is not typically an issue in commercially available semiconductor wafers, but the surface roughness must be minimised and can be dependent on any processing techniques applied. Furthermore, the heat treatment applied to the sample can cause significant problems for processed devices with metal patterns and also cause the diffusion of dopants. In addition, the heat treatment can

cause any contaminants to create air bubbles at the interface of the bond [57].

3.4 Lattice mismatched GaAs-based detectors

Outside of dilute nitrides, it is possible to fabricate detectors based on GaAs despite the lack of conventional alloys available. In order to achieve this, a material with a dissimilar lattice constant would be utilised. An example is the use of metamorphic InGaAs [58]. The large lattice mismatch is accommodated by a 2.4 µm buffer layer which steadily changes In content from 20% to 60%. The resultant InGaAs is relatively defect free after a post-growth anneal with a low dark current of $0.224\,\mathrm{mA\,cm^{-2}}$ and an RC-limited bandwidth of 7 GHz. Faster detection has been demonstrated with smaller devices up to 14 GHz [59], though this improvement is likely caused by lower resistance contacts. However, the long growth time required for the buffer layer is a possible disadvantage of metamorphic photodetectors compared to conventional lattice matched growth. Accounting for only the thickness of the layers and not growth rate, approximately 60% of the growth time is allocated to the buffer layer. Furthermore, by shifting the lattice constant to that of InGaAs, the ability to lattice match the absorber with either AlAs/GaAs DBR mirrors or AlGaAs avalanche multiplication layers is lost.

Alternatively, an interfacial misfit (IMF) array can be used on GaAs substrates to facilitate the growth of highly mismatched GaSb layers where generated dislocations propagate along the GaAs/GaSb interface rather than at a 60° angle to the epitaxial growth direction [60]. This is reported to be caused by the introduction of a Sb-flux on a Ga-rich surface which causes Sb to form islands along the interface rather than create defects in the GaSb layer. Careful management of the growth temperature is required for this process, the optimal substrate temperature during the Sb-flux should be 510 °C, while temperatures of 480 °C or 540 °C appeared to produce a more defect heavy GaSb layer [61].

The benefit of using an IMF layer is the ability to use the range of low band gap antimonide semiconductors while still providing the advantages of the AlGaAs material system. For instance, GaSb has a low enough band gap to allow absorption at 1.55 µm and, by using an IMF layer, can be combined with AlGaAs in a SAM APD [62]. In this device the excess noise was found to lie within $0.1 < k_{\mathrm{eff}} < 0.2$. However, the quantum efficiency of the sample is extremely low. Once punchthrough occurs in the GaSb/AlGaAs device, around 1 µA of photocurrent is measured with a 15 mW laser which corresponds to a quantum efficiency of approximately 0.005%. This is attributed

to the large band offsets between the materials in the SAM APD.

3.5 Dilute nitrides

Dilute nitride alloys lattice matched to GaAs have been researched since 1996 when Kondow et al. [63] proposed GaInNAs as a way of lasing at telecommunication wavelengths of 1.3 µm and 1.55 µm. In this study lasing at a wavelength close to 1.3 µm was demonstrated. From here, the material continued to find use in lasers but also in solar cells and photodetectors. The challenges of integrating a dilute nitride alloy for each of these applications are different, and so this chapter will focus mostly on detector applications.

3.5.1 Dilute nitride epitaxial growth

The growth of dilute nitride alloys can be facilitated either by molecular beam epitaxy (MBE) or by metalorganic chemical vapour deposition (MOCVD), however the compositional control and uniformity of MBE result in it being more favoured. Typically, in MBE, the source beam of the group V elements is created by cracking various species of the chemical, for example As_4 and Sb_4 into diameter As_2 and Sb_2. However, nitrogen in its standard state of N_2 is too stable and cannot be used with the same cracking methods as elements such as arsenic, antimony or phosphorus. Instead, the most successful method of producing atomic nitrogen has been the use of a plasma source. This plasma source will generate a mixture of dissociated atomic and molecular radicals and ions, therefore the conditions of the plasma must be optimised in order to maximise the concentration of atomic N. The amount of atomic to molecular nitrogen can be determined from the emission spectrum between 500 nm and 950 nm. Molecular nitrogen produces very broad bands (570-610 nm, 610-690 nm, and 710-780 nm) originating from transitions between vibrational states. However, atomic N produces three sharp peaks at 744.6 nm, 821.3 nm and 865.8 nm [64]. This is shown on figure 3.2. By measuring the intensities of the molecular bands and the atomic peaks, the amount of N atoms and excited N_2 molecules can be determined. However, this method cannot detect unexcited N_2 molecules as the emission only reflects the amount of transitions between energy levels rather than population.

Using a plasma source can have drawbacks. Harris et al. [65] describe issues related to the plasma stability due to inconsistency in the flow rate and also in igniting the plasma. Such issues may result in large differences between wafers grown in the same MBE system despite nominally identical settings. Furthermore, using the plasma allows

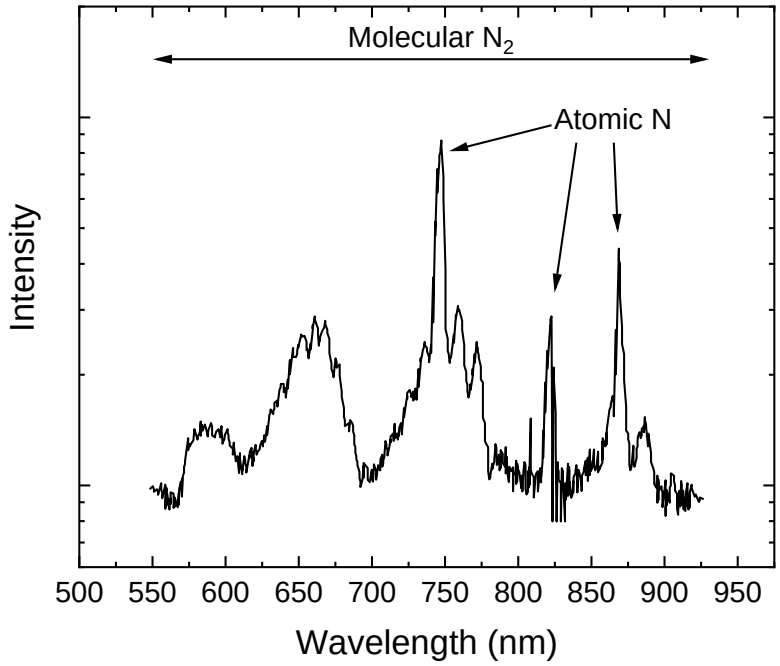

Figure 3.2: A typical emission spectrum for N plasma with indications of the peaks caused by molecular N_2 and atomic N. Adapted from Guina et al. [64].

for the formation of ions which can cause damage to the crystal structure. Wistey et al. [66] found that the use of biased deflection plates (with voltages of 18 and -40 V) resulted in a higher photoluminescence intensity as compared to a control sample grown with zero bias over the plates. The effect of the deflection plates is especially noticeable once the sample has been annealed above a temperature of 720 °C as the samples grown with the use of deflection plates have approximately five times the photoluminescence intensity of the sample with no deflection plate.

3.5.2 The effect of annealing on the band gap

The effect of a thermal annealing treatment in dilute nitride materials is unique compared to other III-V materials. First, there is a large improvement to the structural quality of the material and secondly, a significant blueshift of the cut-off wavelength is found. Since this blueshift can negate the effect of increased nitrogen incorporation, it is important to balance the crystal quality improvement with the change in band gap of the dilute nitride.

The blueshift due to annealing has been well recorded through various dilute nitride compositions and annealing conditions but the source of the blueshift has been attributed differently. Theoretical studies predict a change in band gap depending on the nearest neighbouring environment of the N atom [67]. Both studies predict a favourable en-

vironment during growth for the formation of Ga-N bonds, likely caused by the low temperature required for dilute nitride growth. However, during the anneal the In and Ga atoms are able to switch lattice sites to a more evenly distributed setting, or potentially even beyond the statistically expected of In-N bonds [67].

Experimental evidence of this effect was provided in a separate study by Kurtz et al. [68]. FTIR spectroscopy was used to probe the local arrangement of N atoms in GaInNAs. They found an absorption band at $470\,\mathrm{cm}^{-1}$ which is attributed to Ga-N [69] in as-grown samples, but after annealing another peak formed at $487\,\mathrm{cm}^{-1}$ which was attributed to the addition of In-N bonds. The relatively low concentration of In (between 1% and 2%) most likely inhibits the formation of N atoms with two In nearest neighbours.

Furthermore Klar et al. [8] used photoreflectance and theoretical calculations to show the blueshift is caused by the transition of nitrogen from Ga-rich sites to In-rich. Compared to Kurtz et al., there are distinct peaks in the photoreflectance which are shown to correlate with different nearest neighbour configurations as the In content of the alloy is much larger at 30%.

However, this explanation is insufficient when describing the blueshift found in GaNAs, and indium-free dilute nitride alloy. In studies of GaNAs, the blueshift was attributed to the out-diffusion of nitrogen in quantum wells [13], therefore reducing the nitrogen concentration within the quantum well and increasing the band gap. A blueshift was also found by Loke et al. [70], who attributed the overall blueshift to the hopping of nitrogen from substitutional to interstitial sites. Since no overall change in lattice constant is found, the nitrogen cannot be diffusing out of the GaNAs layer.

Although, when studying Ga(In)NAs ternary and quaternary alloys, a blueshift was only found in the quaternary GaInNAs alloys [71]. This may imply that different growth conditions could lead to different mechanisms responsible for the blueshift.

Despite the lack of consistency regarding the mechanism of the blueshift, a universal feature is an improvement of photoluminescence (PL) intensity with annealing. The PL intensity is considered a useful technique in providing a figure of merit for the sample. Typically, the lower the defect density, the more radiative recombination occurs which improves the peak intensity value. Improvements to the PL intensity are found across compositions such as GaNAs [72], GaNAsSb [73], GaInNAs [7] and GaInNAsSb [74].

3.5.3 The effect of Sb incorporation in GaInNAs

In this study, antimony is incorporated in the dilute nitride alloys for its impact on the crystal structure as a constituent (further reduces the band gap) and as a surfactant (lowers surface free energy, suppresses surface diffusion, and thus prohibits island formation and phase separation [75]). The incorporation of Sb has been shown to improve parameters such as the photoluminescence intensity [76, 77] as well as allow for the lowest band gap dilute nitride materials in literature [78]. However, the Sb flux during growth is another parameter in a complicated growth process, and optimising the flux requires precise control on factors such as composition, temperature and growth rate [79].

3.5.4 Nitrogen defects and doping type

Previous results show that the defects present in dilute nitride materials play a large role in device performance, hence it is important to know the type and concentration of relevant defects and their thermal stability with annealing.

In most cases, unintentionally doped dilute nitride layers are p-type as grown regardless of whether MOCVD or MBE is used to grow the dilute nitride layer [80, 15, 81]. However, studies into the growth conditions of GaInNAs have found that the as-grown unintentionally doped type is dependent on the temperature [82] and V/III ratio [83] so the defects responsible for the type of GaInNAs are highly dependent on the conditions of the MBE growth. Furthermore, the intrinsic type can switch after a post-growth anneal at temperatures such as approximately 700 °C, much greater than the dilute nitride growth temperature. In the cases of MOCVD-grown GaInNAs layers, annealing encourages the development of an N-H complex which acts as a donor switching overall type to n [84].

However, in the UHV conditions of an MBE chamber, the amount of impurities should be minimised especially compared to MOVCD and so this reasoning should not apply to MBE-grown dilute nitrides. Despite this, Langer et al. [83] report a type switch in GaInNAs at 700 °C from n to p-type. The reasons for the switch could be related to the evolution of nitrogen-related defects with annealing. Xie et al. [85] reported multiple defects in as-grown p-type material which is attributed to both nitrogen-related and the EL2-type defects found in GaAs. Annealing this material had the effect of decreasing the total defect density but increasing the net acceptor concentration due to the introduction of an acceptor level. Furthermore, annealing has been shown to dramatically reduce the concentration of interstitial nitrogen complexes [86] which act as donor defects at

approximately 0.25 eV below the conduction band.

Overall, control over the intrinsic type and the defect concentration is important in device design and careful choice of annealing parameters is required in order to minimise the defect concentration.

3.5.5 Unity gain detectors

One of the earlier detectors that utilised dilute nitrides on GaAs was demonstrated in 1999, a few years after Kondow's proposal. Héroux et al. [87] demonstrated an RCE GaInNAs photodetector which could operate at near 1.3 µm. With an applied bias of 7 V, they achieved a quantum efficiency of 72% and a dark current density of 0.9 mA cm^{-2}.

In 2005, two separate studies achieved detection at 1.55 µm using dilute nitrides. The first study used GaNAsSb quantum wells in between GaAs layers for a total dilute nitride thickness of 14 nm [73]. Furthermore, they investigated the difference in photodiode performance before and after a post-growth anneal. They found significant improvement to the dark current of the device by roughly an order of magnitude from 1 mA cm^{-2} to 0.1 mA cm^{-2}. The responsivity of the photodetectors decreased from 0.016 A W^{-1} to 0.01 A W^{-1} which was caused by the blueshift of the band gap. This responsivity is relatively small compared to expectations set by commercial devices (up to 1.0 A W^{-1}) but is quite substantial considering the thickness of the absorber. For a total GaNAsSb width of 14 nm, the two responsivities would equate to substantial absorption coefficients of 13 000 cm^{-1} and 8000 cm^{-1}, both larger than that for InGaAs at 6500 cm^{-1} and strained Ge at 2000 cm^{-1}. However, the absorption coefficient of this GaNAsSb layer is calculated from a thin quantum well structure, therefore is subject to any uncertainty in the width of this quantum well. A more accurate measurement of the absorption coefficient can be measured on a bulk layer.

The second study of 2005 that utilises dilute nitrides to reach detection at 1.55 µm, uses GaInNAs RCE-PDs to reach a responsivity of 0.42 A W^{-1} [88]. In order to maximise the quantum efficiency and meet the resonance condition required for an RCE-PD, DBRs constructed from 8 and 25 pairs of AlAs and GaAs were used as top and bottom mirrors respectively. A low dark current of 4.3×10^{-5} A cm^{-2} was measured at the operating bias of -5 V. Furthermore, the study was an early example of the speed at which the detector could be operated. They measured a rise time of 800 ps, which is a bandwidth of 440 MHz. This speed is too low for telecommunication applications; however the rise time was independent of the device size and also unlikely to suffer from long transit

times across the 1366 nm intrinsic width. Therefore, the rise time is instrument limited and the bandwidth of this device is like much higher.

Other studies that show photodetectors which can respond to 1.55 µm illumination include Tan et al. [89]. This differs from previously mentioned devices as no quantum well or RCE-PD structure is used. Instead a bulk 500 nm GaInNAsSb layer is used. This study resulted in a device with a responsivity of $0.098\,\mathrm{A\,W^{-1}}$ at 1.55 µm. This results in an absorption coefficient of $2600\,\mathrm{cm^{-1}}$, much lower than that for InGaAs. This could be a result of the band gap of the GaInNAsSb layer ($E_g = 0.77\,\mathrm{eV}$) not reaching a sufficiently low level to allow for more detection at 1.55 µm. However, this is unlikely as the band gap is similar to the dilute nitride alloy grown in the study by Luo et al. [73] and the absorption coefficient does not rise above $1 \times 10^4\,\mathrm{cm^{-1}}$ even at shorter wavelengths. This implies that the collection of photogenerated carriers is inhibited in some way, therefore limiting the quantum efficiency of the device.

Waveguide structures that are not top illuminated like previously mentioned structures can also be fabricated. Loke et al. [90] fabricated GaNAsSb waveguide photodetectors with a detection range up to 1.6 µm with a maximum responsivity of $0.29\,\mathrm{A\,W^{-1}}$. This work was continued, although at a shorter operating wavelength of 1.3 µm by Xu et al. [91] who achieved a responsivity of $0.72\,\mathrm{A\,W^{-1}}$ using AlGaAs cladding layers and Zegouai et al. [92] for high speed operation. In this study, they found an RC-limited bandwidth of 16.5 GHz using 1.3 µm illumination, which is to be expected in waveguide photodetectors.

Another example of a GaNAsSb high speed photodetector is a UTC-photodetector [24] which uses GaAs as the carrier collection layer. The GaNAsSb layer was not intentionally doped, but instead relied on the high unintentional doping concentration of $7 \times 10^{16}\,\mathrm{cm^{-3}}$. At an applied bias of $-12\,\mathrm{V}$ and illumination from a 1.3 µm laser, this detector achieved a bandwidth of 14 GHz. However, it is clear from the photocurrent that multiplication is occurring over the photodiode at this voltage. The effect of this on the bandwidth is not mentioned in the study.

However, this group has not published high speed operation at 1.55 µm. The reason for this is that increased nitrogen incorporation degrades the crystal quality and photodetector performance. To illustrate this, figure 3.3 shows the dark current density of the photodiode against the band gap of the dilute nitride. As the band gap is decreased, the dark current exponentially rises not only because of the lowered band gap but also because of the increased density of nitrogen-related defects. Importantly, the

dark current values in figure 3.3 are not normalised for the same voltages, electric fields or device structure. Therefore, the conclusion taken from figure 3.3 should not be that GaNAsSb is inherently worse than other dilute nitride materials as some of these data points represent functional high-speed devices that sacrifice dark current for operating speed. The aim of this study will be to not replicate this large dark current, but instead approach commercial InGaAs photodetectors with approximately 10 nA in a device with a diameter of 25 µm. This corresponds to a dark current density of 2 mA cm^{-2}.

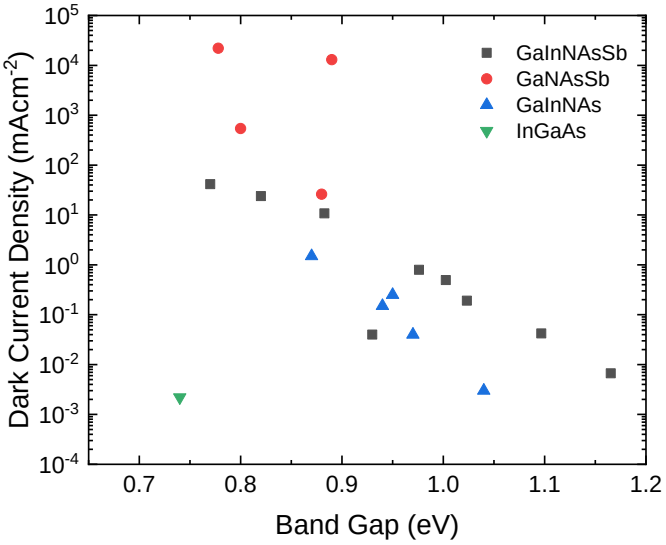

Figure 3.3: The dark current density of various dilute nitride photodetectors against their band gap such as GaInNAsSb [93, 89], GaNAsSb, [91, 90, 24, 94] and GaInNAs [95, 87]. For comparison, an InGaAs photodiode is included [29].

3.5.6 Avalanche Photodiodes

Ideally, for low noise operation, highly dissimilar impact ionisation coefficients are required in APDs. Early predictions of the impact ionisation coefficients of dilute nitrides predicted a drop in the electron ionisation coefficient due to the highly disruptive N atom affecting the conduction band while leaving the valance band unaffected [96]. The reasons for this include an increase in effective mass causing less acceleration and more scattering in addition to the formation of defects including N-N pairs which further encourage scattering before the electron has reached sufficient energy to ionise. Therefore, multiplication initiated by holes could lead to low noise operation.

Kinsey et al. [97] fabricated GaNAs APDs for operation at a short wavelength of 1.06 µm. The results from this study showed a minor improvement as compared to GaAs APDs of a similar intrinsic width with noise results indicating $k = 0.4$ and a gain-

bandwidth product of 42 GHz. The multiplication in this study was electron initiated and was published several years before the prediction of Adams.

In 2013, a more detailed study of the impact ionisation of GaInNAs diodes was published [98]. In this study, Tan et al. find not only a large reduction in α, but a reduction in β as well. Therefore, there is no improvement in the operation of the APD except for the longer wavelength operation as compared to GaAs.

GaInNAsSb SAM APD

Despite the potential advantages of a dilute nitride APD, it would be preferable to design a SAM APD using AlGaAs as the multiplication layer rather than any dilute nitride. The high electric field required for avalanche multiplication would lead to large dark currents in the photodiode. In addition, the use of AlGaAs can lead to incredibly thin multiplication layers which would lead to very low noise operation. As mentioned previously, the thinnest AlInAs/InGaAs APDs include multiplication layers of 100 nm. However, $Al_{0.8}Ga_{0.2}As$ APDs have been demonstrated with $k = 0.13$ with a thickness of 0.15 µm [99]. The AlGaAs layer could be thinned further to 0.02 µm and result in an effective $k < 0.1$ [100]. This result is consistent across a range of multiplication up to $M = 90$. At the electric fields required for this level of multiplication, tunnelling currents would have likely caused a breakdown in the device in AlInAs.

Chapter 4

Experimental Methods

The samples in this study were grown via MBE and then annealed by IQE. They were then transported to Lancaster where they were processed and characterised at the university. Therefore this chapter will only briefly mention the growth aspect of the devices and instead focus on the processing and characterisation methodology.

4.1 The devices

Over the course of this study, there have been four separate campaigns of dilute nitride growth. From each campaign there are multiple growth runs which produce multiple wafers which are then annealed at different temperatures. In this work, in order to track which is being discussed each device will be referred to by its campaign number, its type, n-i-p or p-i-n, its thickness and the annealing condition. For example, a campaign three n-i-p that is annealed at 720 °C is referred to as C3-n1-720. An unannealed sample, or an unannealed point on a graph, will have the reference UnA.

Campaign	Intrinsic thickness (µm)	Annealing Range (°C)	Device Type
1	3.0	785	Homojunction
2	1.0, 1.5	735 - 835	Heterojunction
3	1.0	720 - 750	Heterojunction
4	1.0, 1.5	720 - 750	Heterojunction

Table 4.1: A summary of the four different campaigns and key device differences between them.

Each campaign was designed to investigate a new aspect of the devices. For instance, the range of annealing temperatures investigated for the campaigns changes over the course of the study. First, only one annealing process was applied. In campaign two

a wide range of annealing temperatures were studied. Finally, in campaigns three and four, two focused studies of the annealing temperature were carried out. The reason behind this is that an anneal at 785 °C gave the highest photoluminescence intensity, so it was assumed that this would lead to the highest quality photodetector. This was found to be incorrect in campaign two and therefore influenced the annealing temperatures of campaigns three and four. Table 4.1 summarises the key details of the campaigns, while the full list of the devices measured, along with key parameters such as the band gap, are shown in chapter 7.

In general, campaign four contained the most optimal devices for a detector and therefore many results focus on this campaign. However, campaigns 2 and 3 can help show the journey between the first devices produced by the project in campaign 1 to the final devices suitable for high bandwidth operation. As such, where relevant the results of campaigns 2 and 3 are mentioned.

A major difference from campaign one and the rest is the device type. Campaign one included only homojunction devices that have the electric field of the p-i-n only within the GaInNAsSb. Other campaigns had double heterojunction devices that have an intrinsic GaInNAsSb layer between two GaAs cladding layers that are p and n type doped. The layer structure of a p-i-n homojunction device is displayed on table 4.2, complementary n-i-p was also grown with the same doping concentrations but different types. The layer structure of the double heterojunction devices is shown on table 4.3 and figure 4.1. In all structures, Be is used as the p-type dopant and Si is the n-type dopant. The doping in the top layer in the double heterojunction n-i-p is slightly reduced compared to the p-i-n due to poor activation of dopants in the layer.

Layer	Material	Thickness (nm)	Doping Concentration (cm^{-3})
5	GaAs	500	(p) 1×10^{19}
4	GaInNAsSb	300	(p) 1×10^{18}
3	GaInNAsSb	3000	UID
2	GaInNAsSb	500	(n) 1×10^{18}
1	GaAs	2500	(n) 1×10^{18}
Semi Insulating GaAs substrate			

Table 4.2: The nominal layer structure of the devices in campaign one. Complementary n-i-p devices were grown with the same doping concentration but with opposite type.

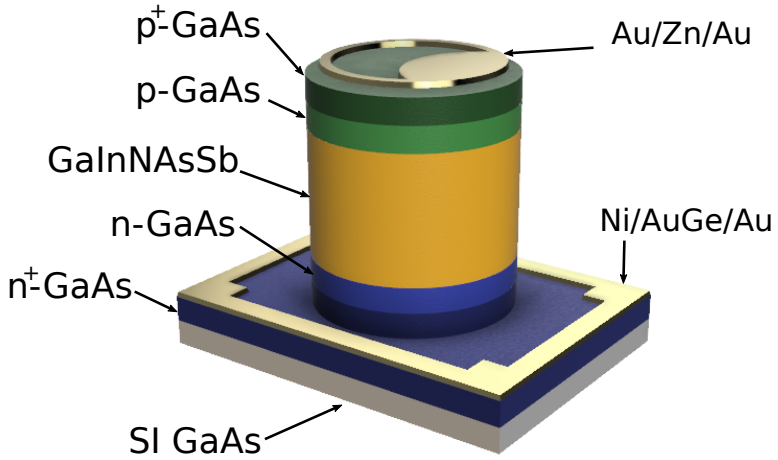

Figure 4.1: A figure showing the layer structure of the double heterojunction *p-i-n* device used in campaigns two to four. Complementary *n-i-p* devices were also grown with equivalent doping concentrations but opposite type.

Layer	Material	Thickness (nm)	Doping Concentration (cm^{-3})	
			p-i-n	n-i-p
5	GaAs	200	(p) 1×10^{19}	(n) 5×10^{18}
4	GaAs	200	(p) 1×10^{18}	(n) 1×10^{18}
3	GaInNAsSb	1000 / 1500	UID	UID
2	GaAs	500	(n) 5×10^{17}	(p) 5×10^{17}
1	GaAs	1000	(n) 2×10^{18}	(p) 2×10^{18}
Semi-insulating GaAs substrate				

Table 4.3: The nominal layer structure of the double heterojunction devices used in campaigns two, three and four.

4.1.1 Post growth anneal

The anneals were done using a rapid thermal annealing (RTA) system. This allows for the annealing process to take place inside a nitrogen atmosphere to inhibit the formation of oxides. A GaAs substrate is used as a cap layer to prevent any arsenic desorption at high temperatures. The peak temperature was changed for difference devices, but the time at this temperature was kept consistent at 20 s.

4.2 Device fabrication

In this work, there are two photomasks that have been used to fabricate the devices. The simplest device is from the *mixed area* mask which features circular mesas that

have diameters that range from 25 µm to 800 µm. Typically, only the properties of larger mesas with diameters greater than 100 µm are measured as the devices are tested by direct probing, which is easier for larger devices. Two metal contact evaporations and a mesa-defining etch step are required to fabricate devices similar to that in figure 4.1 with an image of the example of the devices under test shown in figure 4.2.

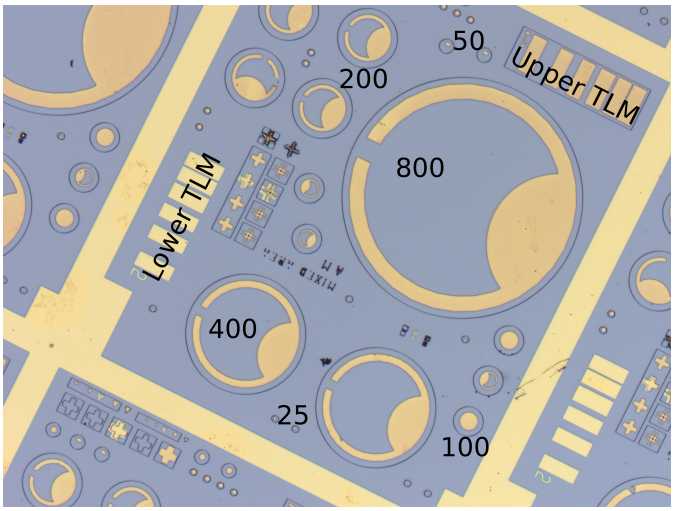

Figure 4.2: An image of a finished simple photodiode. Device diameters are labelled with units of µm along with the transmission line measurement (TLM) gold pads further described in section 4.2.3.

However, for high bandwidth measurements a more complicated photomask is required to allow for testing of smaller devices and the use of a ground-signal-ground probe. Remote bond pads are positioned away from the two contact layers to an insulating layer either provided by the undoped substrate or a layer deposited by PECVD (see section 4.2.5). In this study, we use SiN_x to provide an insulating ramp for remote bond pads to reach the required contact level from the insulating substrate layer. An illustration of this is shown in figure 4.3.

4.2.1 Photolithography

In order to create a pattern for the contacts, SiN_x or a mesa etch, photolithography is required. This technique uses the selective exposure of ultraviolet light to a photosensitive resist on the substrate. This resist is spin coated on the substrate pre-exposure to distribute it evenly. Typical exposure parameters would use a wavelength of 365 nm at an energy density of 30 mW cm^{-2}. The exposed resist is then dissolved in Microposit MF CD-26 developer.

The resists that are used depend on the next processing step. For etching purposes,

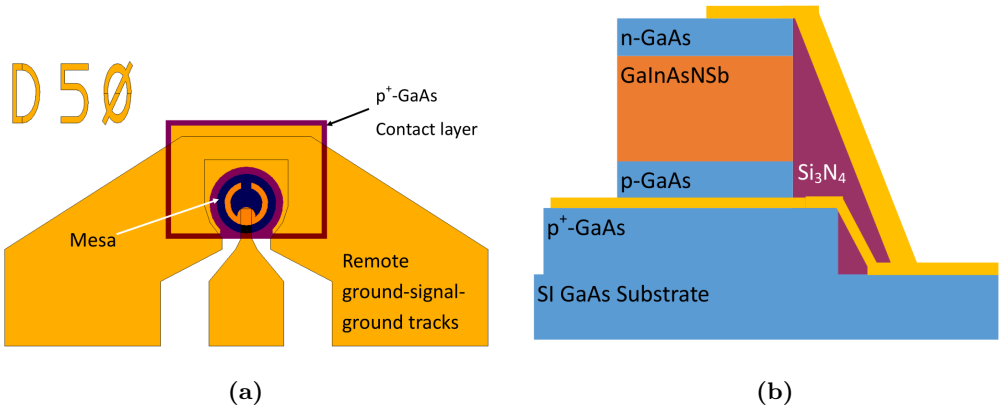

Figure 4.3: A schematic diagram of the device suitable for bandwidth measurements from the (a) top and (b) side.

S1813 is spun at a speed between 4000 rpm and 6000 rpm for 60 s and then baked at 115 °C. However, for the purposes of thermal evaporation, an undercut is required, and so a lift-off resist, LOR3A, is spun first directly on the GaAs substrate at a speed of 3000 rpm for 30 s and baked for 5 minutes at 180 °C.

The S1813 can easily be removed by acetone, however after a thermal evaporation it is cleaner to use an NMP-based remover which is heated to 70 °C and can effectively strip LOR3A.

4.2.2 Thermal evaporation of ohmic contacts

The process for thermally evaporating metals involves heating a tungsten basket in which the source material is placed. A current is passed through the basket which is heated by Joule heating. The evaporation takes place inside a vacuum of $<1 \times 10^{-5}$ mbar to avoid contamination of the contact.

The thickness of the metal that is being deposited is monitored using a quartz crystal microbalance (QCM). This uses the piezoelectric effect to vibrate the crystal using an alternating current. The resonant frequency at which it vibrates is decreased when material is evaporated onto the crystal. Therefore, this frequency change can be used to calculate the thickness of the metal evaporated using the density and the Z-Ratio of the metal. This Z-ratio is the ratio of the acoustic impedance of the quartz crystal with the metal. A tooling factor can also be applied to account for any differences between the thickness displayed by the QCM and the true thickness measured by a surface profiler. This difference could be caused by positional differences in the chamber of the QCM and the samples.

In order to obtain Ohmic contacts, which are without any rectifying Schottky barrier, a correct choice of metals need to be selected which change depending on the semiconductor and the type of doping present in the contact layer. For instance, Au/Zn/Au contacts were used for p-type GaAs [101] whereas Ni/AuGe/(Ni)/Au [1] or InGe/Au contacts are used for n-type GaAs. In each case, the first metal to be evaporated in the left-most metal in the format A/B/C.

For the Au (10 nm)/Zn (20 nm)/Au (200 nm) contact, the first Au layer is required to improve the adhesion of the Zn to the surface [101], while also being thin enough to allow for Zn to diffuse through to the GaAs to provide extra p-type doping to the layer. The top Au layer prevents any loss of Zn during annealing and provides a suitable surface for probing.

The n-type contacts used in this study varied. Simpler InGe (20 nm)/Au (200 nm) contacts can be evaporated more quickly than triple-layer contacts as less time is spent heating the third tungsten coil. However, for high quality low resistance contacts required in devices for high bandwidth operation, the contact Ni (5 nm)/AuGe (100 nm)/Ni (35 nm)/Au (100 nm) is used. The first Ni layer provides improvements to the adhesion of the contacts to the GaAs surface while also providing a favourable interface for current to flow once annealed [102]. The second Ni layer is required as the AuGe will lose its morphology and form balls on the surface of the contact. The low surface tension of Ni prevents this from occurring. The AuGe mix is 88% Au and 12% Ge by mass. This forms a eutectic alloy with the lowest melting point of any mix of Au and Ge.

4.2.3 Optimising the contact resistance

For high frequency operation, there is a need to minimise both the capacitance and the resistance of the device in order to maximise the RC bandwidth. The capacitance depends on the depletion width and the size of the mesa, but the resistance is mostly determined by the processing steps. Therefore, an optimised process was found to minimise the contact resistance of the photodiodes intended for high bandwidth operation. In order to achieve this, transmission line measurements (TLM) were applied to the evaporated contacts. This involves measuring the total resistance between a pair of contacts, of width w which are separated by a known distance such as in figure 4.4b where $L_3 > L_2 > L_1$. The total resistance (R_t) is given by

[1] The 2nd Ni layer is only required for annealing small contacts <25 µm

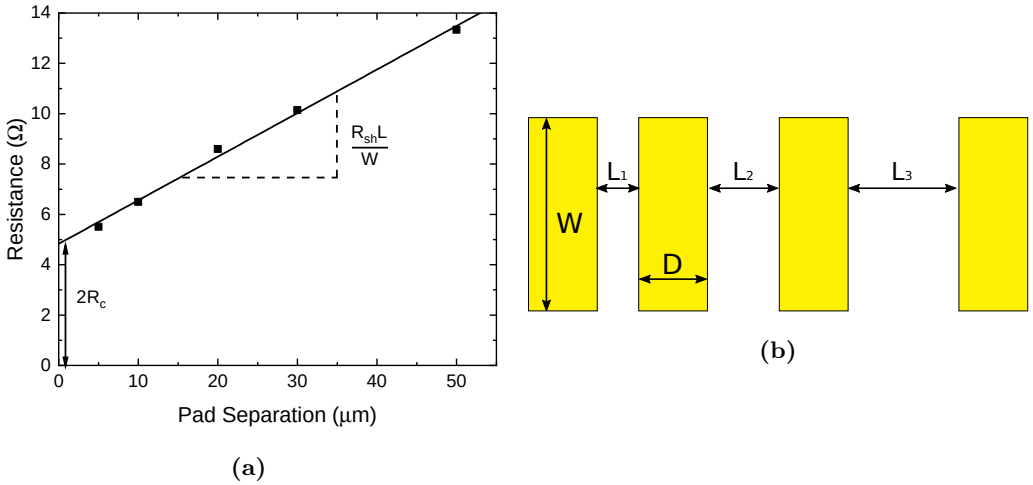

Figure 4.4: (a) The resistance measured from adjacent TLM pads is plotted against their separation distance to find the contact and sheet resistance. The resistance of the cables was not accounted for in this data. (b) An illustration of the TLM pads showing the increasing distance between adjacent pads.

$$R_T = 2R_m + 2R_c + R_{semi} \tag{4.1}$$

where R_m is the resistance of the metal, R_c is the contact resistance and R_{semi} is the resistance due to the semiconductor. The addition of R_m can be ignored as it is likely much lower than that of R_c and R_{semi} and the semiconductor resistance can be given as $R_{sh}\frac{L}{w}$, where R_{sh} is the sheet resistance of the semiconductor. Therefore, the plot of R_t against L should intercept the y-axis to give $2R_c$. An example of this is shown in figure 4.4a.

In order to minimise R_c, after the photolithography is completed, the surface of the semiconductor is cleaned with an O_2 plasma at 75 W with a flow rate of 15 sccm. However, this step appeared to increase the contact resistance as compared to a sample which had no plasma etch applied even after an alloying step. Therefore, it was concluded that the oxygen plasma may have introduced a thicker oxide to the GaAs and a chemical oxide removal step with a 1:1 HCl : H_2O was applied for 10 s. Since no H_2O_2 is present to oxidise, only the GaAs oxide is dissolved. Unfortunately, the native oxide will reform as the sample is exposed to air after the etch is complete before entering the thermal evaporator. Therefore, the time between the oxide removal and the low-pressure environment of the thermal evaporator is minimised.

After the evaporation and lift-off steps, the Ni-based contacts require annealing. Previous studies have found annealing at 400 °C to give the lowest contact resistance.

Figure 4.5 shows the contact resistance as measured by TLM for a range of anneal temperatures where the sample has received an oxygen plasma ash and an oxide removal step. The resistance measurement did not take into account the resistance of the system. The optimal anneal temperature for the Ni/AuGe/Ni/Au layers in this study is 380 °C for 30 s. This is close but not exactly equal the optimal resistance for the p-type contact, Au/Zn/Au, but due to the size difference between the top and bottom contact, it is crucially important that the top contact is of low resistance.

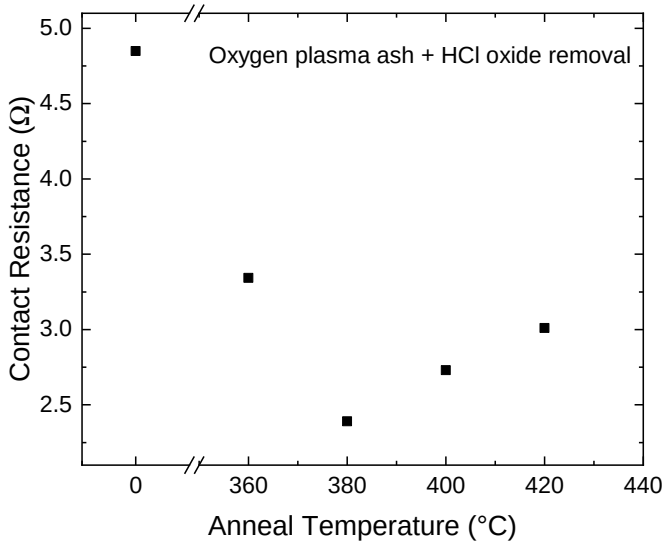

Figure 4.5: The optimisation of the annealing temperature of contacts. the samples were placed at the temperature stated for 30 s in a N_2 atmosphere for the Ni/AuGe/Ni/Au based contacts.

This optimised resistance, divided by the width of the TLM pad gives a value of 0.37 Ω mm. Previous studies indicate that this value could lie within 10^{-1} to 10^{-2} Ω mm [102, 103, 104], so there is likely some room for improvement, but the contact resistance will not likely decrease further without significant changes to the process. It is possible to predict the series resistance due to the contacts by calculating the area of the top contact and multiplying the contact resistance by the ratio of the area of the top HBW contact and the area of the TLM pad. For a device with a nominal 25 µm diameter, this would result in a contact resistance of 110 Ω if the optimal annealing case in figure 4.5 is repeated. The RC time constant can be calculated from equation 2.25 with a 1 µm depletion width to be over 20 GHz, exceeding the requirements for 10 Gb/s operation. However, this is likely an overestimation due to the difficulty of repeating the lowest resistance condition and any parasitic capacitance present in the device.

4.2.4 Mesa wet etching

In order to isolate circular mesas for test, a wet etch composed of H_2SO_4:H_2O_2:H_2O with a composition of 1:8:80 was used. The benefit of this etch is a uniform etch rate of approximately $550\,\mathrm{nm\,s^{-1}}$ for GaAs, $Al_xGa_{1-x}As$ and various dilute nitride compositions.

One feature of a wet etching is its anisotropic nature. Although only a significant issue in small mesas, it is important to orientate the device for processing in the correct direction. This is especially important for the high bandwidth designs as the mesas are much smaller and so more sensitive to any anisotropic differences. The different etch profiles were investigated previously by Shaw [105] and then experimentally shown to be similar as shown in figure 4.6. From the figure, the $(00\bar{1})$ direction appears to be sloped whereas the (011) direction has a sharp edge. This means that contacts can more easily track down from the mesa to the semi-insulating substrate. This effect will be present in all etched surfaces but has a greater impact on features roughly the size of 30 µm or smaller.

As the etch results in a device which no longer has the nominal diameter initially designed with, the actual dimensions of the devices are measured using an optical microscope, scale bar printed on a glass slide and a camera connected to a PC. The camera can be used to measure the on-screen length of 100 µm. This is compared to four separate measurements of the devices and an average is taken. For the purposes of calculating current and capacitance density, the devices are assumed to be circular with a diameter of this average value.

4.2.5 PECVD

Plasma-enhanced chemical vapour deposition (PECVD) is a technique to deposit films from a vapour source to a solid surface. In this study, the gases NH_3 and SiH_4 were used in order to deposit Si_3N_4 onto the GaAs surface. The purpose of this was not only to passivate the GaInNAsSb sidewalls, but also to provide an insulating surface for remote bond pads to reach the semi-insulating substrate from the Ohmic contacts.

It could be also be used for anti-reflection coatings given precise control over the thickness of the SiN_x layer.

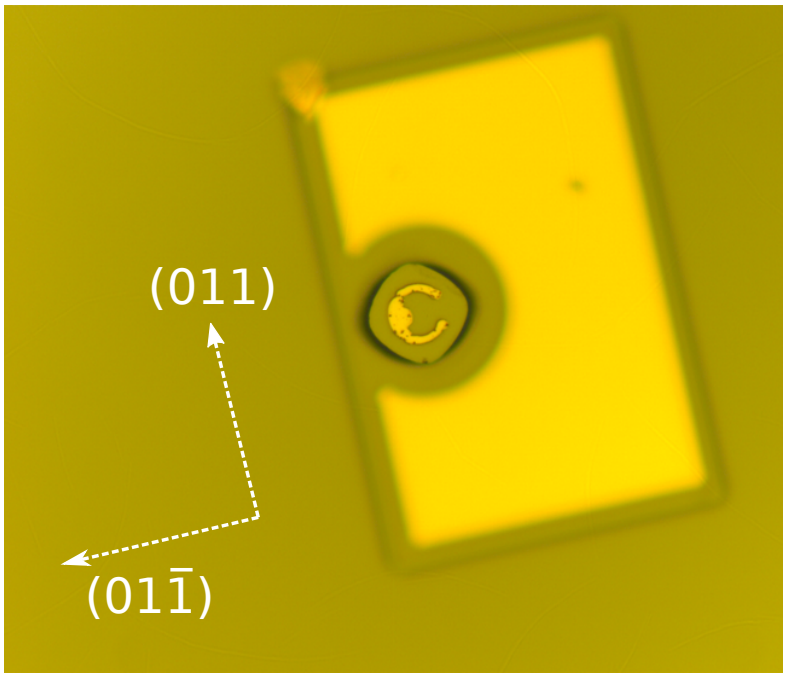

Figure 4.6: A comparison of the 1:8:80 H_2SO_4:H_2O_2:H_2O etch with different crystal directions on GaAs on a device with a nominal diameter of 25 µm.

4.2.6 RIE

Reactive ion etching (RIE) is a process that relies on accelerated ions to both physically and chemically etch a surface. In this study it is used to clean surfaces using a low power O_2 etch and also to etch windows in the SiN_x layer for high bandwidth devices using a mixture of O_2 and CHF_3.

Dry etching was not used in this study as the wet etching recipe was found to be highly repeatable and reproducible and, whereas the dry etching recipe can burn the patterned resist and prove difficult to remove, cleaning the sample of resist after a wet etch is possible using a simple acetone soak.

4.3 Optical characterisation

4.3.1 FTIR transmission

In order to measure the absorption coefficient of the GaInNAsSb material, Fourier Transform Infrared Spectroscopy (FTIR) was used to measure the transmission (and therefore absorption) of the material as a function of wavelength.

Fourier Transform spectroscopy relies on a Michelson interferometer where light from an IR source is directed onto a beam splitter creating two separate paths. One beam is directed back at the beam splitter by a fixed mirror and another is incident on a moveable

mirror. The light from these two beams will then interfere as they are directed towards the detector to produce the resultant interferogram. Over time, the interferogram will be a series of peaks and valleys as the moveable mirror creates constructive or destructive interference for the wavelengths emitted from the light source.

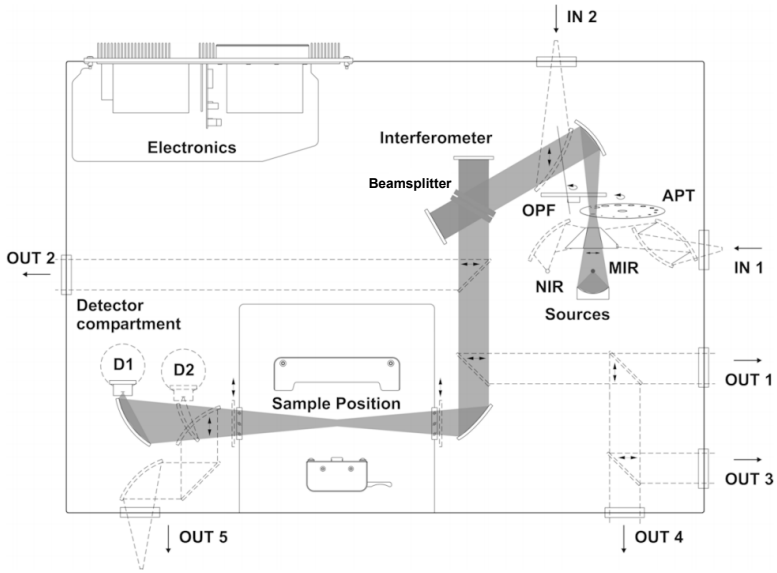

Figure 4.7: A schematic diagram of the internal beam path (marked in dark grey) of the FTIR. The dashed lines represent other optional configurations for beam path. However, in this study only the marked one is used. Figure adapted from Vertex 70 manual [106]

On its own, the interferogram provides little in terms of analysis, however the Fourier transform from time to frequency domain will provide the spectral information about the light source and absorption due to any sample or atmospheric conditions.

In practice, to obtain absorption data for a device, first a background scan is taken to measure the output of the source. The ratio of the measurement with the sample and the background scan will give the proportion of light transmitted through the sample without the effect of the wavelength dependent intensity of the source. Typically, a measurement is also taken with a GaAs substrate without a GaInNAsSb epilayer to account for any loss of signal due to reflection so that the overall transmission (T) due to the epilayer is calculated from the ratio with the transmission through the whole sample (T_{sample}). At room temperature the wafers are attached to a metal sample holder. The sample holder is a flat metal plate with a circular aperture with diameter 2 mm to allow light through. The detector used is either made of InSb or a pyroelectric DLaTGS detector. The DLTaGS detector was used primarily throughout this study, as the InSb detector requires cooling to 77 K. However, the InSb detector has a higher signal to noise ratio particularly at wavelengths around 1.0 µm. These wavelengths are not the target of the

study and so both detectors are suitable.

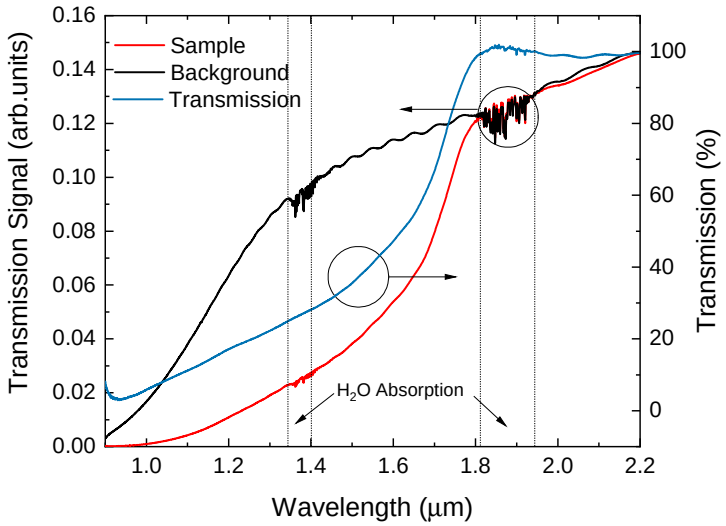

Figure 4.8: The signal received by the FTIR during the background measurement (black) and with the sample (red) for transmission measurements in the cryostat. The resultant percentage of transmitted light (blue) is also shown. The regions defined by the dashed line show wavelengths where water absorption is significant.

Figure 4.8 shows a sample spectrum from the FTIR. The black line is the raw transmission data generated from the blackbody source passing through a GaAs wafer and the red line shows the transmission data when the GaInNAsSb sample is placed in the holder. Since the reduction in transmission signal can solely be attributed to the GaInNAsSb layer, the percentage of light transmitted by this layer is given by equation 4.2 and is shown in blue on figure 4.8.

$$T = \frac{T_{\text{sample}}}{T_{\text{substrate}}} \tag{4.2}$$

The absorption coefficient can then be calculated from Beer's Law in equation 4.3. In the measurement displayed in figure 4.8, the baseline error in the absorption coefficient will be negligible as the transmission beyond 1.8 µm in the GaInNAsSb matches that for GaAs and therefore 100% of the light that passes through the GaInNAsSb epilayer is transmitted giving an absorption coefficient of $0\,\text{cm}^{-1}$ using equation 4.3.

$$\mu = -\frac{1}{W}\ln T \tag{4.3}$$

The model does make the assumption that no light is reflected on the interface between GaAs and GaInNAsSb. This is assumed to be negligible compared to the reflection on the air-GaAs interface due to the differences in refractive index of $n_{air} = 1$

and $n_{GaAs} = 3.3$. This difference would reflect approximately 30% of the light normally incident on the surface as given by equation 4.4. The refractive index of the dilute nitride layer is not known to the same precision, though previous studies have predicted a refractive index of 3.4 [107] and 3.6 [108]. This gives a maximum value for reflection of 0.2%.

$$R_s = \frac{(n_1 - n_2)^2}{(n_1 + n_2)^2} \tag{4.4}$$

The importance of the absorption coefficient comes not only from finding out the amount of light that can be absorbed, but it also helps find various parameters such as the band gap or the Urbach energy. The band gap is found from the linear extraction of μ^2 against photon energy to $\mu^2 = 0$. The energy of this point is the band gap. The Urbach energy is found from the gradient of the natural log of the absorption coefficient beyond the band gap energy. An example of the absorption coefficient extrapolation and the Urbach tail is shown in figure 4.9.

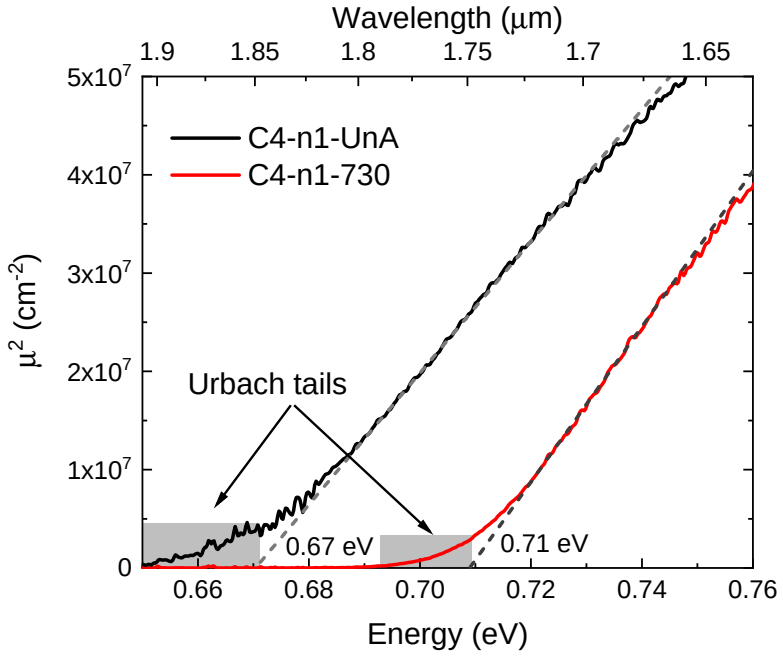

Figure 4.9: The measurement of the band gap and the presence of Urbach tails in two samples, C4-n1-UnA and C4-n1-730. Noise in the black line is caused by water absorption in the atmosphere.

In order to measure the absorption at temperatures other than room temperature, a cryostat was used instead of the magnetic sample holder. In this situation, the cryostat mount fixes the sample in between a temperature-controlled copper and acrylic plate. Light is allowed into the cryostat by a ZnSe window before it passes through the sample

and out again through another ZnSe window. The light allowed through the sample is ideally constant throughout the experiment. Small changes in the position of the sample holder and the cryostat between measurements and the background measurement may impact the resultant spectrum that reaches the detector. Furthermore, only the InSb detector was used, due to the reduction in signal from reflection on the ZnSe windows not overcoming the noise in the DLaTGS detector.

As the sample cannot be removed from the cryostat once the liquid nitrogen has been added (to maintain the vacuum), a background scan cannot be run during the experiment and separate GaAs transmission measurements cannot be taken. Therefore, the background scan was done before any cooling has occurred with the cryostat in place with a GaAs wafer placed in the sample holder.

As the experiment progressed, the baseline absorption coefficient drifts from zero to $1000\,\mathrm{cm}^{-1}$. This is caused by a change in the lamp spectrum highlighting the need for a new background measurement. This was found by comparing the raw transmission through the wafer at room temperature before and after cooling. This showed that the background measurement should be increased by wavelength dependent factor between 1.05 and 1.15. Applying this new background to the high baseline measurements gave a more reliable absorption coefficient and band gap. This was verified by comparing the absorption coefficient at room temperature.

From the temperature dependence of the absorption coefficient, the band gap as a function of temperature can be extracted. These results should follow the Varshni empirical formula [109] given in equation 4.5, where E_0 is the zero kelvin band gap, α and β are fitting parameters that are loosely related to the band gap entropy as $T \to \infty$ and the Debye temperature respectively [110].

$$E_g(T) = E_0 - \frac{\alpha T^2}{T + \beta} \tag{4.5}$$

4.3.2 Laser based quantum efficiency

A key parameter in detectors is the quantum efficiency (QE) or the responsivity (R) of the device. Both quantities are related to the amount of photocurrent generated by incoming light by either considering the ratio of photogenerated electrons to the incoming photons (QE) or the ratio of the photocurrent to the incoming power (R). All of the lasers illuminate the device via an optical fibre coupled to the laser. The fibre tip is attached to a microadjuster which allows for fine adjustment of the fibre. Typically, for

an accurate measurement of QE, a device of diameter 400 µm was used as this diameter is much greater than the diameter of the core of the fibre which ensured all of the light would fall onto the surface of the device.

In order to verify the power of the laser, a commercial Ge diode with a wavelength range of 800 to 1800 nm is used with a known responsivity curve ranging from 0.2 to 0.95 A W^{-1}. Typically, in this study, no anti-reflection coating is applied to the samples. Therefore, roughly 30% of the incoming light is reflected at the air-GaAs interface. The quantum efficiency in this case is referred to as the external quantum efficiency (EQE). Conversely, the internal quantum efficiency assumes that no photons are reflected on the surface and is therefore the highest possible efficiency achievable by that particular device. Most studies calculate this value from the EQE rather than apply an anti-reflection coating by dividing by (1-R_s).

4.3.3 Spectral quantum efficiency

In order to obtain the spectral quantum efficiency, a lamp and monochromator are used. The equipment used in this experiment is the PVE300 system from Bentham. The apparatus is displayed on figure 4.10. It employs a chopped broadband signal and measures the photocurrent across a range of wavelengths by use of a monochromator sampling specific wavelengths. A bias is placed across the photodiode using a separate Keithly 2400 SMU. The quantum efficiency is calculated from the photon flux measured using detectors supplied with the PVE300 system. The wavelength range of the experiment depends on the reference detectors used such as Si for 300 to 1100 nm, Ge for 800 to 1800 nm or PbSe for beyond 1800 nm.

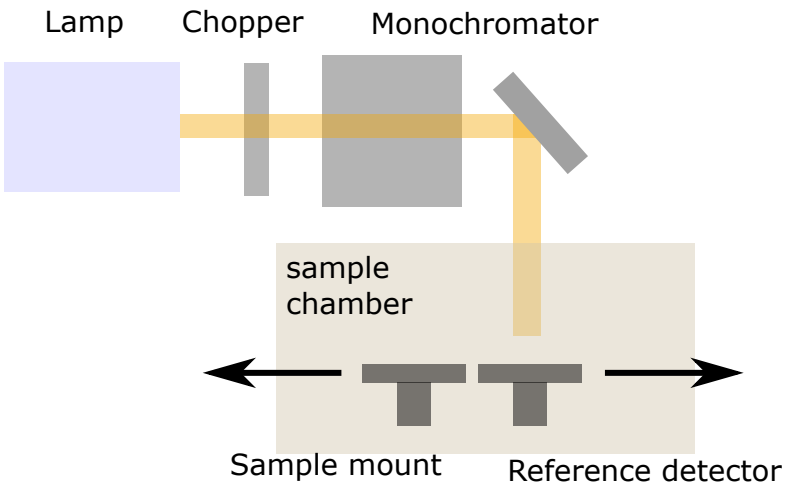

Figure 4.10: A schematic diagram of the spectral quantum efficiency equipment. The position of the reference detector and sample plate is controlled by software and the beam is kept in place.

The spot generated from the monochromator is maintained at a size of $3.42\,\mathrm{mm}^2$ which overfills the fabricated GaInNAsSb photodiodes but not the reference diodes. First of all, this means that only the devices that etched through to the GaAs contact layer are valid in this set up, otherwise light absorbed outside of the etched mesa and the carriers can contribute to photocurrent. Secondly, this means that the raw quantum efficiency as measured by the PVE300 system will be less than the real value for QE. It will have to be normalised according to the ratio of the device area and the spot area. This will include subtracting the area of the metal contact placed on the device.

4.4 Electrical characterisation

4.4.1 Current-voltage

The current-voltage (IV) characteristics of the devices, either in the dark or illuminated by a light source, were measured using a Keithly 2400 source meter controlled by an external LabView program.

Typically, in p-i-n photodiodes, the reverse dark current is determined by bulk currents that are limited by the device area that allows the flow of current. However, in some cases, there may be surface currents present which scale with the perimeter of the device. They can be separated out into two separate components like in equation 4.6 for a circular mesa with radius r.

$$I = \pi r^2 J_{bulk} + 2\pi r J_{surface} \tag{4.6}$$

Dividing the equation by the area of the circular mesa gives

$$J = J_{bulk} + \frac{2}{r} J_{surface} \tag{4.7}$$

which means that the individual components of the total current density can be separately found from the intercept and gradient of the plot of current density and $2/R$.

The temperature dependence of the IV was measured using a Lakeshore TTPX cryogenic probe station and a Keithly 2450 Sourcemeter where possible. The Keithly 2450 is capable of a lower noise floor measurement at the cost of a greater measurement time which is preferable for low current measurements at low temperatures. With the temperature dependent measurements, it is possible to find the dominant current mechanism in the device. The dark current is expected to follow the relation in equation 4.8.

$$J = AT^n \exp\left(\frac{E_a}{k_B T}\right) \tag{4.8}$$

Where E_a is a characteristic activation energy, n is a value dependent on the current mechanism and J is the dark current. For diffusion based dark current, E_a should be approximately equal to the band gap and n should be equal to 3. However, for Shockley-Read-Hall (SRH) current caused by mid-gap states, the activation energy is half the band gap and n is equal to $\frac{3}{2}$. In many studies, the T^n factor has little effect on the results compared to the exponential dependence on the activation energy and is ignored.

4.4.2 Capacitance-voltage

The capacitance - voltage (C-V) measurements are possible through superimposing an AC voltage upon a DC biasing voltage. The AC signal typically has a frequency of 1 MHz and an amplitude of 25 mV. The complex impedance of the device is measured which is used to calculate parameters such as the capacitance and conductance. The phase difference between the applied and measured AC signals was measured and verified to be close to $-90°$ in order to show the device under test was behaving like a capacitor.

In order to measure the unintentional doping concentration in the intrinsic layer, equation 4.9 can be used providing that the concentration of the intrinsic layer (N_i) is much lower than that for the p or n cladding layer adjacent to the p-n junction [111].

$$N = \frac{-2}{q\epsilon A^2 d\left(1/C^2\right)/dV} \tag{4.9}$$

4.4.3 Modelling the capacitance

The capacitance of a device with an arbitrary number of layers can be modelled by solving Poisson's equation in one dimension. For instance, in a three-layer device, the electric field (D) at the boundaries can be calculated as

$$D_1 = qN_1X_1 \tag{4.10}$$

$$D_2 = D_1 + qN_2X_2 \tag{4.11}$$

$$D_2 = -qN_3X_3 \tag{4.12}$$

where N_n and X_n are the doping concentration and the depletion width of layer n. A layer is said to be fully depleted when X is equal to the layer thickness. Eliminating electric field in these equations by substitution yields the following equation:

$$X_3 = \frac{-qN_1X_1 - qN_2X_2}{qN_3} \tag{4.13}$$

Furthermore, the voltage applied to the device, in addition to the built-in voltage of the p-i-n (V_{bi}), is related to the integral of the electric field so that:

$$V = \frac{1}{2}\left(\frac{D_1 X_1}{\epsilon_1} + \frac{D_2 X_3}{\epsilon_3} + \frac{(D_1 + D_2)X_2}{\epsilon_2}\right) \tag{4.14}$$

By substituting equations 4.10 to 4.13 into equation 4.14, a quadratic equation in X_1 is obtained that can be solved by equation 4.15 with the coefficients stated in equations 4.16 to 4.18.

$$X_1 = \frac{-b + \sqrt{b^2 - 4ac}}{2a} \tag{4.15}$$

$$a = N_M\left(\frac{1}{\epsilon_1} - \frac{N_1}{N_3\epsilon_3}\right) \tag{4.16}$$

$$b = 2N_1\left(\frac{X_2}{\epsilon_2} - \frac{N_2 X_2}{N_3\epsilon_3}\right) \tag{4.17}$$

$$c = \frac{-\left(N_2 X_2\right)^2}{N_3\epsilon_3} + \frac{X_2^2 N_2}{\epsilon_2} - \frac{2V}{q} \tag{4.18}$$

The same procedure can be applied to increasing amounts of layers with any number of layers provided there is only one pn junction. For an arbitrary number of layers where m and n are the outermost layers in the p and the n side respectively by equations 4.19 to 4.21.

$$a = N_m\left(\frac{1}{\epsilon_m} - \frac{N_m}{N_n\epsilon_n}\right) \tag{4.19}$$

$$b = 2N_m\sum_{k=m+1}^{n-1}\left(\frac{X_k}{\epsilon_k} - \frac{N_k X_k}{N_n\epsilon_n}\right) \tag{4.20}$$

$$c = \frac{-\left(\sum_{k=m+1}^{n-1} N_k X_k\right)^2}{N_n\epsilon_n} + \sum_{k=m+1}^{n-1}\left(\frac{X_k^2 N_k}{\epsilon_k}\right) + \sum_{k=m+1}^{n-2}\left(2N_k X_k\sum_{l=k+1}^{n-1}\left(\frac{X_l}{\epsilon_l}\right)\right) - \frac{2V}{q} \tag{4.21}$$

The depletion in the outermost n-type layer, X_n, is then calculated simply by balancing the charges on either side of the junction. This is shown in equation 4.22.

$$X_n = \frac{\sum_{k=0}^{n-1} N_k X_k}{N_n} \tag{4.22}$$

In order to find the outermost layers that include any depletion width, X is calculated for the layers either side of the electrostatic junction, and if it is greater than the thickness of the layer, the depletion of the next layer should be considered. This next layer should

be found by considering which side of the p-n junction, has less charge available and expanding the range on that side.

From here, the capacitance of the device can be calculated by the summation of each layer's contribution to the capacitance by treating the device as many parallel plate capacitors in series.

$$C = \frac{A}{\sum_n^m \frac{X}{\epsilon}} \tag{4.23}$$

4.4.4 Intrinsic type test

The type of the dopant in the intrinsic region cannot usually be identified by C-V methods. Typically, this is found by Hall measurements on samples grown especially for this purpose, but due to the complications of growth and repeatability it would be ideal to find the doping type on fabricated samples. So instead, an alternative method was used in this study. Another device was fabricated from the same wafer where, instead of placing the lower contact on the GaAs layer, it was placed approximately halfway through the intrinsic GaInNAsSb layer. The I-V characteristic of this partially etched device would then be measured over a range of device sizes and compared to devices that are fully etched. Therefore, if the electrostatic junction was at the top of the sample, the same characteristics would be expected for the partially etched device. The area of the electric field would be confined to the etched area and produce an area scaled dark current. However, if the junction forms below the etched surface, the current scaling by device area is expected to be lost. Therefore, by these measurements and knowledge of the device structure, it is possible to find the doping type of the intrinsic region.

The importance of this measurement is two-fold. First of all, due to changes in the doping concentration with annealing temperature, it is important to be able to detect if the dominant carrier type has changed. Secondly, when designing APD structures, it is important to have very fine control over the electric field in the absorber layer, therefore it is important to know the position of the junction in the device and keep it far away from the absorber layer.

4.4.5 Admittance spectroscopy

Admittance spectroscopy is a tool developed by Losee [112] and later Walter et al. [113] for finding the discrete energy level for traps in the semiconductor. This technique uses the variation of capacitance and conductance of the junction as a function of temperature

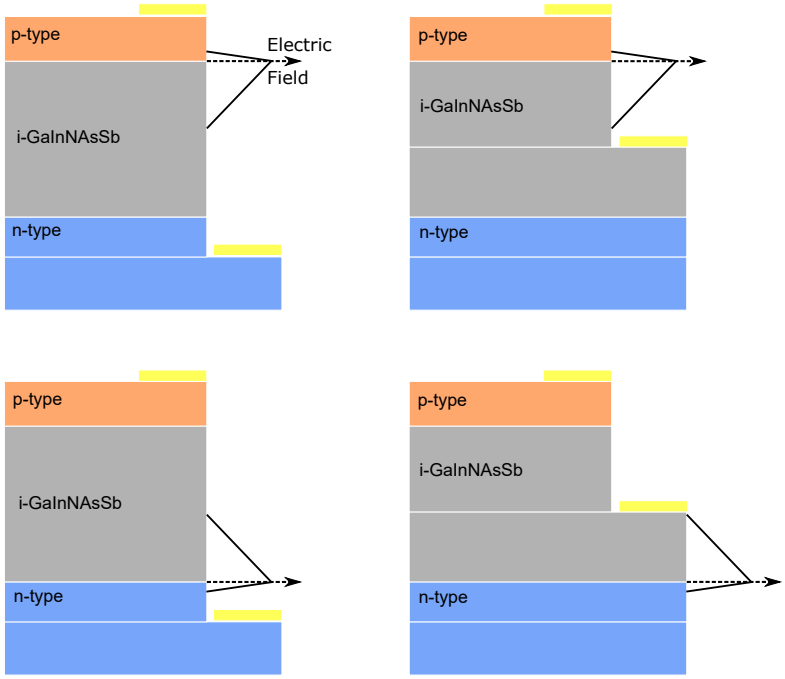

Figure 4.11: The device layer structure and electric field profile of the fully etched samples (left) and partially etched devices (right) for a n-type (top) and p-type (bottom) intrinsic layers. The electric field is contained in the etched area for all samples but the bottom right.

and frequency to probe the thermal emission rates of various trap levels. These variations are a consequence of carrier trapping and detrapping between the defect energy level and the Fermi level. If the applied frequency matches the temperature dependent carrier emission frequency, the conductance will give a peak value related to the emission rate of the trap [114].

$$\omega_0 = 2\tau_0^{-1} = 2\mathbb{E}T^2 \exp\left(-E_a/kT\right) \tag{4.24}$$

$\mathbb{E}$ is the pre-exponential factor which contains the capture cross section, the average thermal velocity and the effective density of the conduction or the valence band all divided by T^2. Overall, the factor is temperature independent. It is found from the y-intercept of a $\ln \frac{\omega_0}{T^2}$ against $\frac{1}{T}$ plot.

The defect distribution can be calculated from the equations

$$E_\omega = kT \ln \frac{2\mathbb{E}T^2}{\omega} \tag{4.25}$$

$$N_T(E) = -\frac{V_{bi}^2}{kTW\left(qV_{bi} - (E_F - E_\omega)\right)} \frac{dC}{d\ln\omega} \tag{4.26}$$

In equation 4.26, W is the depletion width as calculated by 2.12, E_F is the position

of the Fermi level in the bulk of the semiconductor with respect to the closer band edge and N_T is the defect density of state with units of $\mathrm{cm}^{-3}\mathrm{eV}^{-1}$. Therefore, the actual defect density can be measured by integrating the area underneath the N_T against E_ω plot. This can be achieved using a Gaussian fit

The limitations of equation 4.26 arise from uncertainty in knowing V_{bi} and E_f. Both parameters influence the magnitude of the measured defect density but cannot always be extracted reliably from experimental results.

Complications arise with this method when determining the origin of defect present in the material. For instance, Islam et al. [115] describes the difference between bulk type defects that are homogenous throughout the GaInNAsSb layer and localised traps at the interface between two materials. In order to differentiate the two, the bias dependence of the conductance peak is found. For a bulk trap, the applied bias should have no effect on the crossing level of the Fermi level and the defect level. Therefore, the conductance peak should not change with applied bias for a bulk distributed defect. Islam et al. also discuss carrier freeze out which gives a trap-like signature in admittance spectroscopy, although only at temperatures below 77 K. Therefore, in this study, we should only consider the difference between bulk and inter-facial traps. Furthermore, the use of full GaInNAsSb homojunction devices should eliminate the possibility of interface related traps.

4.4.6 Bandwidth

In order to measure the 3dB bandwidth for our devices, the output signal of a 1.55 µm laser was modulated by use of an electroabsorption modulator (EAM). The attenuation of the EAM was controlled by an RF signal generator which resulted in large extinction ratio dependent on the voltage applied. The signal generated in the GaInNAsSb photodiode in response to this laser was then measured using a microwave transition analyser. This is shown schematically in figure 4.12. The internal system frequency response is separately measured without the photodiode and must be taken into account when measuring the frequency response of the photodiode. The response can be normalised by subtracting the low frequency signal (i.e. at less than 500 MHz) from the high frequency signal to find the 3 dB bandwidth.

To verify these results, some measurements were made at Cardiff University. The illumination was provided by a Thorlabs MX40B which operates at a wavelength of 1.55 µm up to a speed of 40 GHz. The signal generated by the photodiode is then

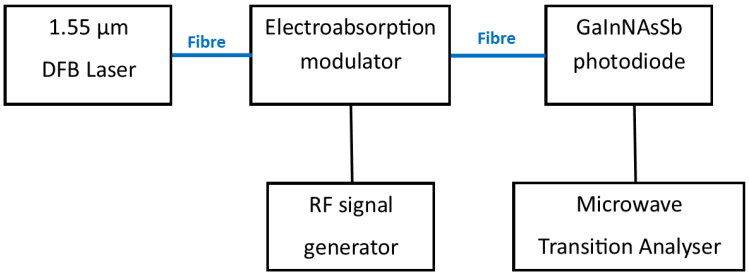

Figure 4.12: The experimental set up used in the bandwidth measurement based at Lancaster.

measured by a N5225A network analyser.

4.5 Gain

The gain of a photodiode is dependent on the position at which carriers are injected within the electric field. Pure injection of only holes or electrons is achieved by illuminating the device at a wavelength short enough to ensure the light is absorbed in the cladding only. In this study this was achieved with a 532.5 nm laser. At this wavelength, GaAs has an absorption coefficient of $5.7 \times 10^4\,\mathrm{cm}^{-1}$ [116]. In order to reach an intensity of 1%, 745 nm of GaAs cladding is required. GaInNAsSb cladding may also be used, but the absorption coefficient is unknown for this material at this wavelength, however it is likely going to be larger than that for GaAs.

Carriers of a single type will be allowed to diffuse to the electric field and be collected and create new electron-hole pairs by impact ionisation. This photocurrent was measured by chopping the laser and using a lock-in amplifier measuring the signal over a 1 kΩ resistor. The primary, unmultiplied photocurrent can be extrapolated with a linear fit [117], although some other studies predict a non-linear dependence [118]. In any case, the end result for multiplication is not substantially affected. An example is shown on figure 4.13.

The multiplication is simply the ratio of the measured photocurrent and the extrapolated primary photocurrent. The voltage on the x-axis of figure 4.13 is the bias placed over the photodiode in an equivalent circuit with a series resistance which includes the 1 kΩ resistor required for the lock-in amplifier and also the contact resistance of 82 Ω. This was done with equation 4.27.

$$V_{diode} = V_{applied} - I(R_{series} + R_{contact}) \tag{4.27}$$

The analysis used to measure the gain from mixed injection is the same, but no

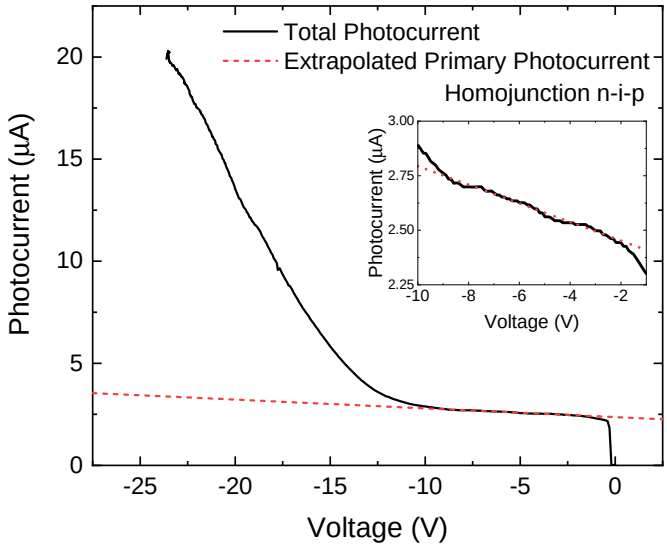

Figure 4.13: The fitting of the unmultiplied photocurrent as compared to that measured for C1-n3-785. The inset contains the same data but shows the unmultiplied current in greater detail.

lock-in amplifier was used and instead the photocurrent is measured by the subtraction of the dark current from the current when illuminated by a laser.

Chapter 5

Results: GaInNAsSb Optical Properties

This chapter will cover the optical properties of the GaInNAsSb dilute nitride alloy. This includes the absorption coefficient, band gap and Urbach energy of wafers before fabrication through FTIR transmission measurements. Quantum efficiency measurements on fabricated devices are presented both by use of a laser and also monochromated light from a filament lamp. The optimal annealing and device conditions are presented from a quantum efficiency perspective. Some discussion is present on the diffusion coefficients of GaInNAsSb.

5.1 Room temperature absorption coefficient

An example of the absorption coefficient measured at room temperature is shown in figure 5.1. On this figure it is compared to that of InGaAs and GaInNAsSb from another study with a slightly higher band gap [89]. The band gap of C4-n1-730 was found to be lower than that for InGaAs, therefore the absorption coefficient at some telecommunication bands is slightly higher. In particular, at 1.55 µm the GaInNAsSb has an absorption coefficient of 8400 cm^{-1} compared to 6500 cm^{-1} of InGaAs. In theory this would lead to a higher quantum efficiency in a GaInNAsSb photodiode, though in practice the difference is likely quite small. Furthermore, the GaInNAsSb absorption coefficient has a much shallower decline than InGaAs as the energy approaches the band gap energy. This is the Urbach tail and is further discussed in section 5.3.

In the previous GaInNAsSb study, the measured absorption coefficient was found from spectral quantum efficiency measurements using equation 2.19. As compared to

this study, the absorption coefficient is lower than expected. In order to compare the two, the absorption coefficient at a constant level above the band gap can be measured, $\mu(E_g{+}0.1\,\text{eV})$. For the two GaInNAsSb materials this results in a value of $9120\,\text{cm}^{-1}$ for this study and $3840\,\text{cm}^{-1}$ for the study by Tan et al. The differences in absorption coefficient are likely not due to fundamental differences in absorption properties. Instead the results gathered by Tan et al. are reliant on not only the accuracy of the depletion width measurement, but also are unclear on the effect of absorption outside of the depletion region. However, this would increase the photocurrent and therefore would lead to an overestimation of the absorption coefficient. Alternatively, it is possible that the GaInNAsSb detector performance is limited due to the poor collection of photo-generated carriers from within the depletion width. In section 5.6, the very low quantum efficiency found in unannealed devices is discussed despite the relatively thick intrinsic width and absorption coefficient. This contrasts with the absorption coefficient measurement where the collection of photogenerated carriers is not a factor. Therefore, I believe that the absorption coefficient measured in this study is more valid than that previously measured by Tan et al. The relation between absorption coefficient and quantum efficiency is discussed in greater detail in section 5.6.

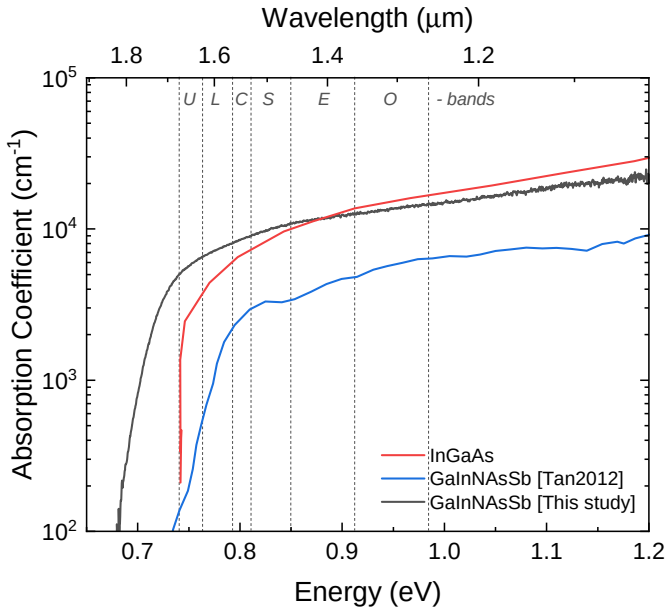

Figure 5.1: A comparison of the absorption coefficient of GaInNAsSb of this study (black) with that for InGaAs (red) [20] and GaInNAsSb from another study (blue) [89]. Also present on the figure are the telecommunication bands to show the range of absorption required. This particular GaInNAsSb wafer is sample C4-n1-730.

5.2 Band gap

The band gap of the GaInNAsSb layer is expected to be direct due to the large redshift of the Γ-valley due to the addition of the nitrogen. Therefore, the extrapolation of the linear section of μ^2 to the energy axis gives the band gap of the GaInNAsSb epilayer. This is shown on figure 5.2 with a range of samples from the same wafer annealed at various temperatures.

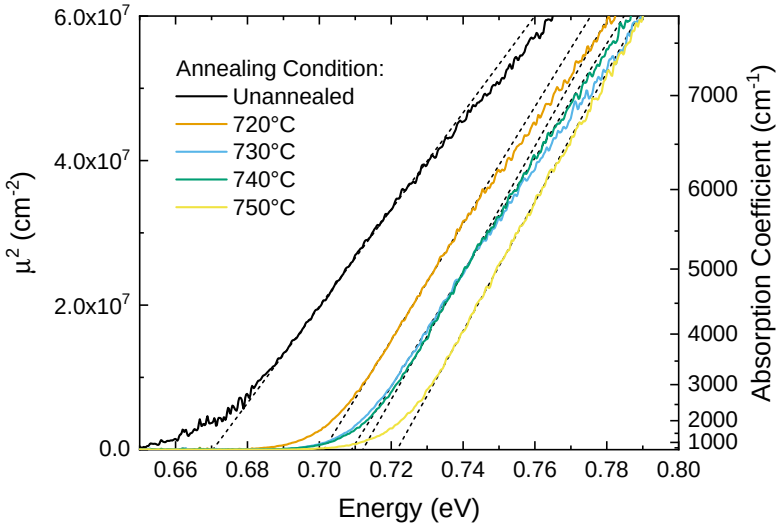

Figure 5.2: The extrapolation of the square of the absorption coefficient to the energy axis to find the band gap.

The linear fit to energies close to the band gap and the magnitude of the absorption coefficient (as compared to a material like Ge with an absorption coefficient of approximately $1 \times 10^3\,\mathrm{cm}^{-3}$ [14]) indicates that the band gap is direct. This method can result in accurate band gaps and is able to resolve band gap shifts of a few meV, although it relies on a low absorption coefficient baseline. For this study, the maximum allowable baseline was determined to be $\pm 200\,\mathrm{cm}^{-1}$. Improvements beyond this yielded very little enhancement of the uncertainty. In cases where a baseline was measured to be greater than $200\,\mathrm{cm}^{-1}$, repeating the background and then the sample measurement was sufficient to reduce the baseline error.

The first target of the band gap of GaInNAsSb was to reach a level capable of absorption at 1.55 µm, i.e. 0.8 eV. However, it is highly preferable to reach a lower band gap for the higher absorption coefficient. For comparison, InGaAs has a room temperature band gap of 0.74eV. So, it is a reasonable target to aim for an annealed band gap of 0.74 eV. This involves allowing for the blueshift of the band gap due to the annealing process applied to the GaInNAsSb. From figure 5.3, which shows the band

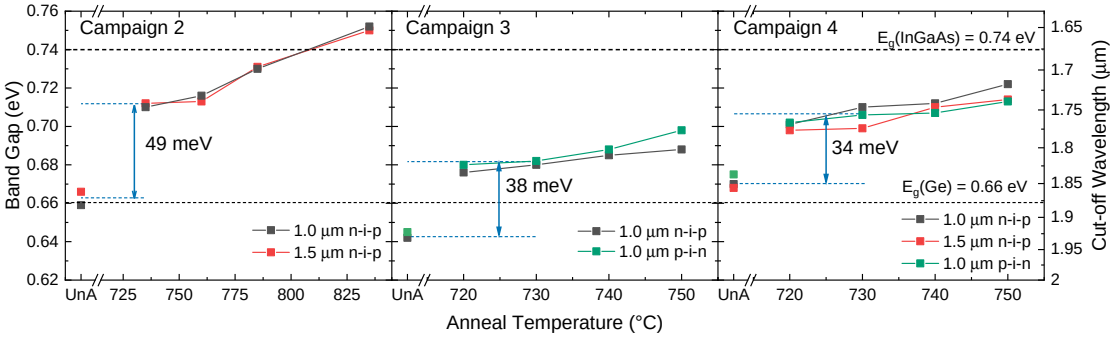

Figure 5.3: The dependence of the annealing temperature on the band gap for campaigns two, three and four. Blueshifts from the unannealed material to that annealed at 730 °C are indicated on the graph as well as the room temperature band gap of InGaAs and the indirect band gap of Ge.

gaps of both the unannealed and annealed samples of campaigns 2-4, the blueshift is approximately 40 meV after annealing at 730 °C. The differences in the blueshift are likely due to the exact composition of the GaInNAsSb layer, as previous studies into the blueshift have attributed the magnitude of the shift to the In content of the alloy [8] and the saturation of the blueshift has been attributed to the inclusion of antimony [65].

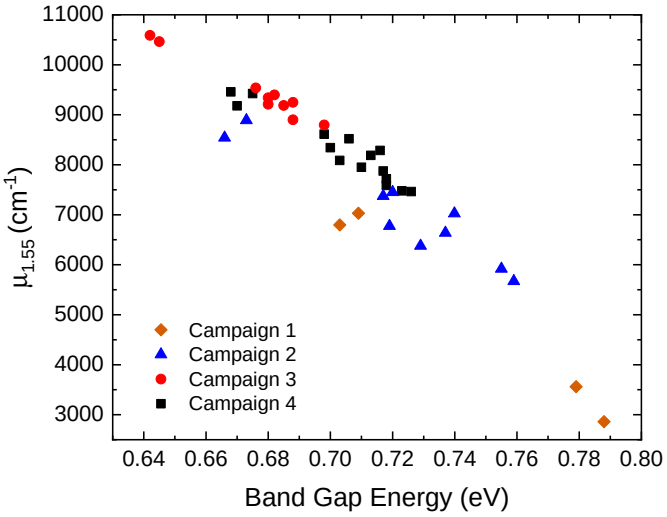

Figure 5.4: The dependence of the absorption coefficient at a wavelength of 1.55 µm against the measured band gap of the sample for a range of campaigns in this study.

Due to the flexibility of the dilute nitride alloy, a lower band gap could be reached by increasing the nitrogen content. A lower band gap would not only mean a longer cut-off wavelength but also a larger absorption coefficient at 1.55 µm as shown on figure 5.4. A larger absorption coefficient should lead to a larger quantum efficiency as given in section 2.2.4 by equation 2.19. However, a lower band gap usually leads to increased dark current and trap density through increased nitrogen incorporation therefore a balance

needs to be found between a large absorption coefficient and other important detector parameters.

5.3 Urbach energy

The Urbach energy was measured from the absorption coefficient data found from the samples in campaign 4. It was measured by fitting a straight line to the natural logarithm of the absorption coefficient at energies below the band gap as shown in figure 5.5a. The Urbach region of the unannealed sample on figure 5.5a coincides with water absorption (wavelength range of 1.8 µm to 1.95 µm) and therefore the signal is noisy. This can introduce some uncertainty with the linear fit, but it is clear that the Urbach energy will increase due to much shallower gradient compared to the annealed sample in black. Furthermore, it is extremely important that the baseline of the absorption coefficient is as close to zero as possible as, unlike with the band gap extrapolation, the absorption coefficients required for measuring the Urbach energy are quite low.

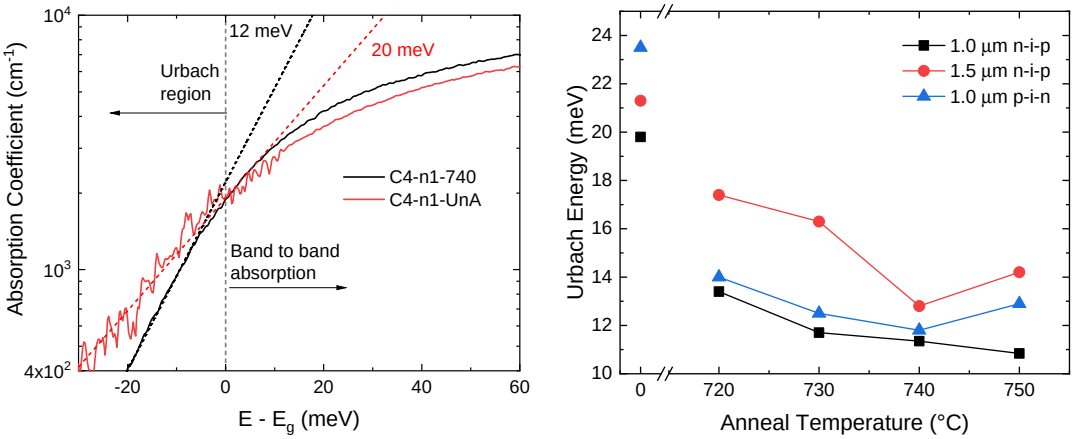

Figure 5.5: Figure (a) shows the presence of a non-zero absorption coefficient at energies lower than the band gap in the Urbach region. The characteristic Urbach energy is fitted for both samples. Noise from the unannealed line comes from water absorption at around 1.9 µm. Figure (b) shows the improvement of Urbach energy with annealing for samples grown in campaign four.

The results for Urbach energy as a function of anneal temperature in the wafers grown in campaign 4 are shown in figure 5.5b. From this figure there is a clear decrease in Urbach energy from the unannealed samples, which is more than 20 meV, to the annealed samples. The lowest of which reaches a minimum of 11 meV which is close to the typical III-V value of 10 meV. This reduction in Urbach energy is likely to be caused by an elimination in disorder-generating defects in the GaInNAsSb crystal structure with

annealing.

However, from the data in figure 5.5b, the Urbach energies for C4-p1-750 and C4-n1.5-750 are higher than the Urbach energy for the same wafer annealed at 740 °C. This may be caused by the thermal anneal introducing defects into the structure. This has been observed in literature which has been speculated as the formation of an arsenic-vacancy defect [119, 114].

In comparison to previous studies which have measured the Urbach energy of dilute nitrides, a value of 10 meV has been achieved in two separate studies. One by Tan et al. [120], where annealing at 800 °C brought the Urbach energy down from 16 meV for an unannealed sample to 10 meV. Another was achieved in unannealed material by Loke et al. [121] from responsivity data rather than absorption coefficient data. Both studies feature GaInNAs lattice matched to GaAs with a band gap of around 0.9 eV, higher than that for this study. Therefore, there are two reasons why 10 meV is achieved in those studies but not in this one. First, the increased nitrogen incorporation to reach a lower band gap will be generating more defects and therefore increasing the Urbach energy [122]. However, the Urbach energy was never quantified in this study, it is only by inspection that he Urbach energy appears to increase from a 0.2% to a 5.0% nitrogen incorporation. Secondly, it has been found that the Urbach energy of $InAs_xSb_{1-x}$ increases with the addition of Sb which is attributed to the disorder introduced by a new constituent in the alloy[123]. However, the Urbach energies of GaInNAsSb are much lower than that found in that study which are between 40 meV and 75 meV and so the effect of the additional constituent is extremely low if at all present.

In conclusion, the Urbach energy appears to be a useful parameter for discussing the improvement of lattice quality with annealing and does provide some evidence that excessive annealing can lead to the formation of defects. However, like with the photoluminescence intensity discussed in section 4.1, it is not enough to describe the performance of the material as a photodetector.

5.4 Temperature dependent transmission

The absorption coefficient over a range of temperatures between 77 K and 355 K is shown in figure 5.6a. The results were confirmed to be accurate by a comparing the absorption coefficient spectrum at room temperature in the cryostat (before and after cooling) to the absorption coefficient spectrum as measured by the magnetic sample holder. In the

"after cooling" measurement, the temperature controller of the cryostat was set to 295 K in order to make the comparison to room temperature.

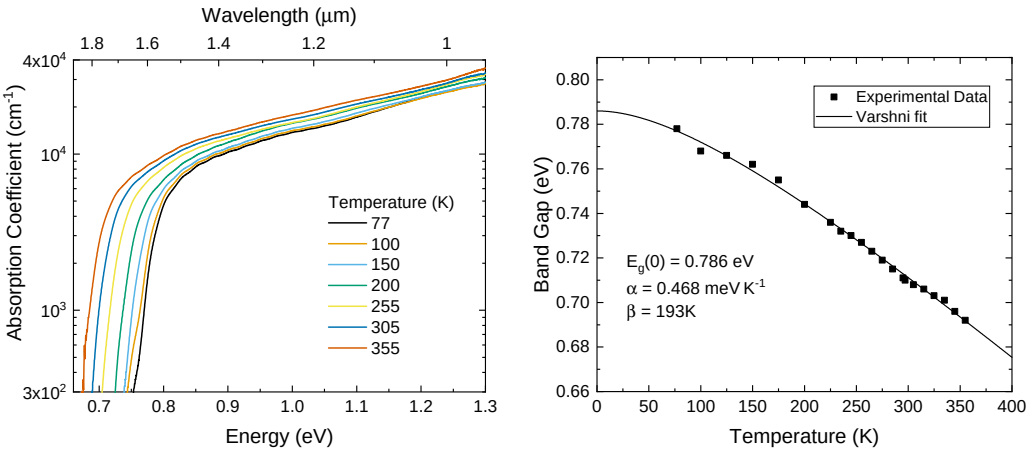

(a) **(b)**

Figure 5.6: The temperature dependence of the (a) absorption coefficient and the (b) band gap. The band gap data is fitted with the Varshni empirical equation with the parameters shown in the figure.

The temperature dependence of the band gap was measured and is shown in figure 5.6b. A Varshni fit is achieved with the parameters $E_g(0) = 0.786\,\text{eV}$, $\alpha = 0.468\,\text{meV K}^{-1}$ and $\beta = 193\,\text{K}$. A feature that is commonly seen in dilute nitrides, is an S-shaped temperature dependence of band gap found previously in a study by Mazzucato et al. [124]. This feature may not be found in this study due to the temperature limited to liquid nitrogen temperatures, though a similar effect was found in another study at temperature above 100 K [125]. Furthermore, the feature may only be present in photoluminescence measurements as both studies measured the band gap from the peak PL energy. Since transmission measurements do not rely on the recombination of carriers, the effects of localised states cannot interfere with the measurement.

In general, literature suggests that the temperature dependence of the band gap is weaker than that for GaAs which agrees with the results from this study as shown on figure 5.7. This figure also compares the temperature dependence of the band gap to InGaAs [126] and two other studies into dilute nitride compositions with zero temperature band gaps of 0.788eV (Nunna et al. [125]) and 1.154eV (Uesugi et al. [127]). Since the change in the band gap is dominated by the change in spacing between the atoms, it may be unsurprising that the Varshni fit of the GaInNAsSb layer is most similar to InGaAs rather the other dilute nitride samples due to the relatively large In content of the alloy.

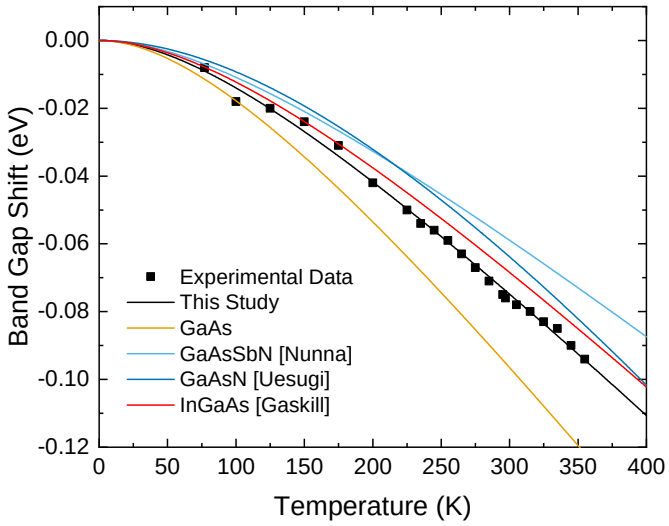

Figure 5.7: The Varshni parameters of this study compared to GaAs (Orange), InGaAs (red, [126]) to two other dilute nitride materials [125, 127].

Ideally, the temperature dependence would be weaker than that for InGaAs. A strong temperature dependence, typically decided by the magnitude of α, would lead to a large change in the absorption coefficient which leads to a difference in the quantum efficiency of the detector. For instance, between the typical range of operation temperatures of $-40\,°C$ and $60\,°C$, the absorption coefficient at $1.55\,\mu m$ changes from $8070\,cm^{-1}$ to $9450\,cm^{-1}$. For a $1\,\mu m$ layer, would change the internal quantum efficiency from 55% to 61%.

5.5 Quantum efficiency - laser

The voltage dependence of the photocurrent and quantum efficiency is given in figure 5.8a for a device illuminated by a $1.55\,\mu m$ laser operating with a power of $1\,mW$.

Figure 5.8a shows a suppression of the photocurrent between $0\,V$ and $-5\,V$ where the quantum efficiency reaches a maximum value of around 34%. This value is encouraging as the maximum EQE for this sample is 35%, as calculated from the absorption coefficient, GaInNAsSb width and reflection at the air-GaAs interface. The suppression of photocurrent at lower voltages is most likely caused by the heterojunction between the GaInNAsSb and the GaAs prohibiting photocurrent from flowing at lower biases. A similar trend is found in GaNAsSb/GaAs quantum well structures [73] which are likely to have a similar band structure. With a pure GaInNAsSb homojunction p-i-n device, the suppression is not found as shown on figure 5.8b. The size of the potential barrier was investigated using nextnano. Since GaInNAsSb is not in the database, the conduc-

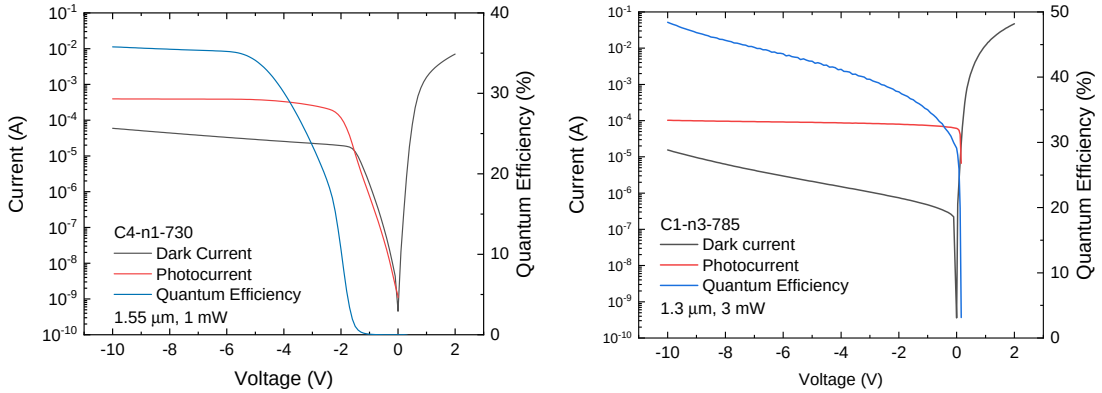

(a) **(b)**

Figure 5.8: The voltage dependence of dark current (black), photocurrent (red) and the external quantum efficiency (blue) for (a) a double heterojunction (C4-n1-730) and (b) a homojunction (C1-n3-785) device. The homojunction has a band gap of 0.8 eV and so is illuminated with a shorter wavelength of 1.3 µm.

tion band bowing parameter of InGaAs was changed to 3.1 in order to change the band gap of the material to 0.72 eV for the same concentration of In as measured by SIMS on wafers from campaign 1. This ensures that the effect of the nitrogen is only found in the conduction band and the effect of the In on the valence band is present. This does mean the effect of Sb is overlooked, however from SIMS, the Sb content was determined to be $< 1\%$ and therefore has very little effect on the band offsets.

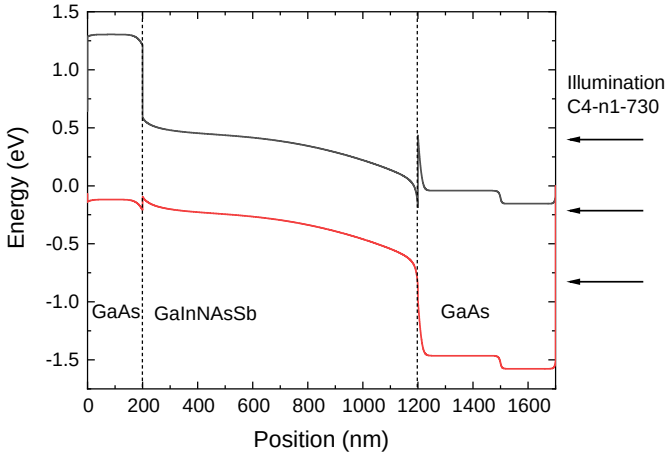

Figure 5.9: The band diagram of a double heterojunction n-i-p with zero bias. The intrinsic GaInNAsSb layer is modelled with a p-type doping of $1 \times 10^{15}\,\mathrm{cm}^{-3}$.

Figure 5.9 shows the modelled band structure with zero bias. Due to the large offset between the GaInNAsSb and GaAs, there is a large barrier in the conduction blocking the photogenerated electrons which nextnano predicts to be 0.53 eV. At sufficiently high

bias, the electrons have enough energy to either overcome the barrier or tunnel through.

5.5.1 Anneal dependence

The annealing process applied to the GaInNAsSb has a strong effect on the quantum efficiency. The device shown in figure 5.8a is selected from a range with a relatively high QE. In fact, a small change in anneal temperature has a large effect on the QE. This was verified by measuring the quantum efficiency on a device at each annealing temperature. The quantum efficiency was verified to be accurate from at least three separate measurements which gave quantum efficiency results within less than 5% of each other. From figures 5.10a and 5.10b, there is a clear peak in the quantum efficiency at 740 °C and 730 °C respectively.

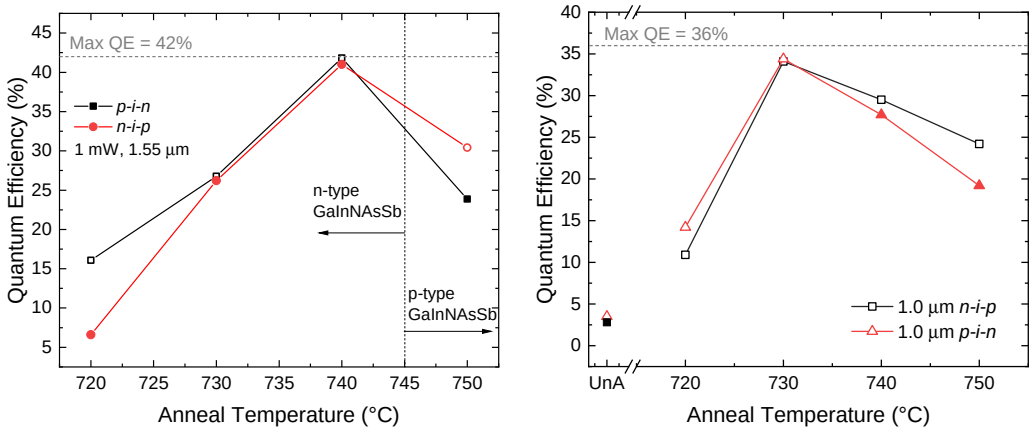

Figure 5.10: The dependence of the annealing on the measured external quantum efficiency at 1.55 µm for (a) the devices from campaign three and (b) the 1.0 µm thick devices from campaign four. Devices with a more optimal intrinsic type are shown with open symbols. The maximum quantum efficiency is indicated by a grey dashed line and is calculated from the average absorption coefficient of the annealed devices.

This would be partly due to the UID type of the GaInNAsSb. In both figures, when the GaInNAsSb is the most optimal type for quantum efficiency, the data point is indicated by an open symbol. The optimal type is decided by the location of the electrostatic junction so that it is preferential to have the junction at the top of the device where most of the absorption will occur. In the majority of cases the position of the junction determines whether the device can reach the maximum allowed QE (indicated by a grey dashed line) with the exception of C3-n1-740, which has a fully depleted intrinsic width. In this case, the position of the junction is irrelevant.

Outside of the most optimal cases, the unannealed devices and those annealed at 720 °C are underperforming, when considering their depletion and absorption coefficient. Figure 5.11 shows the difference in quantum efficiency between the measured value in figure 5.10 with that calculated from equation 2.22. With the exception of one device (C4-n1.5-UnA), those devices which are unannealed or annealed at 720 °C fall below expectations indicated by the grey dashed line on figure 5.11. This characteristic highlights a previous issue with the calculation of an absorption coefficient from quantum efficiency data in section 5.1. Above 720 °C, some devices still underperform, though this is attributed to a fully depleted intrinsic width and potential losses due to the power of the laser as discussed in section 5.5.2.

A measured QE greater than the modelled QE is caused by a contribution by the diffusion of carriers modelled by equations 2.20 and 2.21. The diffusion length and carrier lifetime required for this calculation are discussed in further detail in section 5.6. Furthermore, figure 5.11 shows the reduction in quantum efficiency found at higher temperatures in figure 5.10 is caused by a lack of depletion rather than any other material fault.

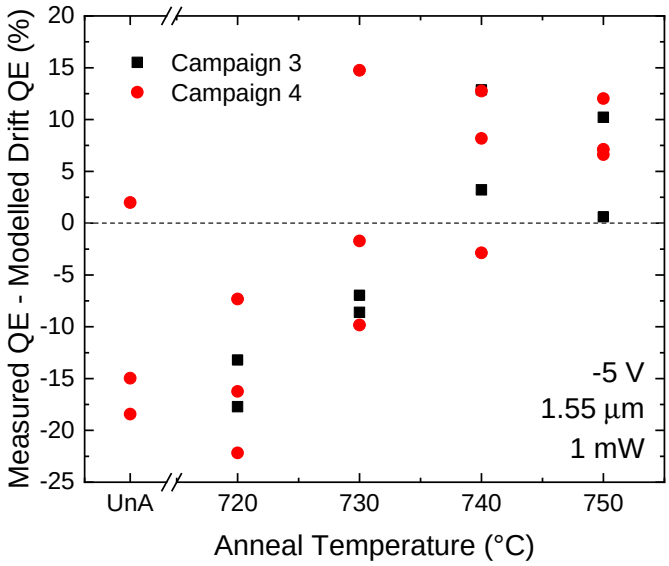

Figure 5.11: The difference in measured quantum efficiency and that calculated from the depletion width by equation 2.22 plotted against the annealing temperature. Lower temperature annealing conditions lead to a measured QE much lower than that which is predicted by considering the size and position of the depletion width.

5.5.2 Power dependence

The power dependence of the quantum efficiency can be measured by using various attenuators coupled directly the laser output. With this, a range of powers between a minimum of 10 µW, which is decided by the detection capabilities of the reference Ge photodiode, to a maximum of 20 mW, which is the maximum power from the laser. This range of powers is generated by two separate lasers. To confirm that the laser is not impacting the power dependence, a measurement at 1.4 mW is performed for both lasers. The quantum efficiency found at this power is 25.9% and 26.1%, for the lower and higher power laser respectively. This is within the acceptable limits of the accuracy for the measurement. The device used in this study is C4-n1-730 as is it one of the few samples that has a sufficiently low dark current so that the lowest power of lasers can be used and still detected.

Ideally, the QE should not change as the power is increased, however above a certain power the photocurrent generated may no longer follow a linear relationship with the power. This loss of linearity is important to note for future detectors and should be investigated. If the loss is device related, there are more optimal designs such as UTC photodetectors or waveguide structures which have large saturation powers. The loss of linearity may be caused by a series resistance limit where the photocurrent generated is too large and so the effective bias over the photodiode is reduced. It may also be caused by space-charge effects [128] which cause a screening of the applied electric field.

From figure 5.12, it appears that the saturation power of the photodiodes is around 1 mW. This result is unexpectedly low for a series resistance of 100 Ω, which is measured from dark IV measurements for a device with a diameter of 400 µm. The series resistance limit at −5 V with a responsivity of 0.4 A W^{-1} is given by several commercial photodiode data sheets to be:

$$P_{max} = \frac{V}{R_S \mathcal{R}} = \frac{5}{100 \times 0.4} = 100\,\text{mW} \tag{5.1}$$

Figure 5.12 shows the power dependence of the QE at −5 V only. However, by examining the voltage dependence of the QE at powers that have lost linearity (such as 4 mW), it is found that the QE can exceed the 20% predicted by figure 5.12b. On figure 5.13a, the 4 mW line reaches 38% before any significant avalanche multiplication occurs at lower powers, so the increase in QE is tied to the increased collection of photogenerated carriers rather than avalanche gain. The same feature is present in the 20 mW line but at a higher voltage of −12 V. The same comparison can be made with the low power

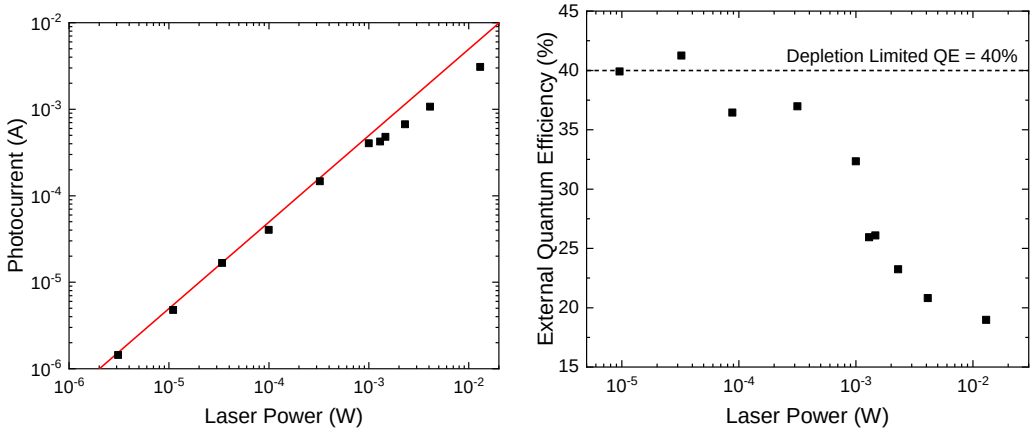

(a) **(b)**

Figure 5.12: The dependence of (a) photocurrent and (b) quantum efficiency on the power of the incoming optical signal generated by the C4-n1-730 with a reverse bias of 5 V. The red line on figure 5.12a represents a quantum efficiency of 40%.

measurements (0.01 and 0.1 mW) with that for 1 mW in figure 5.8a, but in the opposite direction. The low power measurements reach a peak QE value much earlier than that for 4 mW. Therefore, the voltage at which the QE saturates, referred to here as the saturation voltage, has a clear dependence on the laser power and is plotted on figure 5.13b.

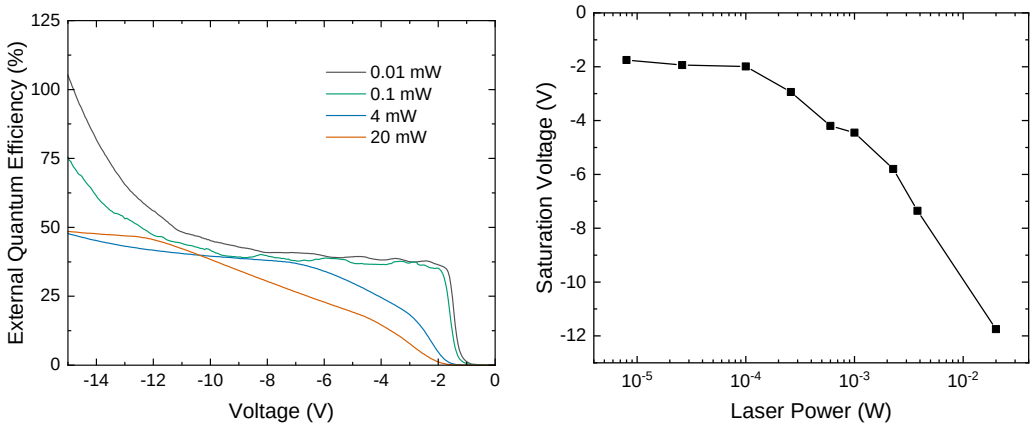

(a) **(b)**

Figure 5.13: (a) The voltage dependence on the quantum efficiency for a range of different incoming optical powers. (b) The dependence of the saturation voltage on the laser power. The saturation voltage is quantified as the voltage at which the full extraction of photocurrent is achieved in sample C4-n1-730.

The reasoning for this shift in voltage and corresponding drop in QE is very likely tied to the suppression of the electric field in the p-i-n by the addition of extra charge carriers.

Evidence for this comes from the earlier initiation of avalanche multiplication in the lower power measurements. For instance, by −15 V the lowest power measurement on figure 5.13a has reached past 100% due to impact ionisation, but as the input optical power is increased the quantum efficiency at −15 V, and therefore the avalanche multiplication, drops. Since impact ionisation is heavily dependent on the electric field the carriers are experiencing, we can deduce that the carriers themselves are counteracting the electric field due to the applied voltage.

Similar behaviour is found at other wavelengths. The quantum efficiency at 1310 nm was measured using a laser diode coupled into a multimode fibre. The power was altered by changing the source current for the laser diode and was measured using the same Ge photodiode that was used for the measurements at 1.55 µm. No attenuation was intentionally introduced, as the attenuators were for single mode fibres only, but a similar decrease in quantum efficiency is found at lower voltages that is not found at higher voltages.

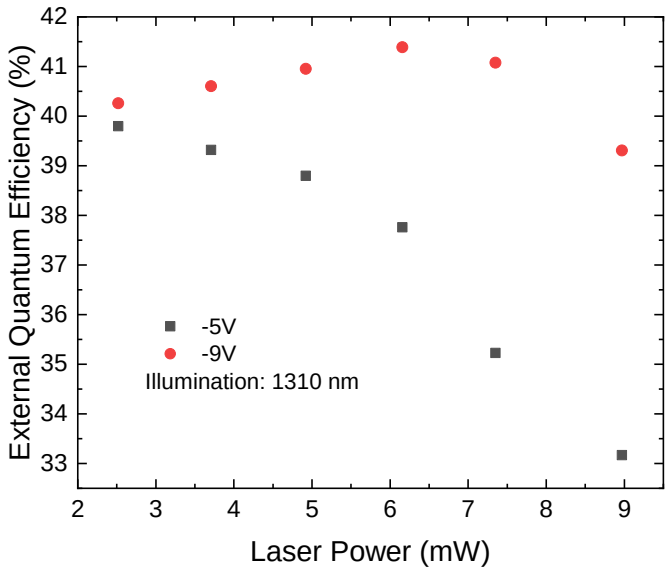

Figure 5.14: The power dependence of the photodiode at a wavelength of 1310nm. At the higher voltage of −9 V, the QE remains at 40% while it drops to 33% at −5 V.

In conclusion, the results show that introducing a different device geometry instead of a p-i-n could be advantageous for detection over a wide range of powers. However, the actual point of linearity loss may not be known exactly from this study. The power measurements rely heavily on the linearity of the Ge photodiode with no maximum power stated on the datasheet. Despite that, UTC photodiodes using GaInNAsSb and GaAs have been fabricated previously [24] which may cope with higher powers better as well as waveguide photodetectors which show linearity up to 8 mW, the maximum

power measured [91].

5.6 Quantum efficiency - spectral

Although the aim of the study was the design of photodetectors for 1.55 µm, they could also be used at other wavelengths. Therefore, the quantum efficiency as a function of wavelength for four difference devices were measured by the set-up described in section 4.3.3. The four devices chosen were C4-n1-UnA, C4-n1-730, C4-p1-730 and C4-p1-730. The n-i-p devices were chosen as a comparison of the least and most optimal annealing conditions, this is shown in figure 5.15a. The p-i-n devices were initially chosen for their different intrinsic types so that the diffusion characteristics of both electrons and holes can be measured. However, since the measurement, it was discovered that both samples have p-type intrinsic layers. This is shown in figure 5.15b. In order to check the validity of the results, the quantum efficiency is compared to the laser-based measurements with input optical power less than 1 mW to avoid any space charge screening effects.

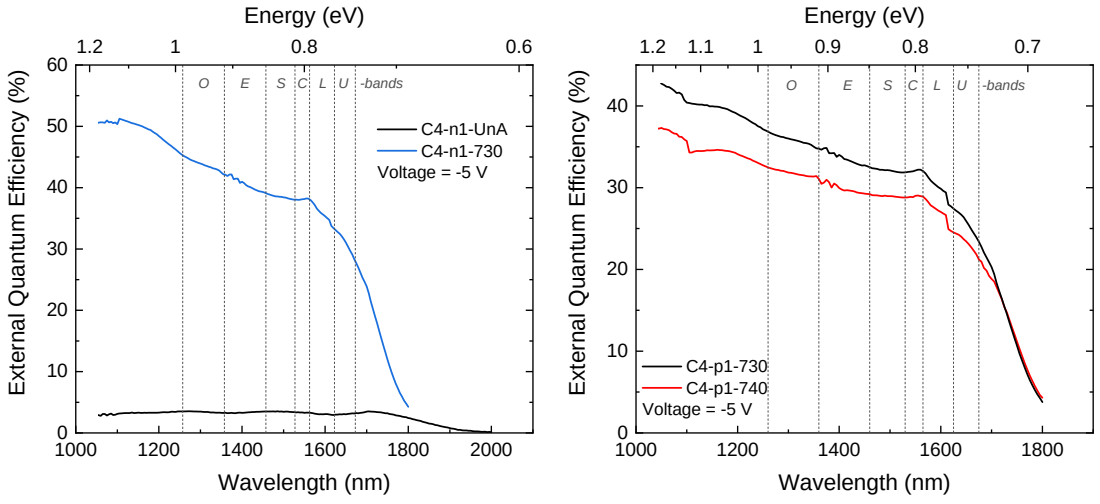

Figure 5.15: (a) The difference in the spectral quantum efficiency between C4-n1-UnA and C4-n1-730. (b) The difference in spectral quantum efficiency between C4-p1-730 and C4-p1-740. Telecommunication bands are shown to highlight the range of absorption at important applications.

Similar to the laser-based QE, the spectral QE of the unannealed device is still low at 3.3% at 1.55 µm compared to 38% in C4-n1-730. Since the power of the illuminating light is very low, the QE in these figures is considered to be the highest possible for that device at −5 V. Despite the low QE in C4-n1-UnA, it can be considered an achievement that detection up to 1.9 µm has been recorded in a GaInNAsSb device. Many studies

previously have not managed to extend the cut-off wavelength to this extent. This could even reach longer wavelengths using C3-n1-UnA or C3-p1-unA which have a smaller band gap.

In the p-i-n devices, the differences in quantum efficiency could be caused by two factors. First, the depletion width of C4-p1-730 is larger and therefore can collect more photo-generated carriers. Secondly, the diffusion coefficients may be affected by the annealing process. In any case, it is clear that C4-p1-740 is not collecting all photo-generated carriers as the absorption coefficient and band gap is similar to that of C4-p1-730 but the QE, especially at shorter wavelengths, does not match.

Modelling the quantum efficiency with absorption and diffusion coefficients

In homojunction devices, the short wavelength QE is limited by absorption in the top layer away from electric field. In double heterojunction devices, as used in this study, this can only occur when the electric field does not cover the entire intrinsic region. In such cases, it's possible for carriers to diffuse from undepleted regions into the electric field and contribute to the photocurrent. However, such parameters as the carrier lifetime and diffusion lengths are expected to be poor for GaInNAsSb due to the high defect density typically present.

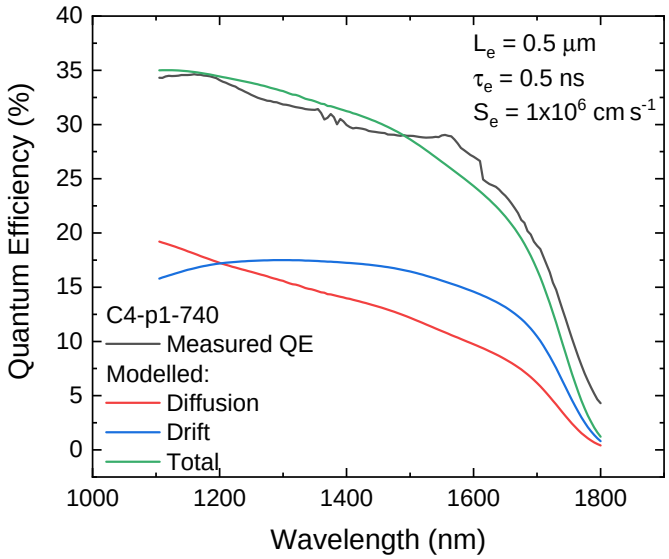

Figure 5.16: A comparison of the measured quantum efficiency (black) with the theoretically possible quantum efficiency (green) calculated using the contributions from drift (blue) and diffusion (red) for sample C4-p1-740.

In sample C4-p1-740, the theoretically predicted EQE is similar to that of the experimentally found EQE using the equations from section 2.2.4. Since the sample is a

p-i-n with a p-type intrinsic region, the junction is at the bottom of the device. In this case, absorption of short-wavelength light is away from the region with electric field and carriers rely on diffusion to reach the depletion region, furthermore only the diffusion length and carrier lifetime of the electron need to be specified. Using a measured value for depletion region from CV measurements, carrier lifetime of 0.5 ns [129], diffusion length of 5 µm [130] and a surface recombination velocity of 1×10^6 cm s^{-1}, equations 2.20 to 2.22 were used to calculate the theoretical QE and is plotted on figure 5.16.

This figure shows that the QE is well fitted with diffusion coefficients extracted from 1.0 eV GaInNAsSb material. This is encouraging as it is assumed that the increased concentration of nitrogen could further decrease the diffusion length and time. However, using the same coefficients for device C4-p1-730 results in a slight underestimation of the diffusion contribution to QE. Instead a diffusion length of 0.9 µm and a lifetime of 1 ns was used. The results of the calculation are shown in figure 5.17. This method cannot accurately find the carrier lifetime and diffusion length, however it does appear that there is a dependence of diffusion length and carrier lifetime on annealing temperature, and that annealing at high temperatures can possibly reduce the diffusion properties. This can be further investigated by measuring the quantum efficiency on C4-p1-750, another device with a p-type intrinsic region.

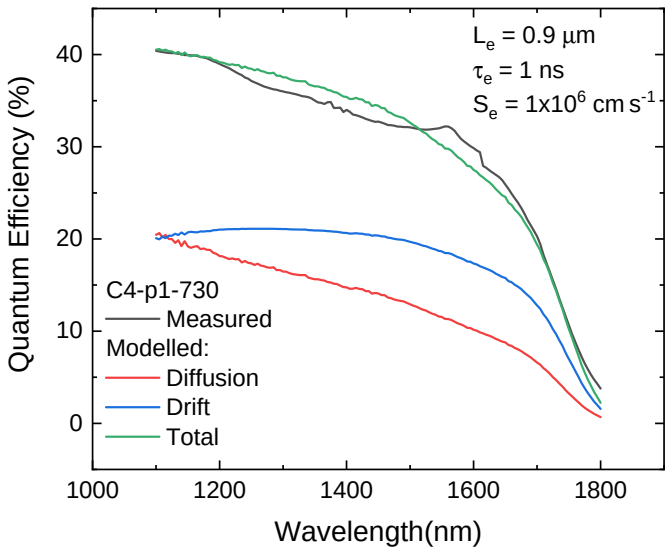

Figure 5.17: A comparison of the measured quantum efficiency (black) with the modelled quantum efficiency (green). The contribution due to diffusion was calculated with a diffusion length of 0.9 µm and lifetime of 1 ns.

However, there are two devices in which the modelled QE does not match the measured QE: C4-n1-UnA and C4-n1-735.

In the unannealed device, the depletion width is measured to be 540 nm. Despite the non-optimal position of the p-n junction, the drift contribution to QE at 1.55 µm should exceed 15%, instead it is around 3.3% as shown on figure 5.18a. This calculation assumes that the depletion width is solely within the GaInNAsSb layer, however this may not be true due to the large unintentional doping concentration. Simulating the electric field with the capacitance calculation detailed in section 4.4.3, a total of 350 nm of the electric field is positioned over the GaInNAsSb layer. However, this still has a calculated QE greater than what is measured and in order to match the QE, a depletion width of 100 nm is required with no contribution from diffusion current. This implies that the carrier lifetime is insufficient to even collect carriers that are generated within in the depletion region.

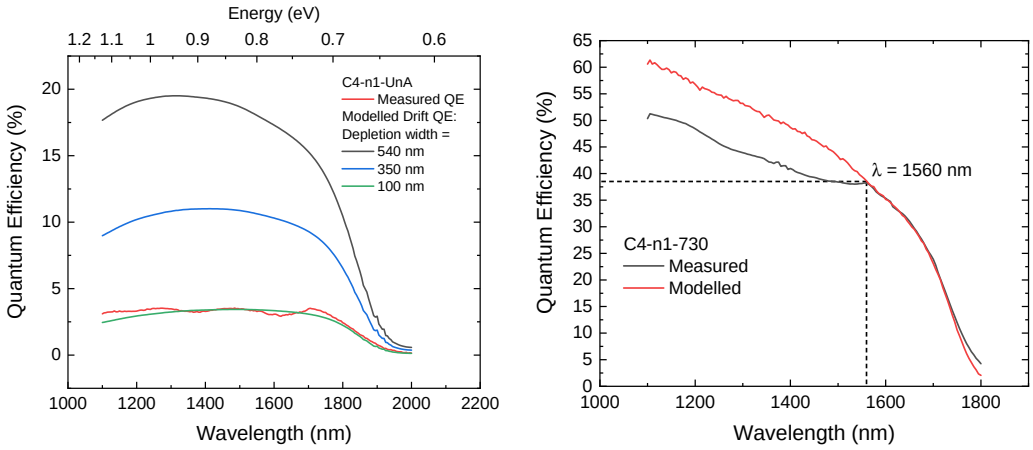

(a) **(b)**

Figure 5.18: The measured quantum efficiency against the calculated drift contribution to quantum efficiency for (a) a half depleted unannealed device (C4-n1-UnA) and (b) a fully depleted annealed device (C4-n1-730). In both cases, the applied voltage is −5.0 V.

The measured QE at short wavelengths on C4-n1-730 also does not match the prediction of the model as shown on figure 5.18b. In this case, the device is fully depleted due to the low unintentional doping concentrations. However, at wavelengths shorter than 1560 nm, the model and the measurement diverge. This is not caused by a power dependence as found in section 5.5.2 as the power from the lamp will be very low compared to the saturation power of the detector, 1 mW. Furthermore, the QE is independent of the method. Measuring the quantum efficiency by using a 1310 nm laser resulted in a quantum efficiency of 40%, similar to the result in figure 5.18b of 43%. Potential reasons for this include a suppression of the collection of carriers generated by the short wavelength light caused by a potential barrier at the heterojunction similar to that found

in InP/InGaAsP/InGaAs APDs [131]. Alternatively, the shorter wavelength light may not be coupling efficiently to the device and is not fully reaching the GaInNAsSb layer. This may be caused during processing by oxidising a layer or by leaving a thin film of photoresist. Regardless, the quantum efficiency is still large at shorter wavelengths and if shorter wavelengths are the intended application, then a wider band gap GaInNAsSb is recommended instead of C4-n1-730.

Chapter 6

Results: GaInNAsSb Electrical Properties

This chapter will cover the electrical properties of the fabricated GaInNAsSb photodiodes. First, the dark current for the homojunction photodiodes of campaign one and then for the double heterojunction devices. The effect of annealing temperature is discussed along with temperature dependent measurements that investigate the mechanism causing the dark current. The unintentional doping concentration and type is discussed along with the annealing conditions required to minimise the concentration. The type switch is further investigated by admittance spectroscopy on two devices from campaign three. Section 6.4 involves annealing samples using the facilities at Lancaster to further investigate the effect of the anneal on GaInNAsSb. Finally, the bandwidth is measured on the samples that have been found to be most suitable for the measurement: C4-n1-730 and C4-n1.5-740.

6.1 Dark current

6.1.1 Homojunction p-i-n - campaign one

The dark currents for the devices in campaign one are shown on figure 6.1. The measurements are conducted at room temperature for a device with a diameter of 400 µm. Across devices of diameters 100 to 800 µm, the dark current scaled with area indicating bulk-dominated currents rather than surface currents.

The annealed IVs also display very low dark current as compared to the unannealed devices as well as other devices in literature. The dark current density at -5 V for device C1-n3-785 is 2.2 mA cm^{-2}, which is an order of magnitude lower than that previously

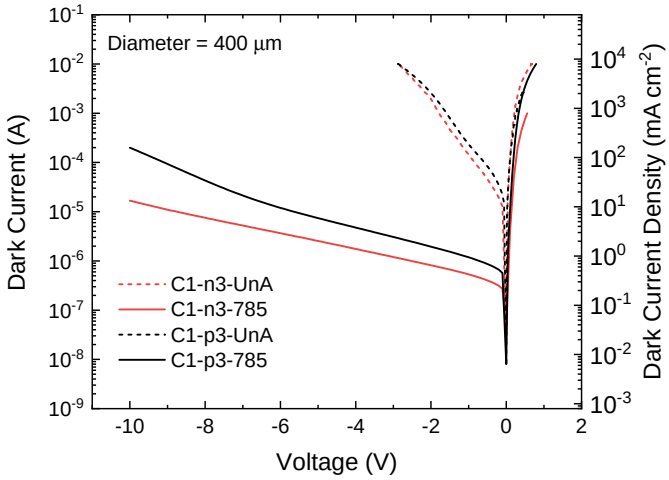

Figure 6.1: The current-voltage characteristics of the devices from campaign one. The solid lines indicate annealed devices and dashed lines indicate unannealed devices.

found in a similar band gap GaInNAsSb p-i-n [89].

Temperature dependent IV

The temperature dependent IV characteristics for device C1-p3-UnA are shown in figure 6.2. There is a weak temperature dependence, and as such the activation is as low as 0.1 eV as shown on figure 6.2b. This activation energy is not close to the band gap ($E_g(300\,\mathrm{K}) = 0.7\,\mathrm{eV}$) and this is likely due to trap assisted tunnelling, which is largely temperature independent and varies as the band gap increases with temperature. Surface current can be ruled out as the measured dark current is proportional to the area of the mesa.

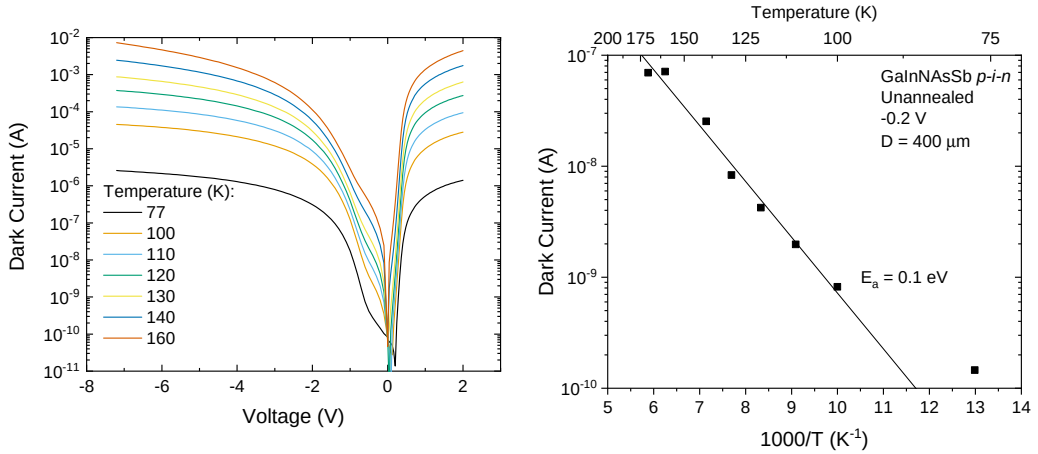

(a) .

(b)

Figure 6.2: (a) The temperature dependence of dark current in device C1-p3-UnA. (b) The Arrhenius plot of the dark current at a bias of −25 V with an activation energy of 0.1 eV.

On the other hand, the annealed sample has two regions with two separate gradients with activation energies of 0.22 eV and 0.64 eV at lower and higher temperatures respectively for an applied bias of −0.2 V. At temperatures lower than 125 K, the measured dark current is dominated by the noise floor of the SMU and so does not feature on the Arrhenius plot on figure 6.3b.

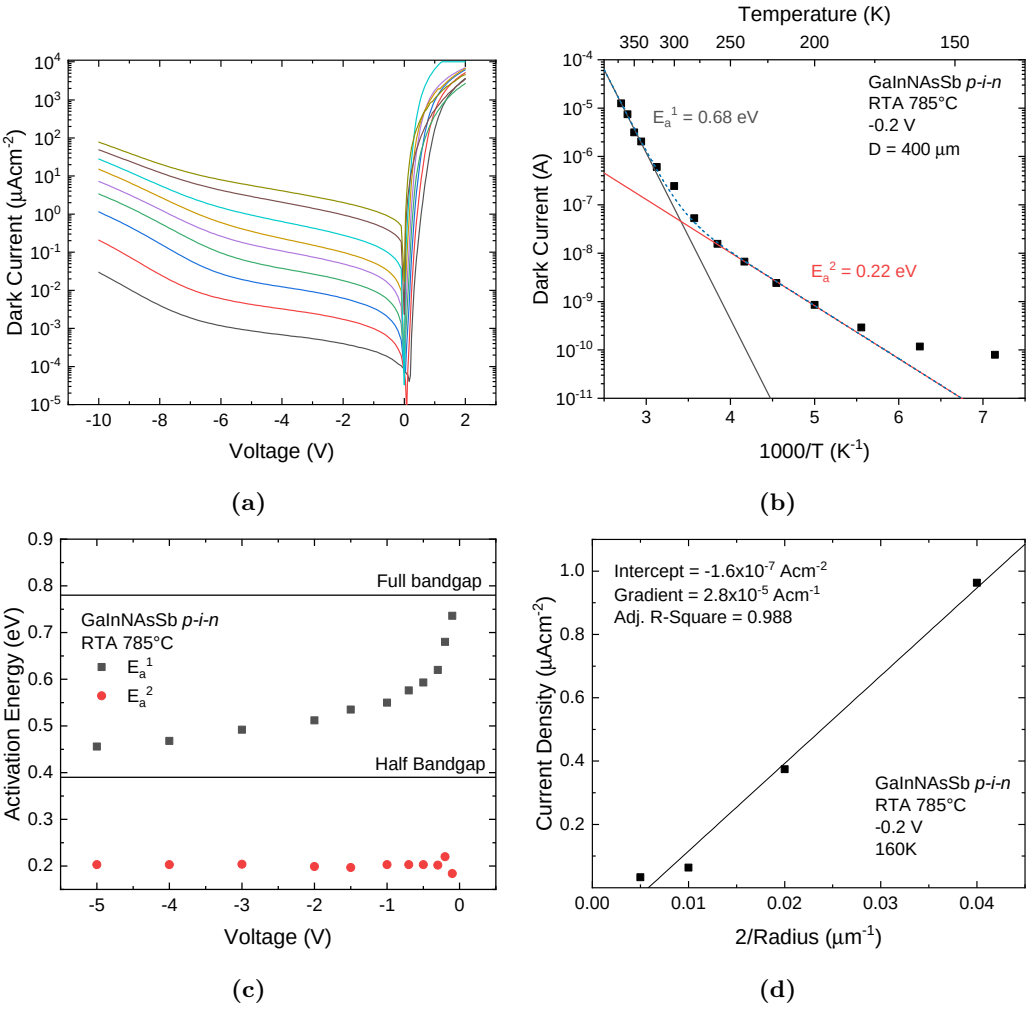

Figure 6.3: The temperature dependent properties of the dark current for an annealed homojunction p-i-n, C1-p3-785. (a) The dark current between 160 K and 360 K in intervals of 20 K. (b) The Arrhenius plot of the dark current at a applied bias of 0.2 V. (c) The voltage dependence of both activation energies. (d) The current density for C1-p3-785 at 160 K plotted against the size of the mesa to demonstrate the surface current present in the sample.

The voltage dependence of the activation energy is plotted on figure 6.3c. The high temperature activation energy decreases from around E_g to close to $E_g/2$ as applied voltage rises. This is believed to be caused by the transition of the dominant dark current mechanism from diffusion currents to SRH with increasing electric field as the activation energy tends towards the half band gap value of 0.39 eV.

The lower temperature activation energy appears to be voltage independent and could be caused by surface currents. Figure 6.3d shows the current density against $2/R$ for C1-p3-785 across devices with a range of mesa diameters 100 µm to 800 µm. The figure implies an appreciable surface current compared to the bulk dark current based on the difference non-zero gradient of figure 6.3d. Some materials exhibit surface currents after being etched by certain chemicals, such as the 1:8:80 sulphuric acid etch used in this study for InAs [132]. However, for these samples, the dark current due to this mechanism is negligible compared to the bulk dark current close to room temperature, which is the intended operating temperature. If, in future work, the surface generated dark current starts to dominate an etchant study should be done to find an optimal etch and a study into the chemical profile of the surface of the photodiode such as Auger electron spectroscopy.

6.1.2 Double heterojunction devices

Campaign two was the first campaign in this study to investigate a range of annealing temperatures. The dark current density as measured on 400 µm diameter device at −5 V is shown on figure 6.4.

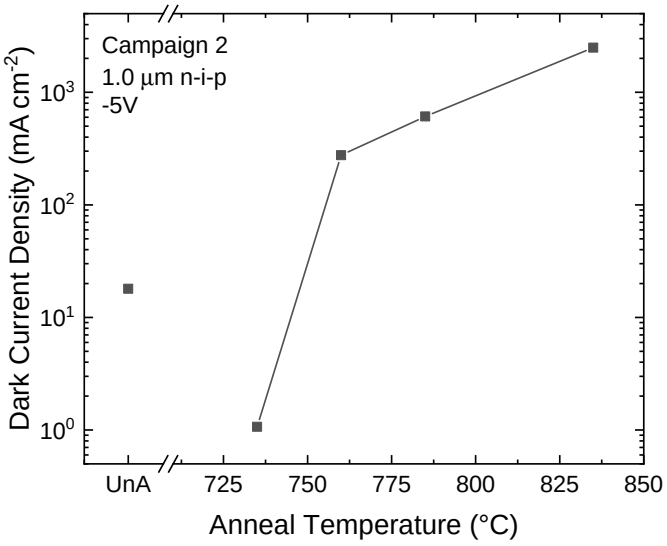

Figure 6.4: The dark current density at −5 V plotted against the annealing temperature for devices in campaign two.

The only annealing condition that indicated improvements to the dark current was at a temperature of 735 °C. The change in optimal annealing temperature from campaign one is most likely caused by the difference in composition of the GaInNAsSb alloy as a lower band gap was the target of the campaign. The band gap of the samples in campaign

two is lower than that for campaign one indicating a greater N or In composition. The next two campaigns, three and four, have annealing temperatures centred around 735 °C. The dark current density at −5 V for all processed devices from campaigns 3 and 4 is shown in figure 6.5.

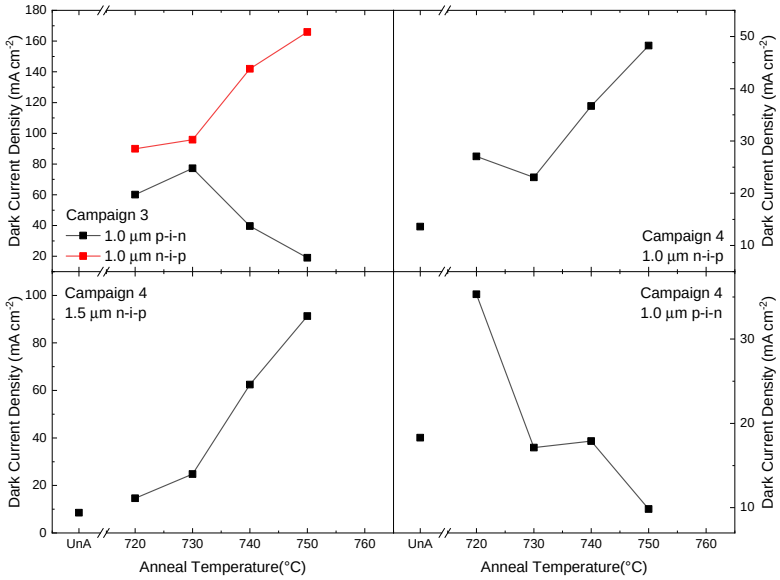

Figure 6.5: The dark current density for all processed devices from campaigns three and four. The measurement is taken at −5 V on a device with diameter 400 µm.

In campaigns three and four, the dark current is not always reduced from the as-grown device by annealing. However, there are many other parameters beyond the magnitude of the dark current that require consideration. For instance, SRH generated dark current is proportional to the depletion width and so the unannealed devices may have a reduced dark current due to the small depletion width. Furthermore, figure 6.5 does not account for the voltage dependence of dark current. For example, C4-p1-UnA and C4-p1-730 have similar dark currents at −5 V. However, with further bias the dark current in the unannealed sample rapidly increases.

In comparison to previous research, the dark current density of these samples is highly encouraging. Considering the more optimal anneals, for example C4-n1-730 has a dark current density of 23 mA cm^{-2} which is comparable to the results found by Tan et al. [89] but for a smaller band gap of 0.71 eV. Furthermore, the value extracted by Tan et al. is at an electric field similar to what would be present in the intrinsic width of C4-n1-730 with an applied bias of −5 V. This is significant evidence that the material quality of some GaInNAsSb devices in this study is high compared to previous studies.

Temperature dependent IV

The dark current as a function of temperature is shown in figure 6.6a for device C4-n1-730, a double heterojunction n-i-p. In comparison to the homojunction device, the dark current between −1 V and 0 V appears to be suppressed. This could be caused by a potential barrier introduced by the GaInNAsSb/GaAs interface as the suppression appears in all the heterojunction devices. Such a sharp change is not seen in the homojunction devices. Furthermore, the position of the "knee" in the IV characteristic appears to be temperature dependent, increasing from −0.85 V at 175 K to −1.5 V at 340 K. This feature is previously attributed to the presence of a barrier caused by the band offset in GaInNAsSb/GaAs, it is surprising to find the "knee voltage" increases at higher temperatures. From the Varshni parameters found in section 5.4, the temperature dependence of the band gap in GaAs is stronger than that for GaInNAsSb. Therefore, since the alignment of the heterojunction is type-I, i.e. the GaInNAsSb is fully contained by the GaAs, it is expected that the band offset would increase at lower temperatures. Therefore, it could be expected that the "knee voltage" would increase. The position of the "knee voltage" is important as it is the minimum voltage at which the detector can operate and not suppress the collection of carriers from the intrinsic region. It is plotted as a function of temperature in figure 6.6c.

At a low bias of −0.1 V, the high temperature activation energy is found to be 0.68 eV. The proximity of this value to the band gap implies that the dark current at higher temperatures is diffusion limited, as for the homojunction device.

There also appears to be a region between 200 and 240 K which shows an activation energy of 0.16 eV. Like in the homojunction samples, this activation energy is too low to correspond to $E_g/2$ and so could imply the presence of surface currents. In similar fashion to the homojunction device, the dark current at 220 K was investigated across device diameters of 50 µm to 400 µm. At −0.1 V, a surface current density of 9.2×10^{-7} A cm^{-1} was found compared to effectively zero bulk current density. This shows that the surface current dominates for this temperature and bias condition, although it has in fact reduced from the homojunction samples. This is likely due to the heterointerface affecting the path of the surface current and therefore increasing the shunt resistance.

As the voltage applied to the device increases, the activation energy decreases as expected and the smaller activation energy is no longer visible as the bulk dark current dominates. Similarly to the homojunction device, the activation energy decreases from the full band gap value towards the half band gap value by −5 V which indicates the

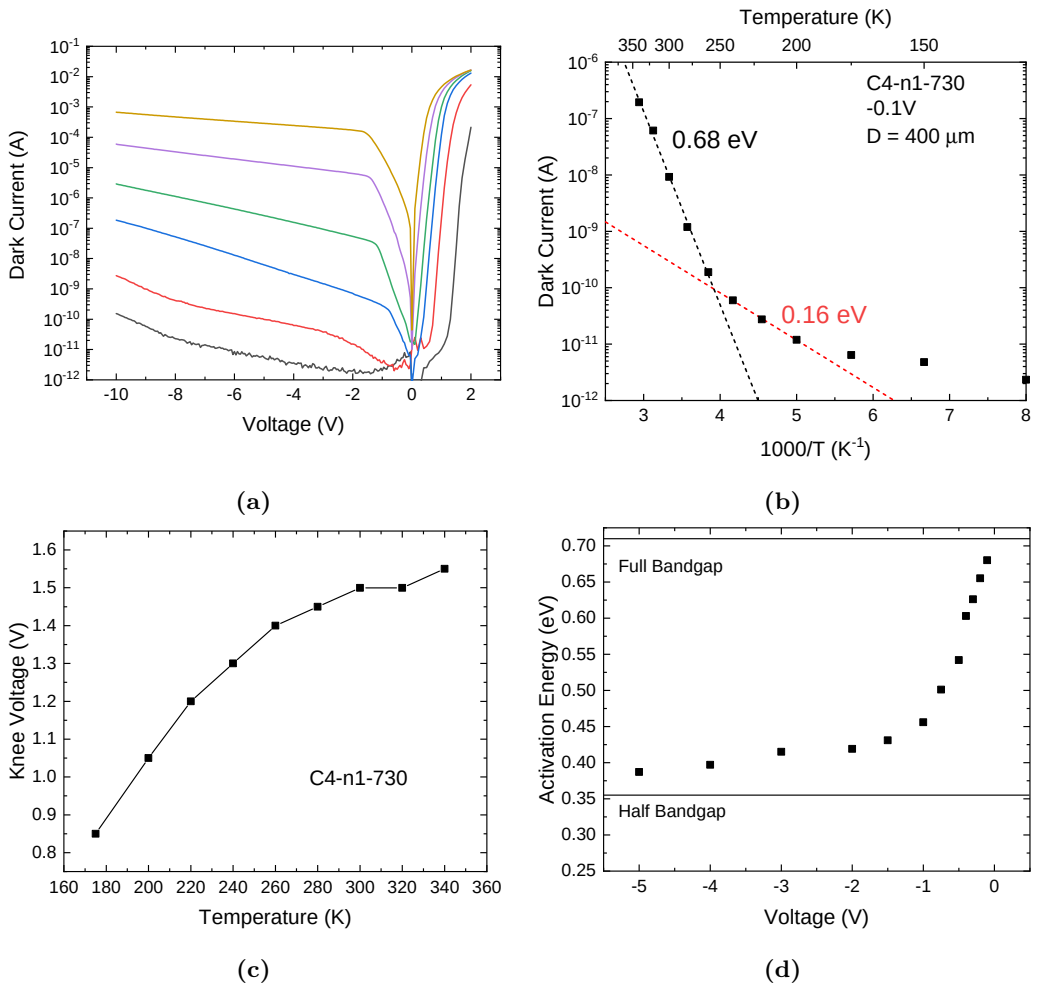

Figure 6.6: The temperature dependence of the dark current for sample C4-n1-730. (a) The dark current from 77 K to 360 K in steps of between 50 K and 60 K. (b) The Arrhenius plot of the dark current at a bias of −0.1 V. (c) The knee voltage of the dark current as a function of applied bias. (d) The voltage dependence of the high temperature activation energy.

increase of SRH dominated dark current.

The largest difference between the homojunction and double heterojunction appears in the unannealed sample which shows a much larger activation energy of 0.57 eV, close to the band gap of 0.67 eV as shown on figure 6.7b. The disparity between the two samples could be caused by multiple issues. First, the simplest explanation is a difference in composition and growth conditions. The two samples were grown at different times under different conditions, and, although it is typically expected that the lower band gap device has the increased nitrogen incorporation and hence larger concentration of defects it is possible that it is not the case. Alternatively, the other difference between the samples is the structure. However, the double heterojunction reduces the dark current by reducing the diffusion current from the cladding layers. Since the activation energy

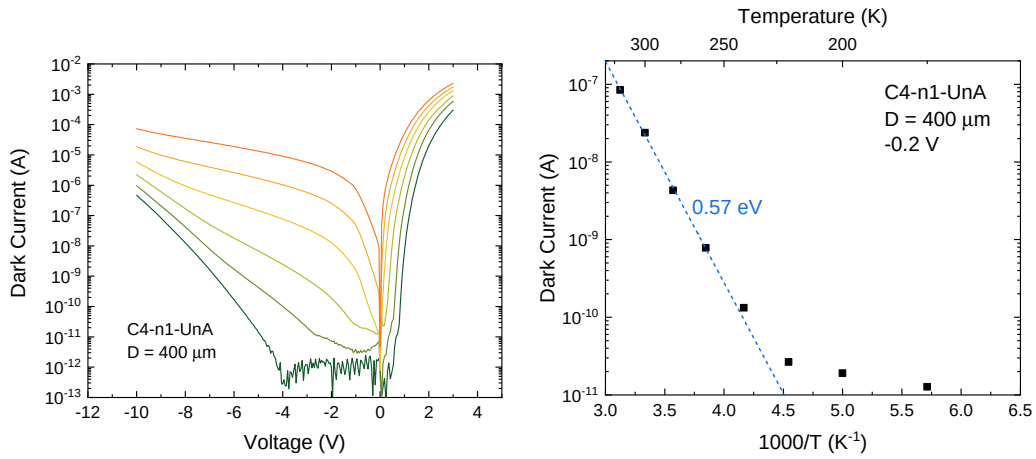

(a) **(b)**

Figure 6.7: (a) The temperature dependence of the dark current for device C4-n1-UnA and (b) the Arrhenius plot at a bias of −0.2 V.

of C1-p3-UnA is so low, the largest difference is likely due to a significant difference the formation of defects in comparison to C4-n1-UnA.

6.2 Doping density and type

The unintentional doping (UID) concentration of the dilute nitride materials is an important parameter as the magnitude of the UID affects the width of the electric field in the sample as described previously in section 2.2. Therefore, it would be highly preferable to keep this concentration as low as possible. The UID concentration required in order to deplete a certain thickness is discussed previously in section 2.2.4. In order to fully deplete 1.0 µm with a bias of −5 V, a maximum concentration of $1.5 \times 10^{16}\,\mathrm{cm}^{-3}$ is required, which is non-trivial. Some previous studies have resulted in concentrations as $3 \times 10^{17}\,\mathrm{cm}^{-3}$ [94], $7 \times 10^{16}\,\mathrm{cm}^{-3}$ [92] and $1.1 \times 10^{17}\,\mathrm{cm}^{-3}$ [133]. Furthermore, since the intrinsic type is known to change with annealing processes it is important to track both the type and the concentration with annealing temperature.

From the wide annealing conditions of campaigns one and two, the unintentional doping concentration improves for certain annealing conditions as compared to the as-grown device. This is shown on figure 6.8. Furthermore, the intrinsic type switches after the post-growth anneal from n-type to p-type in all cases except for device C2-n1-735 which remains n-type.

The annealing conditions resulting in the lowest unintentional doping also changed from campaign one to two. Both annealed samples in campaign one show a decrease

in unintentional doping whereas annealing at the same temperature in campaign two increased the UID level as compared to the unannealed sample. This is caused by variations in the composition and growth conditions of the alloy and means that optimised annealing conditions cannot be applied broadly across the GaInNAsSb alloy range but differ for specific band gaps and compositions.

Since the unintentional doping concentration appears to rise with annealing temperature once the UID has switched to p-type, the next devices studied focused on a smaller range closer to the intrinsic type switch occurring between 735 °C and 760 °C.

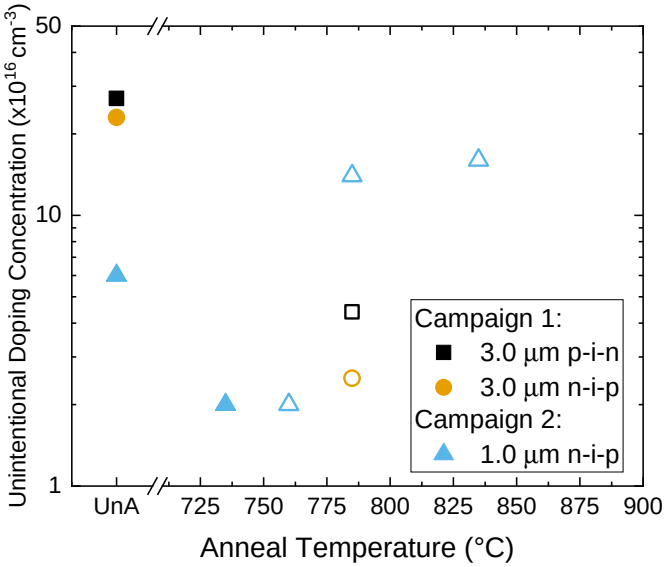

Figure 6.8: The unintentional doping concentrations for devices from campaigns 1 and 2 against annealing temperature. The type change occurs in devices that are annealed at temperatures greater than 735 °C and samples that have changed intrinsic type to p-type are indicated by open symbols.

The results for the range of annealing temperatures of campaign three and four are shown in figure 6.9. First of all, this test could not identify the background type of C4-p1-720. The reverse bias IV does not match that of the fully etched device, indicating that it is p-type, however there is a strong area dependence of dark current with a forward bias, indicating the p-n junction has been etched and an n-type intrinsic layer. In this study, it is assumed that the GaInNAsSb layer is n-type as the depletion width could be extending past the etched width due to the low unintentional doping concentration of the layer. Similar uncertainty was found in C4-p1-730, but the spectral quantum efficiency measurement indicated that the layer was p-type. This reasoning could be applied to the device to verify the type of C4-p1-720, however the QE of this sample is lower than that expected by the drift contribution (figure 5.11). Therefore, it may be unclear if the

QE at shorter wavelengths is predominantly affected by the junction or by poor carrier collection issues.

The results do have some similarities compared to the results of campaigns one and two. For instance, the unintentional doping consistently starts with a high n-type concentration and switches to p-type with annealing. Furthermore, the 750 °C annealing temperature consistently gives the highest UID concentration of all annealing conditions. In general, the lowest concentration is around $1 \times 10^{16}\,\mathrm{cm}^{-3}$, except for C4-n1-730 which is as low as $1 \times 10^{15}\,\mathrm{cm}^{-3}$. This result compares very favourably with some results from the literature, for example, $6.3 \times 10^{15}\,\mathrm{cm}^{-3}$ [134] and $2.7 \times 10^{15}\,\mathrm{cm}^{-3}$ [81]. However, both examples are GaInNAsSb with a band gap of around 1 eV for solar cell applications. The reduced nitrogen content in these alloys will reduce the amount of nitrogen related defects and subsequent unintentional doping through these defects, hence the results from this study are very encouraging.

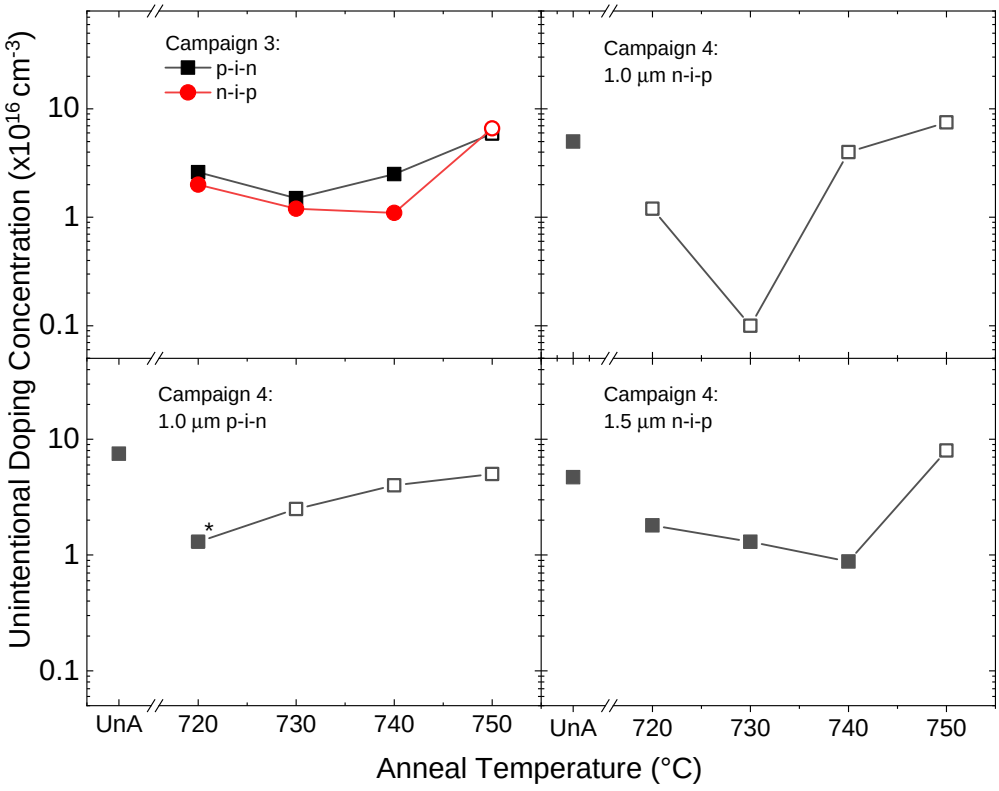

Figure 6.9: The annealing temperature dependence of the unintentional doping concentrations of the devices from campaigns three and four. GaInNAsSb layers with n-type conductivity are denoted with solid symbols, while those with p-type are open symbols. The star indicates uncertainty in the type of sample C4-p1-720.

However, the temperature at which the type switch occurs is no longer consistently between 735 °C and 760 °C. This difference could be caused by inconsistencies between

growth runs of campaign four. For instance, the growth temperature [82] and the V-III ratio [83] appear to affect the resulting type of the GaInNAsSb layer.

The overall unintentional doping concentration as measured by capacitance-voltage is the difference between the acceptor and donor concentration, as given in equation 6.1. Therefore, we cannot directly measure the dynamics of the defect concentration with annealing temperature.

$$N_{eff} = |N_A - N_D| \tag{6.1}$$

However, in combination with the dark current, we can make some assumptions regarding the relative levels of defects resulting from the different annealing conditions. For instance, in figure 6.10, the dark current density at $-5\,\mathrm{V}$ is plotted against the unintentional doping for all devices fabricated in campaign four. The lower annealing conditions all fall within region *i* while the unannealed case and 750 °C annealed case all fall in the outer region *iii*. Therefore, we can assume that the lower temperature annealing conditions have minimised the defects that contribute to dark current through acting as recombination centres.

It requires a method such as DLTS or admittance spectroscopy to thoroughly explain the annealing trends of the defect concentrations. Section 6.3 will apply admittance spectroscopy to two devices from campaign 3 to check the concentrations of the defects.

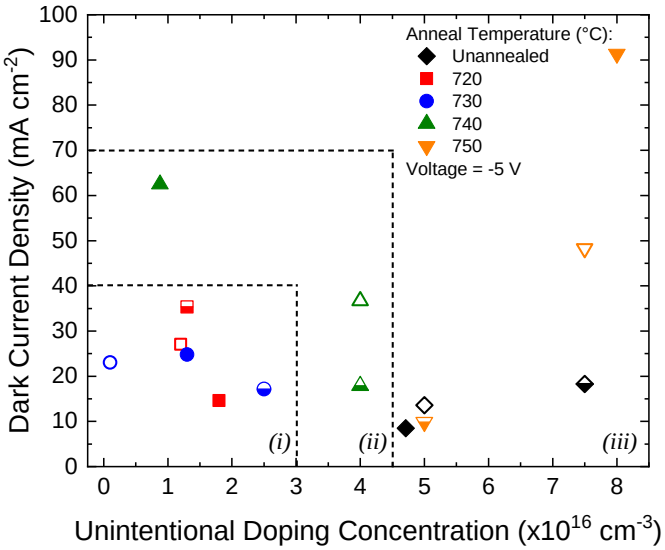

Figure 6.10: The unintentional doping concentration and the dark current for all devices from campaign four. The region marked *(i)* marks the more preferable combination of UID concentration and dark current compared to *(ii)* and *(iii)*. The open symbols represent the 1.0 µm n-i-p, half-filled symbols represent the 1.0 µm p-i-n and the closed symbols represent the 1.5 µm n-i-p.

6.3 Admittance spectroscopy

The aim of applying admittance spectroscopy (AS) to the GaInNAsSb photodiodes is to track the concentration of various defects across annealing temperatures to shed light on the intrinsic type switch from n-type to p-type. If we can find defects that lie in the same place in the band, we can try to simplify the analysis from the previous section. The technique was applied to two p-i-n devices from campaign three. In one case, the intrinsic GaInNAsSb region remained n-type with an anneal of 730 °C, and in another case it had switched to p-type after an anneal of 750 °C. The capacitance and conductance were measured across a range of frequencies, temperatures and bias conditions. Zero bias was measured along with four other reverse bias conditions for comparison. The frequencies chosen had an upper limit of 1 MHz imposed by the LCR meter and typically the lower bound was around 1 kHz, which is the lowest frequency for a reliable measurement. The minimum temperature achievable was 77 K and, to maintain accuracy in the Gaussian fit, the temperature was increased in intervals of 5 K.

The first step of AS is to find the temperature at which the conductance peaks for different measurement frequencies. This was achieved using a Gaussian fit over a select range of temperatures. For example, figure 6.11a shows two peaks in the conductance for a frequency of 10 kHz which indicates there are two trap levels that can be probed by this temperature range and frequency. Some uncertainty in the peak temperature is introduced with the varying baseline of the conductance and the convolution with other peaks. For instance, traps 3 and 4 occur at very similar frequencies and temperatures (approximately 100 kHz and 170 K). However, at the extremes of the frequency range each trap can clearly be distinguished.

In most cases the peak is clearly defined, and the small increments of temperature used in this study will limit the uncertainty of the peak temperature to a maximum of 5 K. With this data, Arrhenius plots can be used to measure the activation energies and pre-exponential factors from the gradient and intercept of the fitted line respectively. Each pre-exponential factor is then used to calculate the energy axis of the defect density plot using equation 4.25.

From figure 6.11, there are a total of 5 defects found: two in the n-type material and three in the p-type material. The position of the defect within the band gap is determined from the activation energy and the intrinsic type of the material. For instance, trap 1 on figure 6.11c is 0.18 eV from the conduction band as it is in n-type material. The defects on figure 6.11d are for p-type GaInNAsSb and therefore refer to the valence band edge.

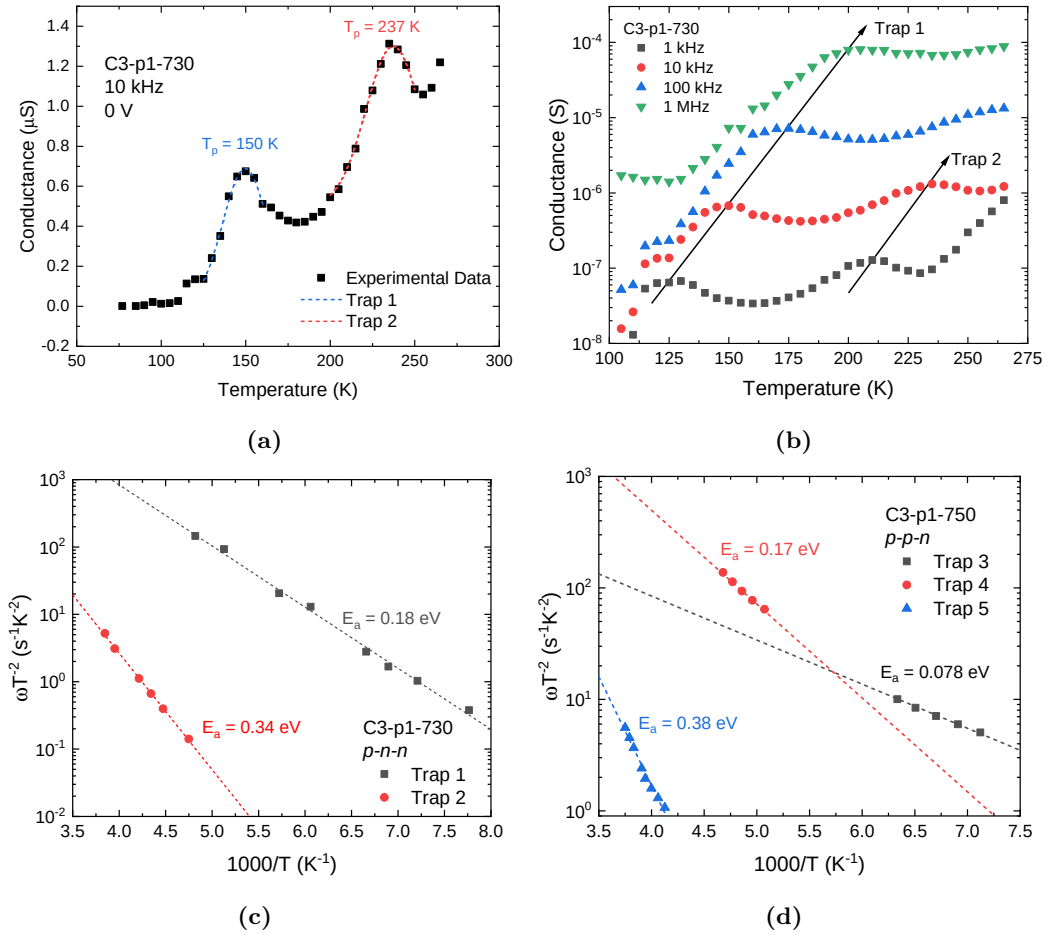

Figure 6.11: The admittance spectroscopy of C3-p1-730 and C3-p1-750 including the Gaussian fits required to find the peak temperature at (a) 10 kHz and (b) a range of frequencies for the Arrhenius plots. Also featured are the Arrhenius plots which give the activation energy and the pre-exponential factor required for the defect density distribution of samples (c) C3-p1-730 and (d) C3-p1-750.

Using the knowledge of the trap position, we can conclude that T2 and T5 are the same defect since they coincide within the range of uncertainty in the activation energy. Unfortunately, in order to measure larger activation energies, such as for T3 or T4 on C4-p1-730, it appears that either a very high temperature or a very low frequency is required which is not be possible with the current set up. It is also possible to intentionally dope the semiconductor so that the p-type defects are observable before the type switch or n-type defects after the type switch [115]. However, this is not an ideal practise as this will introduce levels that would normally not appear in the dilute nitride alloy. Some information of the annealing dependence of the defects can still be inferred from the limited defect density information that AS can supply. For instance, we can propose and upper bound on the concentrations of T3 and T4 by knowing that C3-p1-730 has

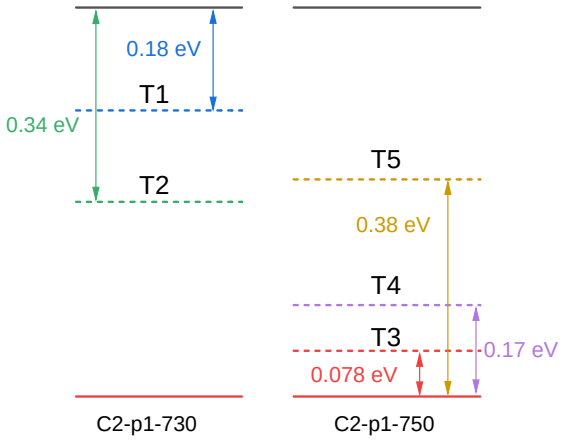

Figure 6.12: The energy levels for each sample. T2 and T5 are very close to each other which indicates they could represent the same defect level.

an overall n-type concentration and the defect concentration of T1.

The defect densities were calculated from the area underneath a Gaussian fit of equation 4.26 using the capacitance measured at various frequencies and temperatures. The built-in voltage was estimated from the amount of band bending present in zero bias models from nextnano. E_F was also found from nextnano to be 90 meV and 130 meV for the n-type and p-type GaInNAsSb layers respectively. Both of these parameters required knowledge of the unintentional doping concentrations which are determined from capacitance voltage measurements taken at room temperature.

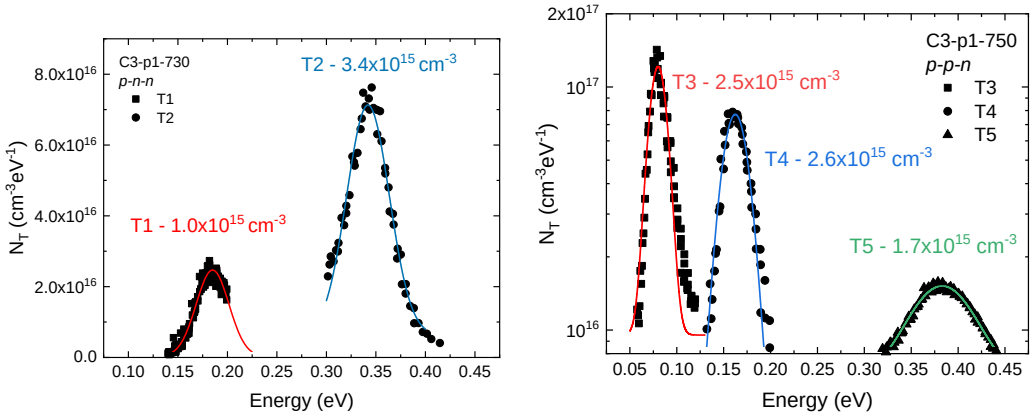

(a) **(b)**

Figure 6.13: The defect density of each level as calculated from the Gaussian fit of the defect density of state, N_T, for (a) the n-type C3-p1-730 and (b) the p-type C3-p1-750.

The defect concentration of the mid gap state, T2 and T5, has decreased with the higher temperature anneal. This defect provides an efficient path for the SRH generation of carriers, and therefore the reduction in concentration of this trap could decrease the

dark current found in the devices.

However, the large increase in shallow traps from T3 and T4 will have a significant contribution to the performance of the device. Since in the n-type material, the concentration of T1 should be larger than any p-type defects such as T3 or T4, as given in equation 6.1, we can assume that the concentration of T3 and T4 is much lower than that for T1. Therefore, we can conclude that the higher temperature anneal is either introducing or promoting the formation of defects T3 and T4 so much that it outnumbers the n-type defects and changes the intrinsic type to p-type. It is not clear how T1 develops with annealing temperature or whether any new n-type defects are introduced with annealing. In order to investigate the dynamics of this defect level, the admittance spectroscopy of another n-type GaInNAsSb layer could be measured at an intermediary annealing temperature step. From this campaign, this would be possible with C3-p1-740 which is a sample immediately before the intrinsic type change.

6.3.1 Uncertainty in defect concentrations

The exact figure given to the defect concentration will have some degree of uncertainty associated with it. Parameters such as V_{bi} and E_f are estimated from nextnano simulations of a material that is not the dilute nitride and cannot be verified experimentally. In order to investigate the impact of the parameters have on the defect concentration, both V_{bi} and E_f were varied by $\pm 10\%$. Importantly, with these two parameters the peak energy is not affected as the terms only feature in equation 4.26.

Parameter	-10%	No Variation	+10%
E_f	$2.53 \times 10^{15}\,\mathrm{cm}^{-3}$	$2.60 \times 10^{15}\,\mathrm{cm}^{-3}$	$2.68 \times 10^{15}\,\mathrm{cm}^{-3}$
V_{bi}	$2.35 \times 10^{15}\,\mathrm{cm}^{-3}$	$2.60 \times 10^{15}\,\mathrm{cm}^{-3}$	$2.90 \times 10^{15}\,\mathrm{cm}^{-3}$

Table 6.1: The effect of different parameters on the results of the defect concentration of trap 4 on sample C3-p1-750.

Table 6.1 shows that the built-in voltage has a significant effect on the defect concentration. This could be minimised in future by using homojunction samples so that the built-in voltage can be measured directly from the samples. However, it is unlikely that this uncertainty would affect the comparison of defects for the same device across annealing conditions since the built-in voltage should remain consistent across the different devices. Therefore, even if the estimation for V_{bi} is inaccurate, the relative defect levels should remain the same.

A further source of uncertainty comes from the equation for defect density used in the study. In previous work, different equations for $N(E)$ are given corresponding to the different ways the applied AC bias will perturb the bands [135]. Walter et al. describes for a n-i-p (or in this study a p-i-n), it is most appropriate to use the linear band bending case [113].

6.3.2 Voltage dependence

Due to the heterojunction between GaInNAsSb and GaAs, there is a possibility that the defect could be caused by the interface rather than occurring as a bulk distributed defect. In previous studies the voltage dependence of the activation energy of the trap was investigated [115]. In theory, for a bulk level, the admittance spectroscopy should reach the same result regardless of bias voltage, however a shift in the peak energy would indicate the defect is related to the interface instead of the bulk of the sample. The justification behind this is described by He et al. [114] to be related by the energy separation between the conduction band minimum and the crossing between the Fermi level with the defect level. As the bias voltage increases, the crossing point changes since the Fermi level at the interface changes with bias so does the separation. Conversely, for a bulk defect the separation remains consistent if it is uniformly distributed through the bulk material.

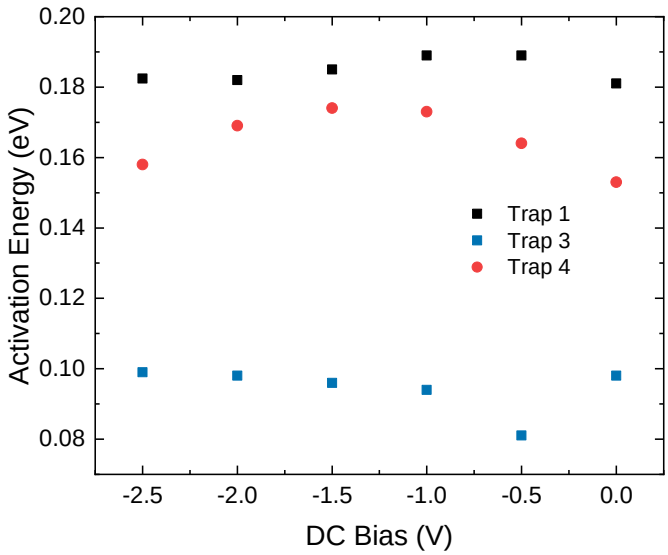

Figure 6.14: The bias dependence of the activation energy for traps 1, 3 and 4. The activation energies do not significantly change beyond the range of uncertainty.

The activation energies of traps 1, 3 and 4 remain constant from zero bias up to a bias of $-2.5\,\mathrm{V}$, as shown on figure 6.14, and therefore can be assumed to be bulk

distributed defects

The activation energies of the mid-gap states cannot be measured as a function of voltage with the range of frequency and temperature available. At the high temperatures at which the mid-gap defects cause a peak in conductance, the baseline of the measurement is rising rapidly which dominates over any peak that would originate from the defect. This is likely caused by the dark current in the samples. A defect associated with the interface of GaInNAsSb and GaAs was found with an activation energy of 0.48 eV [119]. This GaInNAsSb layer had a band gap of 1.0 eV, therefore if the trap stays at the same position relative to the conduction band edge, it would be located 0.22 eV above the valence band. Therefore, this defect is not comparable with any defect identified in this study.

Despite the activation energy remaining constant through the experiment with applied bias, the defect density concentration that did not remain constant with the exception of trap 4. In order to account for bias, equation 4.26 is changed to

$$N_T(E_\omega) = -\frac{(V_{bi}-V)^2}{kTW\left(qV_{bi}-(E_F-E_\omega)\right)}\frac{dC}{d\ln\omega} \tag{6.2}$$

where V is the applied bias [135]. The resultant defect densities with non-zero applied bias are shown in figure 6.15. This trend was found to occur in all models for the defect density as given in reference [135].

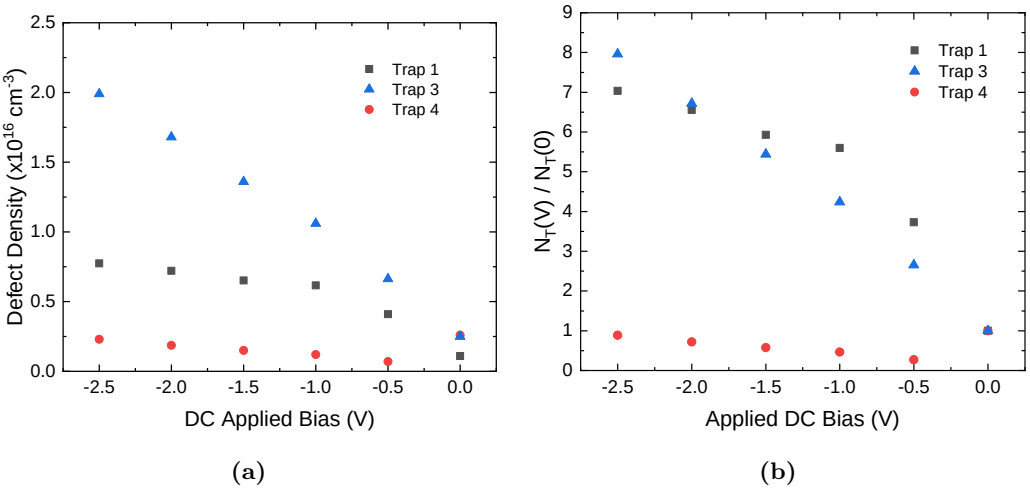

Figure 6.15: The voltage dependent (a) defect density and (b) ratio of defect density as a function of applied bias to the defect density at zero bias for each non-midgap defect.

The largest changes to the defect density concentration come from defects T1 and T3, and these were much larger than the uncertainty as given by the fitting algorithm used. An increase in reverse bias would lead to an increase in depletion width and so

the Fermi level oscillations will be probing the defect levels further away from the p-n interface. Therefore, a change in defect density, specifically an increase, would indicate a higher concentration of defects away from the interface and into the bulk of the device. However, as the junction is positioned in different positions in both devices this would mean that both interfaces at the top and bottom of the device are relatively defect free as compared to the middle of the sample.

Previous experience with the growth of GaInNAsSb has shown that longer growth times can result in unstable temperatures and therefore lead to defect heavy GaInNAsSb at the top of the photodiode. This was thought to have been avoided by a reduction in the intrinsic thickness from 3 µm in campaign one to 1 µm in campaign two onwards. If this temperature instability affected the devices from campaign 2 and beyond, it would lead to a higher defect concentration at the top of the device. This is not seen in device C3-p1-730 as increasing the voltage would move the depletion edge away from the top side and into what would be an area with a lower defect concentration.

In future, a full homojunction sample should be used in place of the double heterojunction design of campaign three. While no defects appear to be created by the interface, the potential barrier between the layers likely affects the small voltage behaviour of the device, similar to the "knee voltage" shown on figure 6.6.

6.3.3 Comparison to the activation energy

The presence of mid-gap states determined from the admittance spectroscopy implies that dark current caused by SRH may be present in these devices. Therefore, the activation energy of the dark current was measured on both the n-type and the p-type samples.

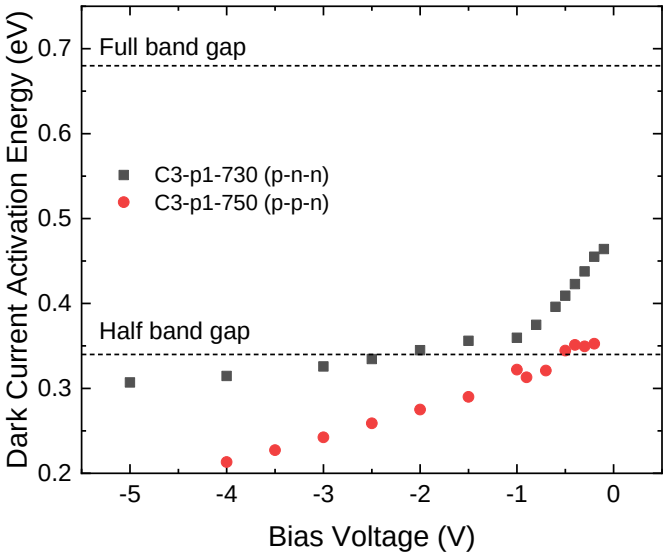

Figure 6.16: The activation energy of the dark current for the devices used in the admittance spectroscopy study. The samples are C3-n1-730 and (black) and C3-n1-750 (red). The half band gap activation energy aligns well with the presence of a mid-gap energy state in the admittance spectroscopy.

For both samples, the activation energy is lower than expected for the devices measured in section 6.1 and lies much closer to the half band gap value as shown on figure 6.16. This implies that SRH method of generation is more significant in these samples compared to the annealed samples C1-p3-785 and C4-n1-730. However, it is unclear if this is due to the concentration of a mid-gap state as n-type C3-p1-730 shows a higher mid-gap defect concentration compared to p-type C3-p1-750. The lower activation energy of C3-p1-750 could be caused by some contribution of the shallow defect levels that are formed during the anneal.

However, it is difficult to extract a decisive conclusion from this data without conducting admittance spectroscopy on the samples measured in section 6.1.

6.4 Effect of annealing time on samples

The post-growth annealing processes were performed at IQE with a process developed from other studies into dilute nitride materials. However, the disadvantage of this method is the minimum sample size that can be annealed is a quarter of a 6″ wafer. At Lancaster, the sample is placed on a ceramic plate so in theory, much smaller sections (roughly $3\,\mathrm{cm}^2$) of the wafer can be annealed. This would allow for much greater flexibility in optimising the annealing temperature, time or any other parameter of the process. As such, the following section is an attempt at replicating the IQE annealing

process using the RTA at Lancaster on small sections of C2-n1-UnA and comparing the band gap, absorption coefficient as well as electrical parameters such as dark current and the depletion width to sample C2-n1-735.

Sample	Band Gap (eV)	Urbach Energy (meV)
Unannealed	0.673	27
735 °C 30 s	0.708	14
735 °C 60 s	0.708	11
735 °C 120 s	0.715	11
C2-n1-735	0.710	11

Table 6.2: A comparison of the band gap and Urbach parameter of an annealed sample from IQE and annealed samples at Lancaster at the same temperature for a range of times.

Figure 6.17a and table 6.2 show that the Lancaster anneal has produced a sample with similar absorption properties to that produced by IQE. Not only has the band gap blueshifted to match C2-n1-735, but the Urbach energy has also decreased to 11 meV. However, it is apparent from section 5.6 that a large absorption coefficient does not necessarily lead to a high quantum efficiency. Therefore, the devices were fabricated and the quantum efficiency was measured and compared to the unannealed sample and the sample annealed by IQE. The results for the quantum efficiency while illuminated by a 1 mW, 1.55 µm laser is shown on figure 6.17b. From this figure, it is found that despite the band gap similarities, the quantum efficiency of the Lancaster annealed samples does not match the IQE sample.

The reason for the disparity could be a difference in the unintentional doping concentration causing a field distribution similar to that of sample C2-n1-UnA as shown by figure 6.17d. The UID concentration appears to be largely unaffected by the annealing and remains at $6 \times 10^{16}\,\mathrm{cm}^{-3}$. Interestingly the dark current from the Lancaster samples has decreased as compared to C2-n1-UnA.

In conclusion, there appear to be many factors related to the annealing process other than the peak temperature that require control. In future, the annealing time can be increased to see if the quantum efficiency matches that of C2-n1-735 and whether the dark current remains low. Despite the differences between the Lancaster and IQE-annealed samples, an interesting outcome of these results is that the blueshift of approximately 40 meV is unavoidable when finding an optimal anneal temperature. Assuming the Lancaster-annealed devices remain different from those annealed by IQE, as they have

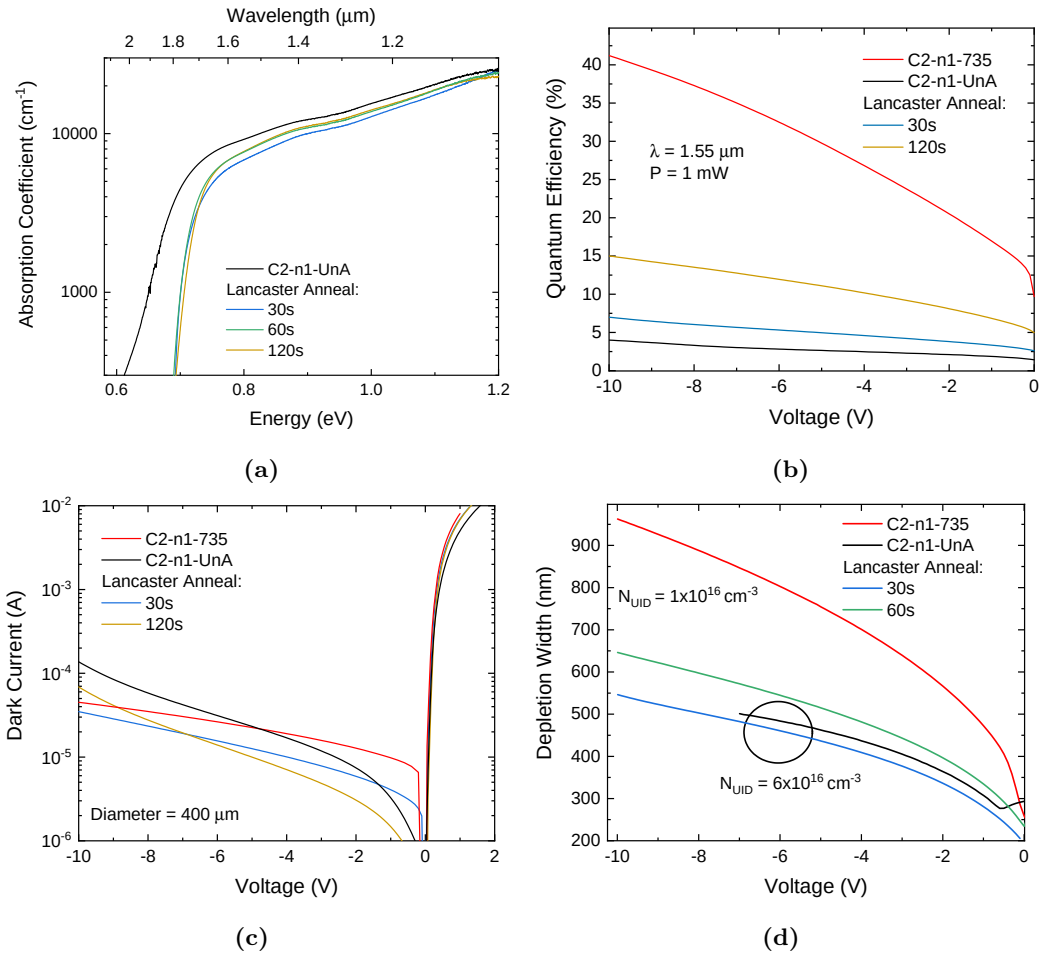

Figure 6.17: The comparison of (a) the absorption coefficient, (b) quantum efficiency, (c) dark current and (d) depletion width of devices annealed at IQE and Lancaster at 735 °C. The unintentional doping concentration is indicated on figure 6.17d with N_{UID}.

not been annealed for a sufficient time, we can conclude that the annealing requirements for the blueshift and the removal of nitrogen related defects is different. Furthermore, the "thermal budget" required for a blueshift is lower than that for the removal of defects.

6.5 Bandwidth

A high bandwidth device requires significantly more time to fabricate compared to the simpler photodetector designs used in the previous sections. Therefore, only the best devices were processed into high bandwidth detectors. These include C2-n1.5-735, C4-n1.5-740 and C4-n1-730. The thicker devices have a higher dark current and unintentional doping compared to C4-n1-730, but the higher intrinsic thickness could lead to a lower capacitance at higher voltages. An SEM image of the finished high bandwidth device is shown in figure 6.18.

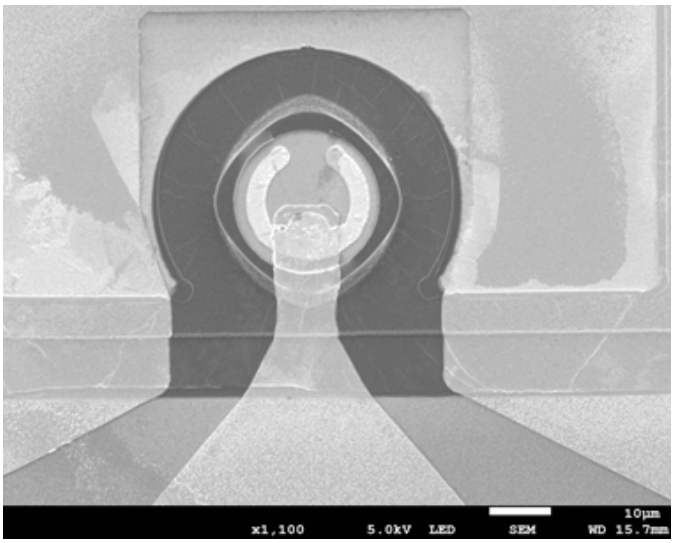

Figure 6.18: An SEM image of the finished high bandwidth device. The device nominally is a circular mesa with diameter 30 µm, but the anisotropic etch removes the circular shape.

A comparison of the DC characteristics such as dark current and capacitance is shown on figures 6.19a and 6.19b. The diameter of the high bandwidth device is nominally 35 µm, but from the SEM image on figure 6.18, the mesa is not completely circular and the diameter varies from 30 µm to 34 µm. The density was calculated with an averaged diameter measurement and therefore there may be some inaccuracy in the dark current density and capacitance density. It is expected that the additional processing steps add parasitic capacitance which is reflected in the increase in capacitance density in figure 6.19b. The level of dark current in this device is encouraging for the application of high speed detectors as the most important parameter is noise rather than signal to noise ratio. Since the detectors are operated with external amplifiers, the dark current should be kept below approximately 1.0 µA in order for the noise generated by the detector to be small compared to the amplifier [52]. In the device shown in figure 6.19a, the dark current is 32 nA, less than an order of magnitude than the required 1.0 µA. However, the dark current from commercial InGaAs photodiodes is usually much smaller. Data-sheets obtained from vendors typically describe a typical dark current in similar sized devices of 3 nA [1].

Figure 6.20 shows the normalised frequency response as measured at Lancaster and at Cardiff with two different experimental setups. The normalised frequency response is the difference in the magnitude of the signal compared to a low frequency result. In the Lancaster measurements this frequency is 1 GHz whereas in the Cardiff measurements

[1] Dark current taken from Albis Optoelectronics, 17/10/2020

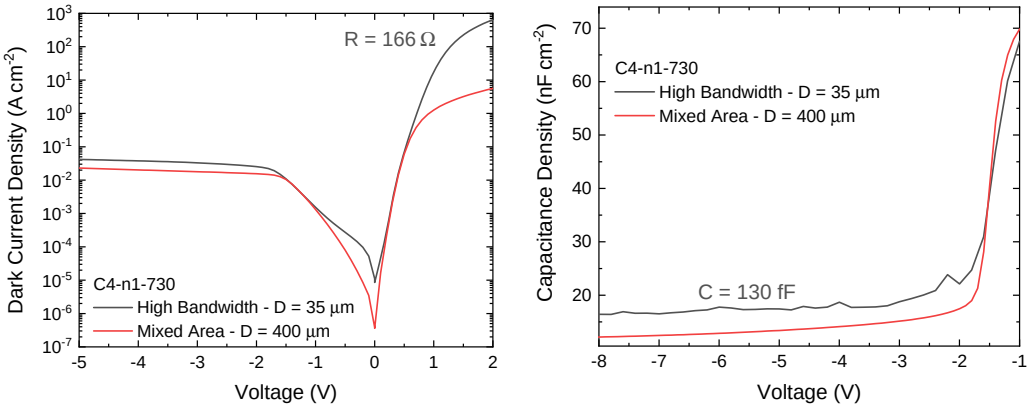

(a) **(b)**

Figure 6.19: A comparison of the (a) dark current density and (b) capacitance density of device C4-n1-730 processed for high bandwidth purposes with the larger mixed area devices.

it is 200 MHz. The Lancaster results show a rippling effect present in all samples; this makes it unclear where the signal falls below 3 dB. Figure 6.20 shows three potential places at 2 GHz, 4.5 GHz and 7.5 GHz. Comparing this to the RC limit as given by measured series resistance and capacitance found from figures 6.19a and 6.19b of 7.4 GHz, it appears that the 3 dB bandwidth should be 7.5 GHz. However, verifying this measurement using the equipment at Cardiff shows that the response crosses the 3 dB point at 4.2 GHz.

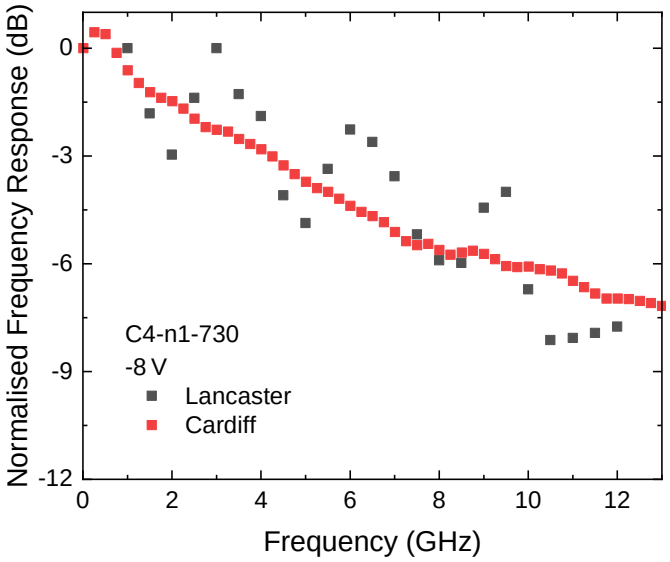

Figure 6.20: The normalised frequency response of a 30 µm device from wafer C4-n1-730 with an applied bias of −8 V.

Despite the lower bandwidth, the frequency response of the Cardiff measurements still appear to follow the RC limit but with a higher resistance than expected. Figures

6.21a and 6.21b show the frequency response at different voltages for devices C4-n1.5-740 and C4-n1-730 respectively along with the theoretical RC behaviour. In order to determine the RC line, the capacitance is found through the model detailed in section 4.4.3. The model outputs a capacitance density, so the true capacitance was found by multiplying by the area of the device as measured using a microscope rather than the nominal diameter. A further 20 fF was added as parasitic capacitance which is related to the additional processing, this value was found as the additional capacitance required to match the capacitance densities on figure 6.19b. This modelling is required as the capacitance of the photodiodes cannot be measured accurately at voltages greater than -8 V.

However, it was found that the capacitance was not changing sufficiently to account for the change in bandwidth as voltage increased. Instead it appears that the series resistance is decreasing as a function of applied bias. The contact resistance of the diode should not depend on the voltage applied, however in this case the quality of the connection of the GSG probe and the contact pads could be improving as the measurements were being taken leading to a lower resistance at higher voltages. Unfortunately, after this trend was found, the measurements cannot be repeated as the Lancaster set up cannot measure the same voltages.

Overall, C4-n1,5-740 reaches the highest bandwidth of 9.2 GHz as shown on figure 6.21c. This bandwidth would be capable of operation at 10 Gbit/s, but because of the high voltage used, the dark current is likely too high for commercial applications. This bandwidth is caused by a smaller resistance as shown by the RC fits on figures 6.21a and 6.21b and a thicker intrinsic width which will lead to a smaller capacitance once a sufficiently large bias is placed on the sample. The resistance of the 25 µm C4-n1.5-740 device is expected to be smaller than the 30 µm device of C4-n1-730 due to the size of the contact, therefore it is unexpected that the resistance found in C4-n1.5-740 is lower. This indicates a poor contact in the experimental set-up, potentially in the contact between the device and the GSG probe as previously mentioned.

The bandwidth is expected to follow RC limits rather than any transit time limitation. The expected transit time limitation, assuming an electron saturated drift velocity of around $4 \times 10^6\,\mathrm{cm\,s^{-1}}$ [136] gives a 3 dB bandwidth of 20 GHz. Furthermore, the dependence of the device size on the frequency response also indicates capacitance is important. Figure 6.21d shows the dependence of the mesa size on the frequency response.

Overall, the bandwidth should increase as the mesa size is decreased due to the

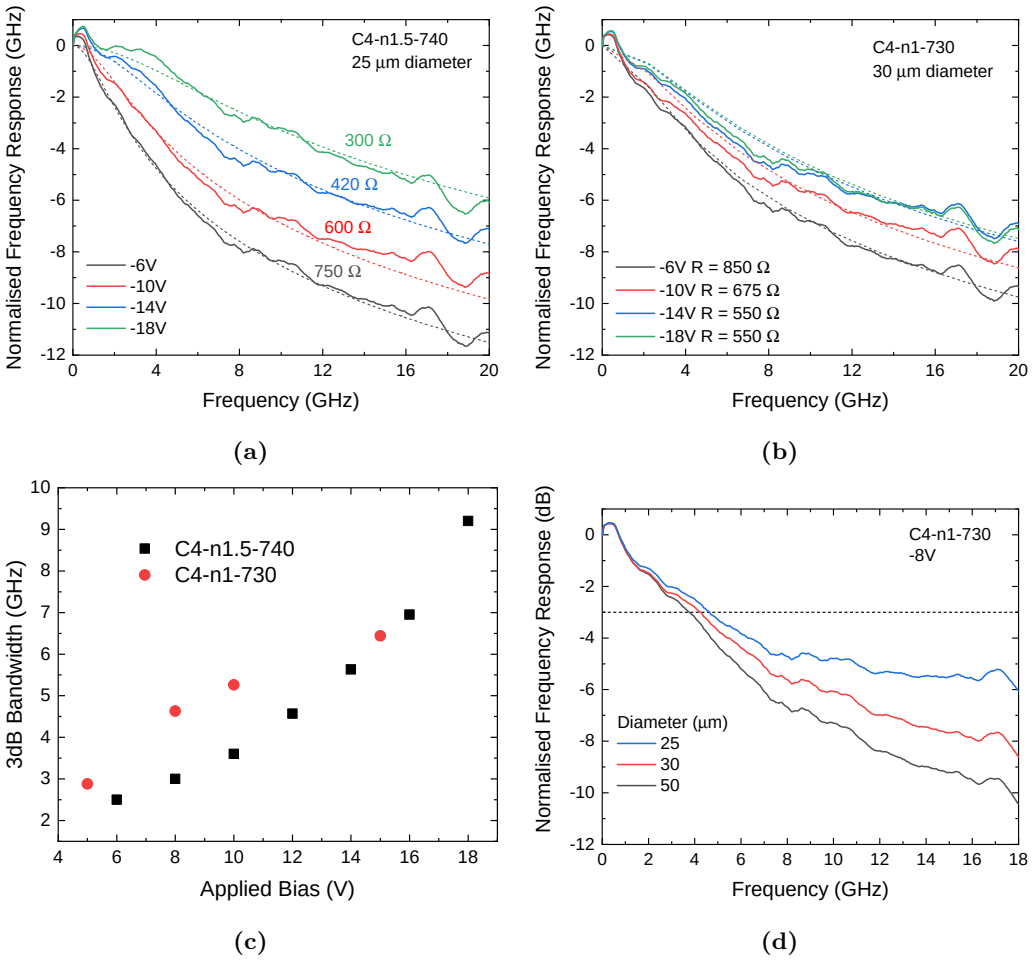

Figure 6.21: The voltage dependence of the bandwidth for samples (a) C4-n1-730 and (b) C4-n1.5-740. The diameter given in these figures is the measurement of the mask used in photolithography rather than a measured value. The dashed line indicates the RC limited response as found from simulated capacitance. (c) The voltage dependence of the 3 dB bandwidth for a 25 µm device from C4-n1-730 (red circle) and C4-n1.5-740 (black circle). (d) The size dependence of the normalised frequency response of sample C4-n1-730.

inverse proportionality of the capacitance to the mesa area, however some difference from expectations can come from an increase of resistance due to the size of the contact placed on top of the mesa decreasing for smaller mesas and therefore increasing the resistance and reducing the bandwidth. As there is a size dependence of the bandwidth on figure 6.21d, a material-based limitation such as transit time can be ruled out at present by reason of no area dependent terms in equation 2.24.

In conclusion, the bandwidth of the photodiodes is slightly slower than current dilute nitride high speed detectors which can operate with a 3 dB bandwidth of 14 GHz [24]. However, this appears to be caused by a large resistance independent of the GaInNAsSb. Furthermore, the current results are exciting as it is the first example of high-speed GaIn-

NAsSb photodiode that is capable of detection at 1.55 µm. Furthermore, the bandwidth measured on C4-n1-730 is comparable to state of the art APDs with InGaAs absorption layers of similar size [40]. Typically, the bandwidth of an APD is reduced compared to a p-i-n due to the avalanche build-up time, however once the resistance found in the measurement is removed the speed of the GaInNAsSb will improve and overtake the speed of the APD.

Chapter 7

GaInNAsSb Photodiode Results Summary

This chapter is intended to summarise the results across all devices in all four campaigns. Since there have been so many different devices, displaying all results graphically can lead to cluttered graphs. Therefore, various results have been complied in the following tables. Each table is also colour coded on a scale from green to red to help show the more optimal devices. This is intended to show in greater detail the decision-making process behind each new campaign.

7.1 Campaign one

	Anneal (°C)	Band gap (eV)	Type	UID conc. (x 1×10^{16} cm^{-3})	J_{dark} (−1 V, mA cm^{-2})	$QE_{1.55}$ (−1 V, 1 mW)
p-i-n	UnA	0.756	n	**27.0**	**0.90**	**4.7%**
3.0 µm	785	0.796	p	**4.4**	**632**	**10.6%**
n-i-p	UnA	0.781	n	**23.0**	**1330**	**1.1%**
3.0 µm	785	0.807	p	**2.5**	**118**	**1.0%**

Table 7.1: The results of the devices of campaign one. Dark current and quantum efficiency are measured with a reverse bias of 1.0 V.

The results of campaign one are shown in table 7.1. All four devices are full GaInNAsSb homojunctions with the structure shown in table 4.2. This campaign did not feature any variation in annealing conditions, but it was found that an anneal at 785 °C changed the intrinsic type from n to p and blueshifted the band gap close to 0.8 eV. This results in

a very low quantum efficiency. Furthermore, it should be noted that the dark current is measured at $-1\,\mathrm{V}$ as the dark current of the annealed samples is too high to be measured at $-5\,\mathrm{V}$ like campaigns three and four.

7.2 Campaign two

Campaign two marked the project's first use of the double heterojunction design and also different annealing temperatures between 735 °C and 835 °C, furthermore, the band gap has been lowered compared to campaign one which allows for a larger quantum efficiency despite the thinner intrinsic region. This change in band gap is likely due to an increased incorporation of nitrogen. The most optimal devices were found to be ones annealed at 735 °C due to the much lower dark current as compared to the other annealing temperatures. Since the intrinsic type of this device had not yet changed from n to p, the reduction in photodiode performance was attributed to the formation of defects at higher annealing temperatures that cause this type switch.

	Anneal (°C)	Band gap (eV)	UID type	UID conc. (x $1 \times 10^{16}\,\mathrm{cm}^{-3}$)	J_{dark} ($-1\,\mathrm{V}$, $\mathrm{mA\,cm}^{-2}$)	$QE_{1.55}$ ($-1\,\mathrm{V}$, $1\,\mathrm{mW}$)
n-i-p 1.0 µm	UnA	0.659	n	**5.5**	**18.0**	**3.6%**
	735	0.712	n	**1.0**	**1.07**	**25.6%**
	760	0.713	p	**1.9**	**275**	**26.3%**
	785	0.731	p	**2.3**	**610**	**20.8%**
	835	0.750	p	**7.2**	**2490**	**4.1%**
n-i-p 1.5 µm	UnA	0.666	-	-	-	-
	735	0.710	-	**3.0**	**9.78**	**10.6%**
	760	0.716	-	-	-	-
	785	0.730	-	**2.4**	**1870**	**20.7%**
	835	0.752	-	-	-	-

Table 7.2: The results of the devices of campaign two. Dark current and quantum efficiency are measured with a reverse bias of 1.0 V.

7.3 Campaign three

This campaign featured a much narrower annealing range from 720 °C to 750 °C which was centred around the most optimal temperature of the last campaign (735 °C). The

band gaps of the unannealed sample and the blueshift due to the annealing is smaller than that of campaign two, which indicates that the composition is not consistent in this campaign. Unfortunately, this could not be measured in the scope of this project and represents a target for any future study. Despite this, the type shift is still visible between 740 °C and 750 °C. The most optimal temperature was considered to be 740 °C due to the large quantum efficiency which is only limited by the intrinsic width and absorption coefficient. This is also the only campaign admittance spectroscopy was applied with the defect analysis applied to samples C3-p1-730 and C3-p1-750.

	Anneal (°C)	Band gap (eV)	UID type	UID conc. (x 1×10^{16} cm^{-3})	J_{dark} (−5 V, mA cm^{-2})	$QE_{1.55}$ (−5 V, 1 mW)
p-i-n 1.0 µm	UnA	0.645	-	-	-	-
	720	0.676	n	**2.0**	**60.1**	**16.1%**
	730	0.680	n	**1.5**	**77.2**	**26.8%**
	740	0.685	n	**3.0**	**39.6**	**41.8%**
	750	0.688	p	**6.0**	**19.0**	**23.9%**
n-i-p 1.0 µm	UnA	0.642	-	-	-	-
	720	0.680	n	**2.0**	**89.9**	**6.6%**
	730	0.682	n	**1.0**	**95.8**	**26.2%**
	740	0.688	n	**1.1**	**142**	**41.0%**
	750	0.698	p	**8.0**	**166**	**30.4%**

Table 7.3: The results of the devices of campaign three. Dark current and quantum efficiency are measured with a reverse bias of 5.0 V.

7.4 Campaign four

Campaign four was the last campaign in this study. It continued the same annealing conditions as campaign three, but the target was to increase the band gap to hopefully reduce the concentration of nitrogen defects. In turn, the temperature at which the type shift occurred was no longer consistent and the most optimal temperature shifted from 740 °C from campaign three to 730 °C. There was also a difference in the photodiode performance of the 1.0 µm devices and the 1.5 µm devices. In general, the thinner devices were had a lower dark current and larger quantum efficiency. For high speed devices, a thickness of 1.0 µm is acceptable as it is a good balance between balancing the transit time of carriers and the RC time constant. However, in future, the growth could be

better controlled over a longer period of time to allow for thicker intrinsic regions and larger quantum efficiencies. In this campaign, high bandwidth devices were fabricated using C4-n1-730 and c4-n1.5-740 due to their low UID concentration of $1 \times 10^{15}\,\mathrm{cm}^{-3}$ and $9 \times 10^{15}\,\mathrm{cm}^{-3}$.

	Anneal (°C)	Band gap (eV)	UID type	UID Conc. (x $1 \times 10^{16}\,\mathrm{cm}^{-3}$)	J_{dark} (−5 V, mA cm^{-2})	$QE_{1.55}$ (−5 V, 1 mW)
p-i-n 1.0 µm	UnA	0.675	n	**7.8**	**18.3**	**3.5%**
	720	0.702	n	**1.3**	**35.3**	**14.2%**
	730	0.706	p	**2.5**	**17.1**	**34.4%**
	740	0.707	p	**4.0**	**17.9**	**27.7%**
	750	0.713	p	**5.0**	**9.8**	**19.2%**
n-i-p 1.0 µm	UnA	0.670	n	**5.0**	**13.6**	**2.8%**
	720	0.701	p	**1.2**	**27.0**	**10.9%**
	730	0.710	p	**0.1**	**23.0**	**34.1%**
	740	0.712	p	**4.0**	**36.7**	**29.5%**
	750	0.722	p	**7.5**	**48.3**	**24.2%**
n-i-p 1.5 µm	UnA	0.668	n	**4.8**	**8.5**	**1.5%**
	720	0.698	n	**1.8**	**14.6**	**5.0%**
	730	0.699	n	**1.3**	**24.8**	**9.1%**
	740	0.710	n	**0.9**	**62.5**	**21.1%**
	750	0.714	p	**8.0**	**91.3**	**27.2%**

Table 7.4: The results of the devices of campaign four. Dark current and quantum efficiency are measured with a reverse bias of 5.0 V.

Chapter 8

Results: GaInNAsSb/AlGaAs Avalanche Photodiodes

This chapter discusses the design of a GaInNAsSb/AlGaAs SAM APD. The first part of this chapter discusses the multiplication possible in GaInNAsSb devices by both pure and mixed carrier injection. Secondly, the chapter uses GaAs/AlGaAs SAM APDs in order to refine the conditions required for the charge sheet layer of the APD. This lays the groundwork required for the growth of GaInNAsSb/AlGaAs SAM APDs in the future.

8.1 GaInNAsSb multiplication

In the design of SAM APDs, the impact ionisation should be limited to the multiplication layer of the device as any gain from the absorber can have a detrimental effect on the noise [137]. According to Ng et al. [137], this effect increases if any feedback carriers from the multiplication layer can ionise in the absorber. In the case of GaInNAsSb/AlGaAs APDs, the injected carrier will be the electron and so if feedback holes can ionise in the absorber to allow for the further injection of electrons into the AlGaAs multiplication region, the noise will increase.

Impact ionisation in dilute nitrides has both been discussed theoretically and demonstrated experimentally for certain compositions. Initially it was thought that due to the increased amount of N-related scattering centres, the electron impact ionisation coefficient would dramatically decrease [96, 138] but not affect β due to the lack of any effect of N on the hole mobility [139]. This could lead to a low value for $k = \frac{\alpha}{\beta}$, and thus a hole-initiated GaInNAs APD would be operated with very low noise.

However, attempts at measuring the noise of a dilute nitride APD or the impact

ionisation coefficients have not yielded the predicted results. Kinsey et al. [140] produced a GaAsN APD with a value for k which has little improvement over GaAs APDs of similar width. Tan et al. [98] measured both the electron and hole impact ionisation coefficients for GaInNAs ($E_g > 0.95\,\text{eV}$). While α drops as predicted compared to GaAs, β also drops so that there are no overall improvements to k and the predicted noise.

Both of these studies differ from the dilute nitride covered in this study. First of all, the dilute nitride alloy used by Kinsey et al. contains no In and only enough N to increase the cut-off wavelength to 1.0 µm. Tan et al. reach a longer wavelength with an In-containing alloy, but they still have a wider band gap than this study. Furthermore, the effect of Sb is not discussed, and since it is believed to affect the valence band position, it may reduce β. Therefore, the following section discusses impact ionisation on several GaInNAsSb samples.

8.1.1 Pure injection - campaign one

The pure injection of carriers was achieved in two devices from campaign one: C1-p3-785 and C1-n3-785, pure electron and hole injection of carriers respectively. The multiplication characteristics of each photodiode is shown on figure 8.1. The plot shows M-1 instead of M so that the effects of additional carriers generated due to avalanche gain are highlighted. The multiplication is measured until the dark current is too high for the lock-in amplifier to distinguish the chopped photocurrent. Typically, this occurs when the dark current reaches 1 mA.

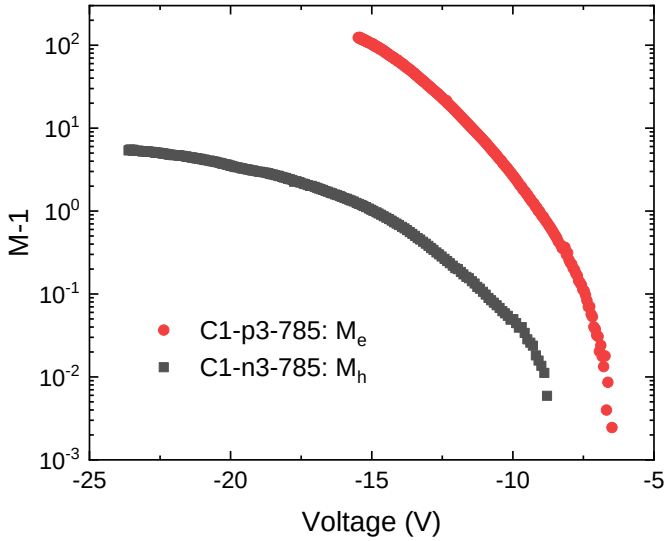

Figure 8.1: The multiplication characteristics of GaInNAsSb that is initiated purely by a single type of carrier, holes for the p-i-n (red) and electrons for the n-i-p (black).

From figure 8.1, it is readily apparent that gain in the p-i-n is much greater than that for the n-i-p for the same voltage, however the impact ionisation coefficients, α and β, are dependent on the electric field rather than the voltage. The difference in electric fields is caused by differences in the unintentional doping concentrations in the samples. Therefore, to find the electric field profile of devices C1-p3-785 and C1-n3-785, the capacitance-voltage characteristics were measured and compared to that calculated by the method in section 4.4.3. The input device file was then adjusted to fit the experimentally measured CV. The electric field profile was calculated from the depletion width of the sample. However, due to the relatively high UID concentration of these samples, the field varies significantly across the intrinsic GaInNAsSb layer, therefore the peak electric field at each voltage was taken and plotted against the multiplication in figure 8.2a.

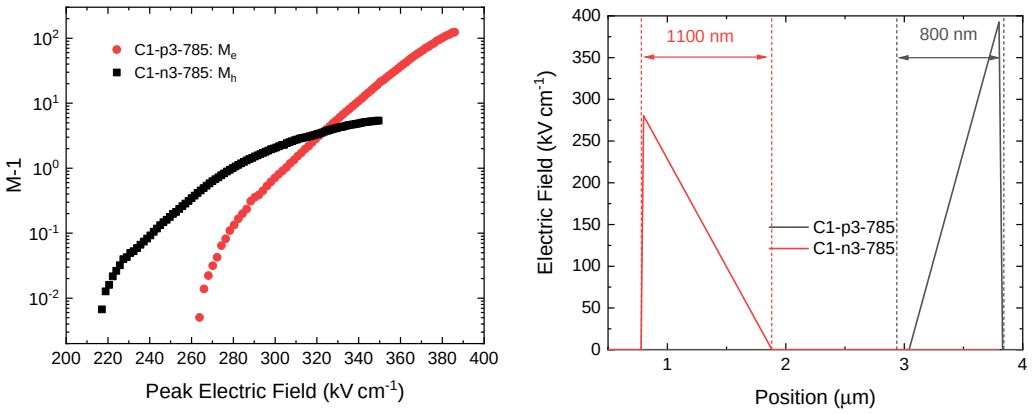

(a) **(b)**

Figure 8.2: (a) The multiplication characteristics for the homojunction p-i-n and n-i-p devices against the peak electric field. (b) The electric field profiles for the two devices at a consistent voltage of -15 V. The difference in peak electric field and depletion width is caused by differences in unintentional doping concentration.

An unusual aspect of the results in figure 8.2a is the crossover between the gain curves for hole and electron-initiated multiplication. Typically, in III-V semiconductors, the impact ionisation coefficients are dissimilar and for two identical devices, the gain curves would not cross. However, samples C1-p3-785 and C1-n3-785 have different unintentional doping concentrations and different junction positions. Since the intrinsic region is not fully depleted, the electric field profile in the devices is triangular, with the peak of the field at the junction and slowly decreasing further into the depletion region. As the junction is positioned differently in both devices; injected holes enter the field from the cladding while electrons enter the field from the intrinsic region. This can lead to an

difference in multiplication and also the crossing of the gain curves found in figure 8.2a.

An evolutionary fitting algorithm was applied using the RPL and capacitance simulations as described previously in section 2.4. This method successfully fitted the impact ionisation coefficients of $Al_{0.9}Ga_{0.1}As_{0.08}Sb_{0.92}$ for three separate devices [141]. However, this method did not result in determining accurate impact ionisation coefficients for GaInNAsSb. This may be caused by a large difference between the initial impact ionisation coefficients which started the evolutionary fitting algorithm and the real coefficients of the material. The algorithm was initiated with the impact ionisation coefficients of similar band gap material such as InGaAs [142] and GaInNAs [98]. However, these coefficients that resulted from these starting positions could not describe the steady increase of hole-initiated multiplication or the rapid increase of electron-initiated multiplication. Since this work has been attempted, a study into the impact ionisation coefficients of GaN has found that β is relatively constant across electric fields but α is highly dependent on electric field such that the low-field multiplication is purely initiated by holes [143]. However, once the field is increased, $\alpha >> \beta$ and the multiplication is almost entirely generated by electrons. A similar dependence of coefficients on electric field could explain the trend found in figure 8.2a. Therefore, in future the evolutionary fitting algorithm could be seeded with coefficients that behave similarly to that found in GaN, but at much lower electric fields.

Alternatively, some of the gain in the n-i-p could be caused by photon recycling from the pure injection. This is the radiative recombination of carriers in the GaAs cap layer, which then may cause the creation of electron-hole pairs further in the device and lead to the injection of electrons. However, it is unlikely for two reasons. First of all, since the intrinsic region is p-type, the p-n junction is at the top of the device. This means carriers must diffuse through 500 nm of GaAs and 300 nm of n-type GaInNAsSb before reaching the intrinsic region and the electric field. These layers are relatively thin compared to the diffusion length of holes in GaAs which is approximately 1 µm [144]. Secondly, photon recycling would be observed in materials with a very large difference in impact ionisation coefficients such as hole-initiated multiplication in InAs. Due to the very early onset of M_h and significant levels of multiplication before the onset of M_e, we can conclude that β is not negligible and multiplication found in C1-n1-785 does not have to be caused by the impure injection of carriers.

Regardless of the behaviour of the multiplication, this evidence suggests that the electric field in the absorber of a SAM APD should be kept below 200 kV cm^{-1} in order

to avoid multiplication. However, this level of electric field should already be avoided as a large amount of dark current could be generated from this electric field.

8.1.2 Mixed injection - campaign four

The pure injection of photogenerated carriers cannot be achieved in the double heterojunction devices for two reasons. First, the cap layer is not thick enough to absorb enough of the light to ensure there is pure injection (400 nm compared to 800 nm). This means there will be some absorption in the depletion region and reduce the quality of the data. Secondly, the heterointerface in C4-n1-730 leads to a large band discontinuity where within 20 nm the valence band maxima has shifted by 0.8 eV. In addition, the electrostatic junction is placed over this interface so that the carriers are subject to an electric field as they enter the GaInNAsSb. Therefore, it is energetically possible for ionisation to occur from the diffusion of holes from the n-GaAs layer into the GaInNAsSb layer. This method of multiplication is the principle behind the staircase avalanche photodiode by Ren et al. [145]. This is not a concern in the homojunction devices as carriers generated in the GaAs layer have a 300 nm GaInNAsSb region in which ionisation due to the step in energy can occur before it enters the electric field. If ionisation occurs before this electric field, it should not affect the gain characteristic of the device and instead only influence the initial primary photocurrent.

Therefore, instead of pure injection, avalanche gain caused by the mixed injection of carriers was measured. This was achieved using a 1.55 µm laser operating at a power of 1 mW. The laser was attenuated by a fixed FC/PC 25 dB attenuator as the power of the laser influences the electric field in the device and therefore would influence the possible multiplication. The results are shown in figure [**?**].

Multiplication through the mixed injection of carriers in C4-n1-730 appears to initiate gain at an earlier voltage and reach high multiplication at a lower electric field compared to the homojunction devices. This may be attributed to the lower band gap of C4-n1-730 compared to the homojunction devices as a lower threshold energy would be required for impact ionisation. However, it is more likely due to the electric field covering the entire intrinsic region due to the low unintentional doping in C4-n1-730. As the mixed injection profile is more representative of the absorption profile of an absorber in a SAM APD, the charge sheet should be designed so that the electric field is limited to 100 $\mathrm{kV\,cm^{-1}}$

Furthermore, a multiplication of 100 is reached without a sharp breakdown of the device, instead a limit imposed by dark current is reached. This is further evidence of

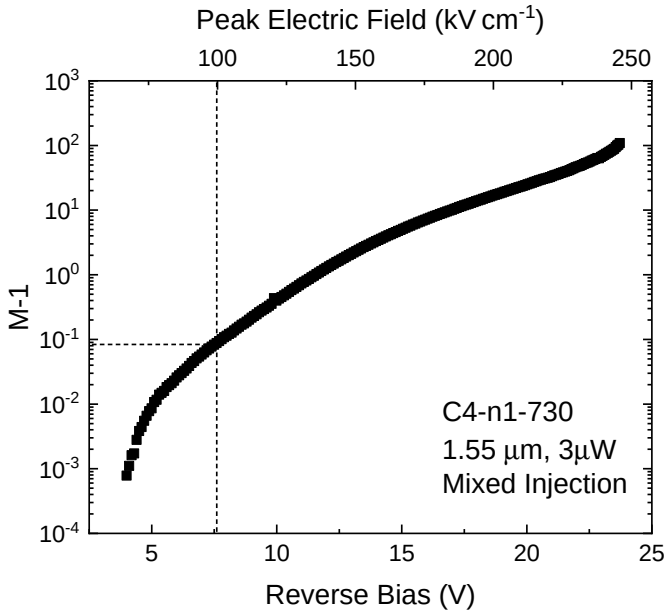

Figure 8.3: The multiplication characteristic of a double heterojunction p-i-n with mixed injection of a laser operating at 1.55 µm.

highly dissimilar impact ionisation coefficients. Such a disparity is useful for low noise APDs, however dark current densities of $2.5\,\mathrm{A\,cm^{-2}}$ rule out the use of GaInNAsSb as an avalanche material at present.

8.2 The modelling and designing of APDs

Band edges

As the GaInNAsSb layer has a much smaller band gap than the AlGaAs multiplication layer, the conduction band offsets between the two materials can be significant. This could inhibit the transport of photo-generated electrons from the absorber to the multiplication layer. Using nextnano, the band structure of the APD was simulated with and without the use of grading layers. This is shown on figure 8.4. The large 1.2 eV barrier is significant so the use of GaAs and $Al_{0.4}Ga_{0.6}As$ reduces this into three smaller barriers.

In the design of the APD, the doping and thicknesses of the grading layers were chosen so that an electron travelling ballistically through the layer, would gain an energy greater than that of the barrier. The layer is intentionally doped with a concentration of $2 \times 10^{17}\,\mathrm{cm^{-3}}$ in order to have a small effect on the electric field in the charge sheet layer, but also to maintain an electric field within the grading layer. This will have the result of affecting the multiplication and punch-through voltage of the APD, so the

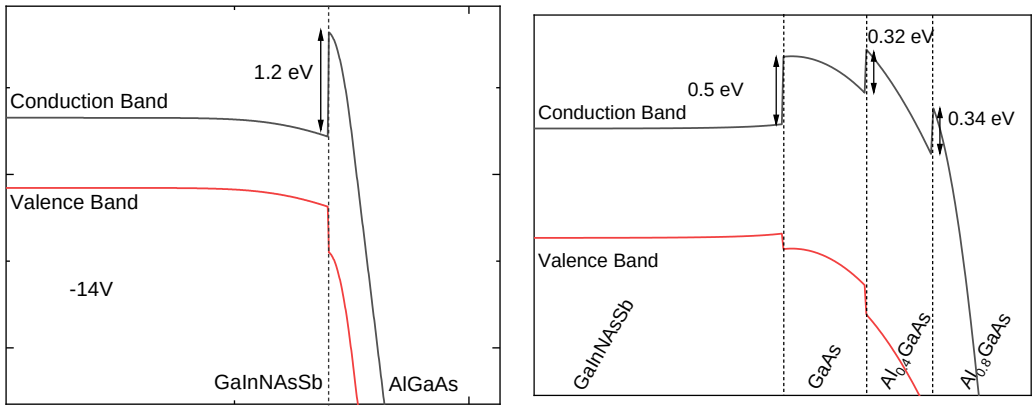

Figure 8.4: The band edges of the GaInNAsSb/AlGaAs APDs (a) with and (b) without grading layers at punch-through.

doping level of the charge sheet will have to be designed around the doping present in the grading layers.

Charge sheet variation

The charge sheet is the most important layer in the APD so that the doping and thickness of the layer must be carefully designed. If the doping is too high, or the layer too thick the electric field may not reach the absorber before the multiplication layer has already achieved breakdown. Alternatively, if the doping is too low the electric field in the absorber will be too high at voltages required for multiplication. It is common in APD design to grow several iterations which are intentionally doped either side of the nominal design. This allows some room for uncertainty in implementing the design.

The effect of the GaInNAsSb intrinsic type

As discussed in section 6.2, the unintentional doping concentration and type of GaInNAsSb is subject to the annealing conditions applied to the GaInNAsSb. If the dilute nitride remains n-type after the post-growth anneal, there will be three electrostatic junctions in the device: between the absorber layer and the p-cladding and grading layers and the intended junction at the multiplication region. These electric fields will interfere with each other as shown in figure 8.5.

The effect of the intrinsic doping is twofold, first of all the electric field in the absorber appears to start depleting away from the grading and charge sheet and secondly the magnitude of the electric field in the multiplication layer has reduced. These will not

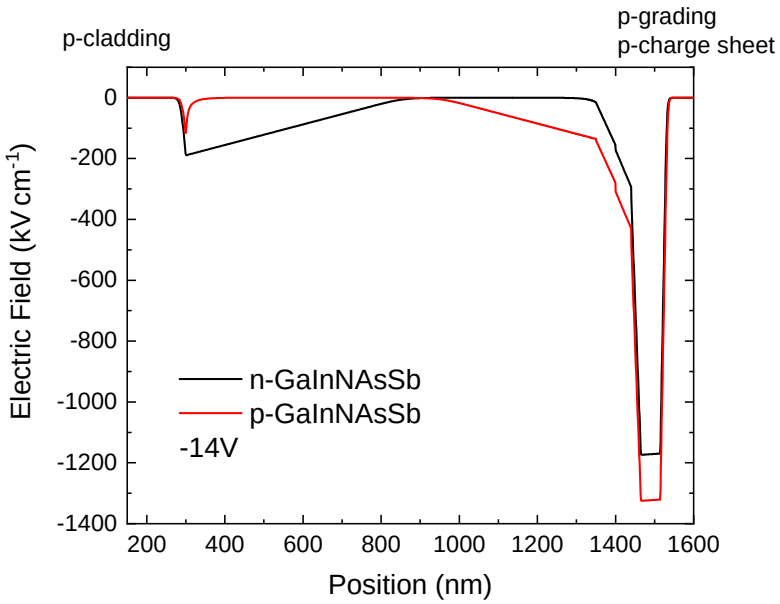

Figure 8.5: The effect on the electric field with the intrinsic type of the GaInNAsSb absorber layer. The doping concentrations of all layers and the type of the other layers have been kept constant. The simulation was achieved using nextnano and a bias voltage of $-14\,\mathrm{V}$.

only affect the collection of any photogenerated carriers but also influence the breakdown of the APD.

8.3 GaAs APD

Due to the complications that are included in the growth of the dilute nitride layer, a version of the APD with GaAs as an absorber was grown. This would allow for the ideal charge sheet conditions to be found before the GaInNAsSb layer would be added in place of the GaAs absorber. The GaAs absorber was intentionally doped to be p-type with a concentration similar to that of a GaInNAsSb at $4.0 \times 10^{16}\,\mathrm{cm}^{-3}$

Layer	Material	Thickness (nm)	Doping (cm^{-3})	
Contact	GaAs	100	p	5.0×10^{18}
Cladding	GaAs	200	p	1.0×10^{18}
Absorber	GaAs	1000	p	4.0×10^{16}
Grading 1	GaAs	50	p	2.0×10^{17}
Grading 2	$Al_{0.4}Ga_{0.6}As$	40	p	2.0×10^{17}
Charge Sheet	$Al_{0.8}Ga_{0.2}As$	25	p	1.5×10^{18}
Multiplication	$Al_{0.8}Ga_{0.2}As$	50	UID	-
Cladding	$Al_{0.8}Ga_{0.2}As$	250	n	1.0×10^{18}
Contact	GaAs	1000	n	5.0×10^{18}
Semi-Insulating GaAs Substrate				

Table 8.1: The design for the GaAs APD. Other designs were fabricated based around the doping and thickness of the charge sheet of this design.

In order to measure a sufficient range of samples, a default device was chosen with the device design in table 8.1, this device is named sample 3. Then, the thickness and doping levels of the charge sheet were systematically altered for a range of devices. The exact intended thicknesses and doping concentrations are shown in table 8.2.

	Doping Increases →		
	Sample 1 18 nm 2.0×10^{18}		
Thickness Increases ↓	Sample 2 25 nm 1.5×10^{18}	Sample 3 25 nm 2.0×10^{18}	Sample 4 25 nm 2.4×10^{18}
	Sample 5 32 nm 2.0×10^{18}		

Table 8.2: The range of GaAs-based APDs in this study. The cell contains information of the sample number, the charge sheet thickness and the charge sheet doping (specified in cm^{-3}).

The thickness and doping concentrations of the charge sheet on samples 1, 2, 4 and 5 were chosen for particular electric field conditions in the absorber and multiplication region. Samples 1 and 2 contain less dopant than sample 3 so that not only the punch-through of electric field into the absorber is earlier, but the breakdown of the AlGaAs layer occurs at a later voltage. This is shown on figures 8.6a and 8.6b. This causes the electric field in the absorber layer to be higher. In samples 1 and 2, the charge sheet is

designed so that the electric field in the absorber reaches 250 kV cm^{-1} at a multiplication of 10. Whereas samples 4 and 5 are chosen so that breakdown occurs at approximately the same voltage as punch-through. This should cover a wide range of doping conditions, and even with uncertainty originating from the growth conditions, at least one sample should return a functional APD.

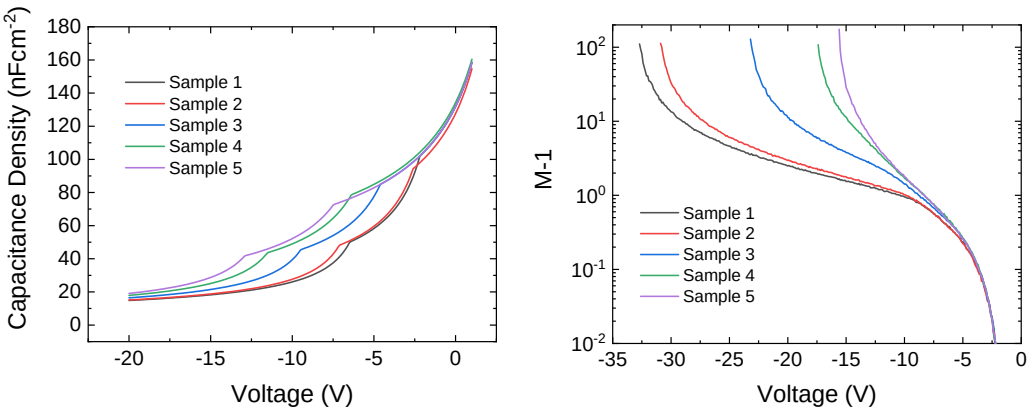

Figure 8.6: The modelled (a) capacitance and (b) gain of the GaAs/AlGaAs APDs.

8.3.1 IV and CV characteristics

The photocurrent of the GaAs/AlGaAs APDs were measured by illuminating the devices using the visible wavelength lamp used for illuminating the sample for probing. This lamp is not calibrated or uniform so there is no measure of responsivity or quantum efficiency. However, it can provide an indication of the collection of photogenerated carriers. This should reasonably replicate the GaInNAsSb/AlGaAs behaviour as the light should almost entirely be absorbed in the top GaAs absorber region before it reaches the AlGaAs layers. Figure 8.7 shows the photocurrent for all five samples. The photocurrent is measured until the dark current breakdown of the device.

Only samples 1 and 2 display the typical characteristic of photocurrent for APDs where there is essentially no photocurrent until punch-though at -6 V, but large amounts of photocurrent afterwards, in this case $> 10^{-6}$A, before breaking down. While sample 3 does appear to punch-though at -9 V, the breakdown is too soon after punch-through to see the consistently high photocurrents that are observed in samples 1 and 2. The most highly doped samples, 4 and 5, both appear to breakdown just as punch-through is happening and therefore are not suitable for APD applications.

The capacitance of APDs is shown in figure 8.8. The voltage at which the charge sheet depletes is similar to the expectations of the capacitance model in figure 8.6a. Further-

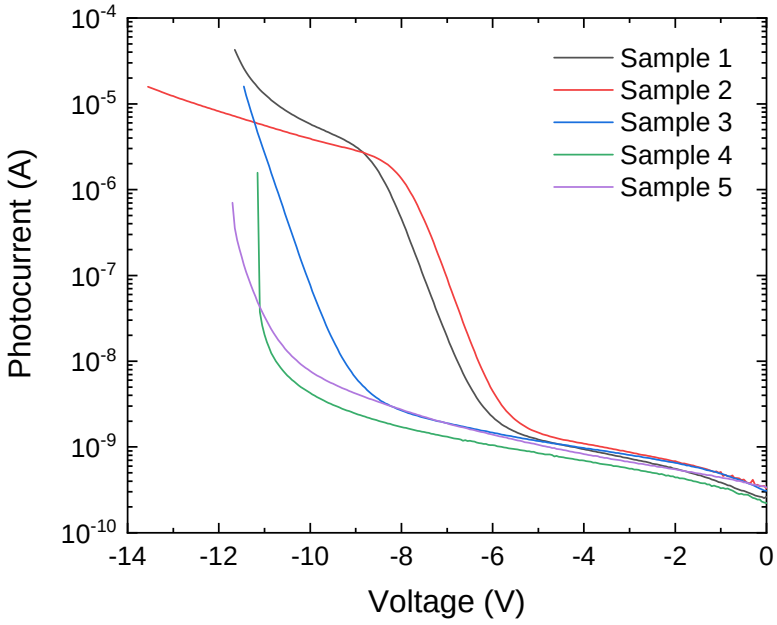

Figure 8.7: The photocurrent in each GaAs APD when illuminated by a visible LED source. Light is detected in all samples, but only in significant quantities for samples 1 & 2.

more, samples 1 and 2 show some punch-through into the absorber. The photocurrent may appear to show punch-through earlier as the grading layers are also capable of absorption at the illumination wavelengths used.

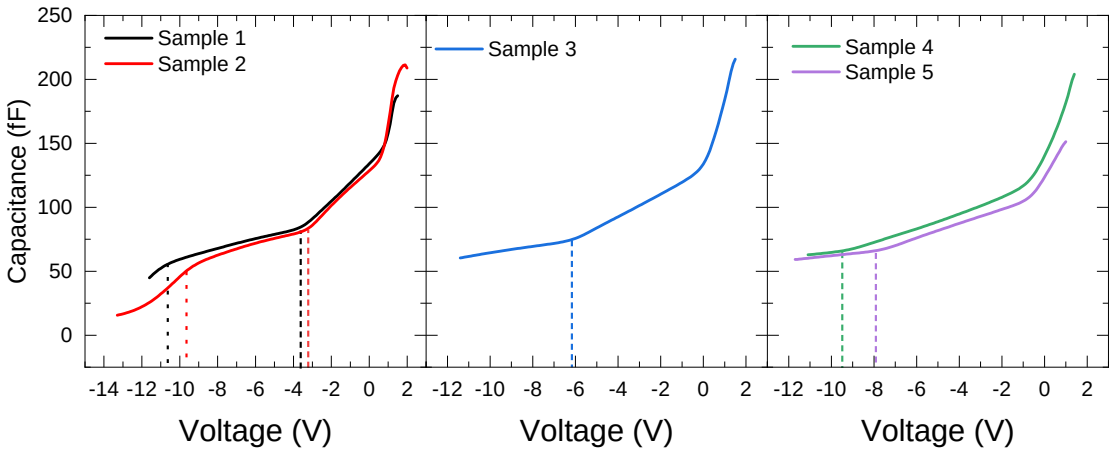

Figure 8.8: The capacitance-voltage characteristics of all five GaAs/AlGaAs APDs. The dashed line signifies the full depletion of the charge sheet and the dotted line on sample 1 and 2 indicates the full depletion of the grading layers and absorber punch-through.

However, the RPL model predicted a much larger difference in breakdown voltages than the measured values. The results as shown on figure 8.7 indicate a breakdown voltage of approximately $-12\,\mathrm{V}$ for all samples with the exception of sample 2 which breaks down at a voltage of $-14\,\mathrm{V}$. In order to investigate the source of the breakdown voltage, the capacitance model was used to find the actual doping profile of sample 2.

Some differences between the planned doping in the charge sheet and grading layers and the actual doping can occur due to the diffusion of dopants across the layers. Therefore, when attempting to fit the calculated capacitance of the APD to the measured value, the doping of the input device was changed rather than the thickness of the layers. The device structure used in the capacitance simulation is shown on table 8.3 and the comparison to the measured CV is shown in figure 8.9a. The electric field profile calculated from the modelled device structure at the breakdown voltage for the real sample is shown on figure 8.9b.

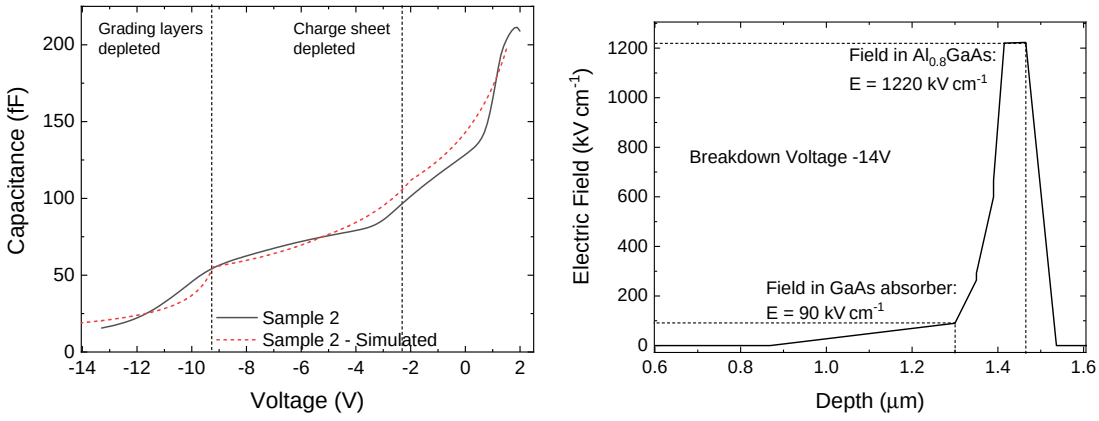

(a) **(b)** .

Figure 8.9: (a) A comparison of the fitted capacitance (dashed) with the experimentally measured capacitance (solid) for sample 2 on a 400 µm diameter device. (b) The electric field at breakdown can be easily extracted once the correct input device for the simulated capacitance is found.

Layer	Material	Thickness (nm)	Doping (cm^{-3})		Modelled Doping (cm^{-3})
Contact	GaAs	100	p	5.0×10^{18}	5.0×10^{18}
Cladding	GaAs	200	p	1.0×10^{18}	1.0×10^{18}
Absorber	GaAs	1000	p	4.0×10^{16}	1.5×10^{16}
Grading 1	GaAs	50	p	2.0×10^{17}	2.5×10^{17}
Grading 2	$Al_{0.4}Ga_{0.6}As$	40	p	2.0×10^{17}	5.0×10^{17}
Charge Sheet	$Al_{0.8}Ga_{0.2}As$	25	p	1.5×10^{18}	1.3×10^{18}
Multiplication	$Al_{0.8}Ga_{0.2}As$	50	UID	-	(p) 3.0×10^{15}
Cladding	$Al_{0.8}Ga_{0.2}As$	250	n	1.0×10^{18}	1.0×10^{18}
Contact	GaAs	1000	n	5.0×10^{18}	5.0×10^{18}
Semi-Insulating GaAs Substrate					

Table 8.3: The doping concentrations used in the model shown in figure 8.9a as compared to the intentional doping levels.

Figure 8.9b shows that at the breakdown voltage of sample 2, the electric field in the multiplication layer is 1220 kV cm^{-1}, whereas the RPL model predicts a breakdown when the electric field reaches 1500 kV cm^{-1}. We can attribute this to an overestimation of electric field caused by an inaccuracy of the RPL to account for thin multiplication thicknesses. This was verified by comparing the breakdown voltage and electric field of AlGaAs APDs from other studies where electric fields of 1200 kV cm^{-1} were required to achieve breakdown in the thin APDs from these studies. Typically, the accuracy of the RPL is improved by splitting the multiplication layer into a larger number of strips. However, the same breakdown field of 1500 kV cm^{-1} was required for a range of strips from 500 to 500000. Beyond 500000 strips, the simulation (which is coded in Java) encounters memory issues and cannot be run further.

Therefore, in future, this particular RPL model cannot be relied upon for the design of thin APDs. Instead, breakdown and punch-through can be calculated through the electric field. However, as the method for calculating gain used in the p-i-n photodiodes is no longer applicable as there will be no primary photocurrent at low voltages, the RPL could provide a method in calculating an accurate voltage dependence of gain. However, in the case of 50 nm APDs, we will have to rely upon different methods.

The gain can still be calculated through knowledge of the maximum primary photocurrent possible through the absorption coefficient and thickness of the absorber layer. However, this relies on the complete collection of carriers through a fully depleted absorber layer which requires a low unintentional doping concentration and optimal annealing conditions of the GaInNAsSb.

In conclusion, the design of a GaAs/AlGaAs APD has been demonstrated despite the error in the modelling of the multiplication. Sample 2 showed the most optimal doping and thickness condition of the charge sheet, so the same conditions of growth for sample 2 should be used with a GaInNAsSb absorber layer. The doping of the charge sheet can further be decreased in order to allow for a greater width of electric field in the absorber and reduce the punch-through voltage as the electric field in the absorber layer is still lower than the target of 100 kV cm^{-1} outlined in figure 8.3.

Chapter 9

Conclusion

9.1 Conclusion

The research intended to show the characteristics of GaInNAsSb photodiodes lattice matched to GaAs for the purposes of NIR detection and in particular for telecommunication applications. This would first require a GaInNAsSb photodiode to be able to detect wavelengths such as 1.3 µm and 1.55 µm. Secondly, the dark current and depletion width would have to be suitable to allow the collection of photocurrent. Finally, it would be required to operate at high speeds in order to compete with the industry standard for photodetectors at this wavelength, InGaAs.

Chapter 5 analysed the optical properties of the GaInNAsSb photodiodes fabricated in this study. The band gap of unannealed GaInNAsSb in this study was found to be among the lowest ever epitaxially grown such as device C2-n1-UnA which has a band gap of 0.659 eV. The post-growth anneal applied to the samples blueshifted the GaInNAsSb by approximately 40 meV in campaigns two, three and four. Therefore, the unannealed samples had a sufficiently low band gap such that the annealed devices were not only suitable for detection at 1.55 µm, but also had a lower band gap than InGaAs (0.74 eV). For instance, in campaign four, the optimal annealing conditions resulted in a band gap of 0.71 eV, therefore, in the future, the nitrogen incorporation could even be reduced with the aim of improving the dark current and UID concentration.

In addition, the band gap we observed in campaigns two, three and four results in an absorption coefficient slightly higher than InGaAs at 1.55 µm. The difference has very little effect on the quantum efficiency compared to InGaAs photodiodes but does provide a large external quantum efficiency with maximums of 41% and 38% in campaigns three and four respectively. However, some limitations are present, such as the linearity of

photocurrent at high input optical powers. This linearity is lost at approximately 1 mW at −5 V. Increasing the applied bias can increase the power that linearity is lost at, but avalanche multiplication should be avoided. Furthermore, it was found that if the annealing conditions are not optimised sufficiently, then the quantum efficiency is lower than the expected minimum value calculated from the absorption coefficient and depletion width, which indicates the poor collection of photogenerated carriers even within an electric field. However, this result is the highest quantum efficiency measured at a wavelength of 1.55 µm. The maximum responsivity without the presence of avalanche gain is 0.51 A W^{-1} in device C3-p1-740 which is greater than waveguide photodiodes of a similar alloy [90] and vertically illuminated photodiodes [73, 89].

Chapter 6 discussed the electrical properties of the GaInNAsSb photodiodes. First, the dark current was shown to be dependent on the annealing conditions. Specifically, from the temperature dependent dark current measurements it is found that the activation energy increases for the annealed samples. This is likely caused by a decrease in defects which would otherwise lead to the generation of carriers contributing to dark current. The dark current was found to be higher than that for InGaAs, however, the dark current is comparable to other dilute nitride samples with slightly higher band gaps [89].

Secondly, the unintentional doping concentration was found to be minimised after annealing at approximately 730 °C, however annealing above this temperature has led to high concentrations, highlighting the importance of optimising the temperature.

Thirdly, the samples consistently showed n-type GaInNAsSb layers before switching to p-type at sufficiently high temperatures. This switch of intrinsic type was investigated by admittance spectroscopy and it was found that annealing had introduced or encouraged the formation of two p-type defects which are likely responsible for high leakage, unintentional doping concentration and type switch.

Finally, in chapter 6, the bandwidth was measured on the most optimal samples from the previous measurements. The 3 dB bandwidth of the detectors was found to be capable of operation at 10 Gbs^{-1} and limited by the RC time constant of the photodiodes. The highest bandwidth measured was 9.2 GHz, although the voltage at which this bandwidth is measured is −18 V and at this voltage the dark current in the photodiode is very large and impact ionisation is likely present. However, this result is significant as it is the first example of a high-speed dilute nitride detector that can operate at 1.55 µm and this level of speed of detector could be used in the intended fibre to the

home applications targeted by the project. Further improvements to the bandwidth can be achieved by the reduction of the contact resistance of the photodiodes, both in the fabrication and measurement steps of the experiment.

Chapter 8 discusses the progress made towards a GaInNAsSb/AlGaAs SAM APD. Such a SAM APD would allow for extremely thin avalanche layers which would lead to low noise operation as compared to InGaAs/AlInAs SAM APDs. Control of the electric field in the absorber is important not only to reduce the dark current in the layer, but also to limit any potential impact ionisation that occurs outside of the multiplication region. Therefore, the multiplication caused by pure and mixed injection was measured on homojunction and double heterojunction samples. The multiplication controlled by pure injection potentially indicated a large mismatch in the impact ionisation from the difference in the p-i-n and n-i-p gain curves. However, this also may have been caused by a difference in electric field profile and further study is needed. The mixed injection multiplication was more representative of the injection profile in a depleted absorber in a SAM APD and showed the onset of multiplication at an electric field of $100\,\mathrm{kV\,cm^{-1}}$. The smaller electric field is related to the wide depletion width as compared to the devices used for the multiplication initiated by the pure injection of carriers. Furthermore, it indicates that future SAM APDs should be designed with a maximum electric field of $100\,\mathrm{kV\,cm^{-1}}$ in the absorber at the operating voltage.

While no GaInNAsSb/AlGaAs APD was fabricated in this study, the last chapter laid the groundwork for future SAM APDs by investigating GaAs/AlGaAs APDs. Using these devices, the correct doping and thickness of the charge sheet layer was verified without the additional complications of the dilute nitride absorber. Therefore, the same growth conditions of the grading layers and the AlGaAs charge sheet can be used in the GaInNAsSb/AlGaAs SAM APD growth run.

9.2 Future Work

In the future, there are several approaches that can be taken to further the scope of this study either focusing on the material aspect of GaInNAsSb or a device-orientated proposal.

The first approach would be to further the admittance spectroscopy analysis from this study to different annealing conditions based on full GaInNAsSb homojunction samples. This would allow for a more complete analysis regarding the annealing dependence of the defect type and concentration. Since the dark current and typical unintentional doping

concentration is still high and also inconsistent across growth runs, further defect analysis could be useful in improving future growth runs.

The second approach would take what we currently can achieve in GaInNAsSb and apply it further to device production. The first step would be to integrate the GaInNAsSb absorber with the SAM APD design. Since the design of the APD is solidified in chapter 8, the APD design shown in table 9.1 can be grown. An extra doping split with a concentration of $1.1 \times 10^{18}\,\mathrm{cm}^{-3}$ can be run which will decrease the punch-through voltage and increase the breakdown voltage. This will achieve a greater depletion width in the absorber at the expense of a higher electric field in the dilute nitride layer, approximately $190\,\mathrm{kV\,cm}^{-1}$ at breakdown. The remaining work would be centred around the annealing condition required to force the absorber to switch to p-type but with low unintentional doping concentration and dark current. If the growth of the GaInNAsSb layer is similar to the 1.0 µm devices of campaign 4, annealing at 730 °C is most likely the most optimal temperature.

Layer	Material	Thickness (nm)	Doping (cm^{-3})	
Contact	GaAs	100	p	5.0×10^{18}
Cladding	GaAs	200	p	1.0×10^{18}
Absorber	GaInNAsSb	1000	UID (p)	-
Grading 1	GaAs	50	p	2.0×10^{17}
Grading 2	$Al_{0.4}Ga_{0.6}As$	40	p	2.0×10^{17}
Charge Sheet	$Al_{0.8}Ga_{0.2}As$	25	p	Nominal: 1.3×10^{18} / Split: 1.1×10^{18}
Multiplication	$Al_{0.8}Ga_{0.2}As$	50	UID	-
Cladding	$Al_{0.8}Ga_{0.2}As$	250	n	1.0×10^{18}
Contact	GaAs	1000	n	5.0×10^{18}
Semi-Insulating GaAs Substrate				

Table 9.1: The design of the planned GaInNAsSb/AlGaAs APD with the inclusion of a charge sheet doping split intended to decrease the punch-through voltage.

Another approach would be to utilise GaAs/AlAs DBR mirrors to create RCE-PDs. With a bulk GaInNAsSb layer that is capable of absorption at 1.55 µm, very large responsivities would be achievable. Currently, RCE-PDs operating at 1.55 µm rely on quantum well structures which due to the small absorption width have limited responsivity. Furthermore, the resonant cavity could be integrated with other approaches such

as the APD or high speed detector to fully take advantage of the GaAs substrate.

Bibliography

[1] M. Razeghi and A. Rogalski, "Semiconductor ultraviolet detectors," *Journal of Applied Physics*, vol. 79, pp. 7433–7473, may 1996.

[2] S. S. Murtaza, R. V. Chelakara, R. D. Dupuis, J. C. Campbell, and A. G. Dentai, "Resonant-cavity photodiode operating at 1.55 µm with Burstein-shifted $In_{0.53}Ga_{0.47}As$/InP reflectors," *Applied Physics Letters*, vol. 69, pp. 2462–2464, oct 1996.

[3] I. Kimukin, N. Biyikli, B. Butun, O. Aytur, S. Unlu, and E. Ozbay, "InGaAs-based high-performance p-i-n photodiodes," *IEEE Photonics Technology Letters*, vol. 14, pp. 366–368, mar 2002.

[4] A. Jasik, J. Gaca, M. Wójcik, J. Muszalski, K. Pierściński, K. Mazur, M. Kosmala, and M. Bugajski, "Characterization of (Al)GaAs/AlAs distributed Bragg mirrors grown by MBE and LP MOVPE techniques," *Journal of Crystal Growth*, vol. 310, no. 18, pp. 4094–4101, 2008.

[5] B. Ng, J. David, S. Plimmer, G. Rees, R. Tozer, M. Hopkinson, and G. Hill, "Avalanche multiplication characteristics of Al/sub 0.8/Ga/sub 0.2/As diodes," *IEEE Transactions on Electron Devices*, vol. 48, no. 10, pp. 2198–2204, 2001.

[6] J. S. Harris, "GaInNAs long-wavelength lasers: progress and challenges," *Semiconductor Science and Technology*, vol. 17, pp. 880–891, aug 2002.

[7] K. Volz, D. Lackner, I. Németh, B. Kunert, W. Stolz, C. Baur, F. Dimroth, and A. W. Bett, "Optimization of annealing conditions of (GaIn)(NAs) for solar cell applications," *Journal of Crystal Growth*, vol. 310, no. 7-9, pp. 2222–2228, 2008.

[8] P. J. Klar, H. Grüning, J. Koch, S. Schäfer, K. Volz, W. Stolz, W. Heimbrodt, A. M. K. Saadi, A. Lindsay, and E. P. O'Reilly, "(Ga, In)(N, As)-fine structure

of the band gap due to nearest-neighbor configurations of the isovalent nitrogen," *Physical Review B*, vol. 64, p. 121203, sep 2001.

[9] W. Shan, W. Walukiewicz, J. Ager, E. Haller, J. Geisz, D. Friedman, J. Olson, and S. Kurtz, "Band Anticrossing in GaInNAs Alloys," *Physical Review Letters*, vol. 82, no. 6, pp. 1221–1224, 1999.

[10] I. Vurgaftman and J. R. Meyer, "Band parameters for nitrogen-containing semiconductors," *Journal of Applied Physics*, vol. 94, no. 6, pp. 3675–3696, 2003.

[11] A. Aho, V.-M. Korpijärvi, R. Isoaho, P. Malinen, A. Tukiainen, M. Honkanen, and M. Guina, "Determination of composition and energy gaps of GaInNAsSb layers grown by MBE," *Journal of Crystal Growth*, vol. 438, pp. 49–54, 2016.

[12] Y. T. Lin, T. C. Ma, T. Y. Chen, and H. H. Lin, "Energy gap reduction in dilute nitride GaAsSbN," *Applied Physics Letters*, vol. 93, no. 17, pp. 1–4, 2008.

[13] S. G. Spruytte, C. W. Coldren, J. S. Harris, W. Wampler, P. Krispin, K. Ploog, and M. C. Larson, "Incorporation of nitrogen in nitride-arsenides: Origin of improved luminescence efficiency after anneal," *Journal of Applied Physics*, vol. 89, pp. 4401–4406, apr 2001.

[14] S. Sze, *Physics of Semiconductors*. Wiley, 2007.

[15] W. K. Loke, S. F. Yoon, S. Wicaksono, K. H. Tan, and K. L. Lew, "Defect-induced trap-assisted tunneling current in GaInNAs grown on GaAs substrate," *Journal of Applied Physics*, vol. 102, no. 5, 2007.

[16] E. Rosencher, B. Vinter, and P. Piva, *Optoelectronics*. Cambridge University Press, 2002.

[17] C. W. Greeff and H. R. Glyde, "Anomalous Urbach tail in GaAs," *Physical Review B*, vol. 51, no. 3, pp. 1778–1783, 1995.

[18] S. R. Johnson and T. Tiedje, "Temperature dependence of the Urbach edge in GaAs," *Journal of Applied Physics*, vol. 78, no. 9, pp. 5609–5613, 1995.

[19] D. Aspnes, "Recombination at semiconductor surfaces and interfaces," *Surface Science*, vol. 132, pp. 406–421, sep 1983.

[20] S. Adachi, "Optical dispersion relations for GaP, GaAs, GaSb, InP, InAs, InSb, $Al_xGa_{1-x}As$, and $In_{1-x}Ga_xAs_yP_{1-y}$," *Journal of Applied Physics*, vol. 66, pp. 6030–6040, dec 1989.

[21] S. Adachi, *Physical Properties of III-V Semiconductor compounds*. John Wiley and Sons, 1992.

[22] A. Ghosal, D. Chattopadhyay, and N. N. Purkait, "Hot-electron velocity overshoot in $Ga_{0.47}In_{0.53}As$," *Applied Physics Letters*, vol. 44, no. 8, pp. 773–774, 1984.

[23] T. Ishibashi, T. Furuta, H. Fushimi, and H. Ito, "Photoresponse characteristics of uni-traveling-carrier photodiodes," in *Physics and Simulation of Optoelectronic Devices IX* (Y. Arakawa, P. Blood, and M. Osinski, eds.), vol. 4283, p. 469, jul 2001.

[24] S. Fedderwitz, A. Stohr, K. H. Tan, S. F. Yoon, M. Weib, A. Poloczek, W. K. Loke, S. Wicaksono, T. K. Ng, V. Rymanov, A. Patra, E. Tangdiongga, and D. Jager, "1.3 µm GaNAsSb–GaAs UTC-Photodetectors for 10-Gigabit Ethernet Links," *IEEE Photonics Technology Letters*, vol. 21, pp. 911–913, jul 2009.

[25] N. Balkan, A. Erol, F. Sarcan, L. F. Al-Ghuraibawi, and M. S. Nordin, "Dilute nitride resonant cavity enhanced photodetector with internal gain for the $\lambda \sim 1.3\,\mu m$ optical communications window," *Superlattices and Microstructures*, vol. 86, pp. 467–471, 2015.

[26] D. S. Ong, K. F. Li, G. J. Rees, J. P. R. David, and P. N. Robson, "A simple model to determine multiplication and noise in avalanche photodiodes," *Journal of Applied Physics*, vol. 83, pp. 3426–3428, mar 1998.

[27] Y. G. Wey, D. L. Crawford, K. Giboney, J. E. Bowers, M. J. Rodwell, P. Silvestre, M. J. Hafich, and G. Y. Robinson, "Ultrafast graded double-heterostructure GaInAs/InP photodiode," *Applied Physics Letters*, vol. 58, pp. 2156–2158, may 1991.

[28] J. Bowers, C. Burrus, and R. McCoy, "InGaAs PIN photodetectors with modulation response to millimetre wavelengths," *Electronics Letters*, vol. 21, no. 18, p. 812, 1985.

[29] Ock Kim, B. Dutt, R. McCoy, and J. Zuber, "A low dark-current, planar InGaAs p-i-n photodiode with a quaternary InGaAsP cap layer," *IEEE Journal of Quantum Electronics*, vol. 21, pp. 138–143, feb 1985.

[30] Https://www.osioptoelectronics.com/Libraries/Datasheets/FCI-InGaAs-36C.sflb.ashx, "OSI Optoelectronics 10 Gbps InGaAs photodiode."

[31] N. Shimizu, N. Watanabe, T. Furuta, and T. Ishibashi, "InP-InGaAs uni-traveling-carrier photodiode with improved 3-dB bandwidth of over 150 GHz," *IEEE Photonics Technology Letters*, vol. 10, pp. 412–414, mar 1998.

[32] J.-W. Shi, Y.-S. Wu, C.-Y. Wu, P.-H. Chiu, and C.-C. Hong, "High-speed, high-responsivity, and high-power performance of near-ballistic uni-traveling-carrier photodiode at 1.55 µm wavelength," *IEEE Photonics Technology Letters*, vol. 17, pp. 1929–1931, sep 2005.

[33] K. Kato, A. Kozen, Y. Muramoto, Y. Itaya, T. Nagatsuma, and M. Yaita, "110-GHz, 50%-efficiency mushroom-mesa waveguide p-i-n photodiode for a 1.55 µm wavelength," *IEEE Photonics Technology Letters*, vol. 6, pp. 719–721, jun 1994.

[34] H.-G. Bach, A. Beling, G. Mekonnen, R. Kunkel, D. Schmidt, W. Ebert, A. Seeger, M. Stollberg, and W. Schlaak, "InP-Based Waveguide-Integrated Photodetector With 100-GHz Bandwidth," *IEEE Journal of Selected Topics in Quantum Electronics*, vol. 10, pp. 668–672, jul 2004.

[35] Http://www.ioffe.ru/SVA/NSM/Semicond/, "NSM Archive - Physical Properties of Semiconductors."

[36] M. J. Mondry, D. I. Babic, J. E. Bowers, and L. A. Coldren, "Refractive Indexes of (Al, Ga, In)As Epilayers on InP for Optoelectronic Applications," *IEEE Photonics Technology Letters*, vol. 4, no. 6, pp. 627–630, 1992.

[37] H. Huang, Y. Huang, X. Wang, Q. Wang, and X. Ren, "Long Wavelength Resonant Cavity Photodetector Based on InP/Air-Gap Bragg Reflectors," *IEEE Photonics Technology Letters*, vol. 16, no. 1, pp. 245–247, 2004.

[38] N. Susa, H. Nakagome, O. Mikami, H. Ando, and H. Kanbe, "New InGaAs/InP avalanche photodiode structure for the 1-1.6 µm wavelength region," *IEEE Journal of Quantum Electronics*, vol. 16, pp. 864–870, aug 1980.

[39] G. Kinsey, J. Campbell, and A. Dentai, "Waveguide avalanche photodiode operating at 1.55 µm with a gain-bandwidth product of 320 GHz," *IEEE Photonics Technology Letters*, vol. 13, pp. 842–844, aug 2001.

[40] M. Lahrichi, G. Glastre, E. Derouin, D. Carpentier, N. Lagay, J. Decobert, and M. Achouche, "240-GHz Gain-Bandwidth Product Back-Side Illuminated AlInAs Avalanche Photodiodes," *IEEE Photonics Technology Letters*, vol. 22, pp. 1373–1375, sep 2010.

[41] Y. L. Goh, D. J. Massey, A. R. J. Marshall, J. S. Ng, C. H. Tan, W. K. Ng, G. J. Rees, M. Hopkinson, J. P. R. David, and S. K. Jones, "Avalanche multiplication in InAlAs," *IEEE Trans. Electron Devices*, vol. 54, no. 1, p. 11, 2007.

[42] J. Xie, S. Xie, R. C. Tozer, and C. H. Tan, "Excess Noise Characteristics of Thin AlAsSb APDs," *IEEE Transactions on Electron Devices*, vol. 59, pp. 1475–1479, may 2012.

[43] X. Yi, S. Xie, B. Liang, L. W. Lim, J. S. Cheong, M. C. Debnath, D. L. Huffaker, C. H. Tan, and J. P. David, "Extremely low excess noise and high sensitivity $AlAs_{0.56}Sb_{0.44}$ avalanche photodiodes," *Nature Photonics*, vol. 13, no. October, 2019.

[44] M. E. Woodson, M. Ren, S. J. Maddox, Y. Chen, S. R. Bank, and J. C. Campbell, "Low-noise AlInAsSb avalanche photodiode," *Applied Physics Letters*, vol. 108, p. 081102, feb 2016.

[45] S. R. Bank, J. C. Campbell, S. J. Maddox, M. Ren, A.-k. Rockwell, M. E. Woodson, and S. D. March, "Avalanche Photodiodes Based on the AlInAsSb Materials System," *IEEE Journal of Selected Topics in Quantum Electronics*, vol. 24, no. 2, 2018.

[46] M. Jutzi, M. Berroth, G. Wöhl, M. Oehme, and E. Kasper, "Ge-on-Si vertical incidence photodiodes with 39-GHz bandwidth," *IEEE Photonics Technology Letters*, vol. 17, no. 7, pp. 1510–1512, 2005.

[47] J. Liu, J. Michel, W. Giziewicz, D. Pan, K. Wada, D. D. Cannon, S. Jongthammanurak, D. T. Danielson, L. C. Kimerling, J. Chen, F. Ö. Ilday, F. X. Kärtner, and J. Yasaitis, "High-performance, tensile-strained Ge p-i-n photodetectors on a Si platform," *Applied Physics Letters*, vol. 87, no. 10, pp. 75–78, 2005.

[48] H. H. Tseng, H. Li, V. Mashanov, Y. J. Yang, H. H. Cheng, G. E. Chang, R. A. Soref, and G. Sun, "GeSn-based p-i-n photodiodes with strained active layer on a Si wafer," *Applied Physics Letters*, vol. 103, p. 231907, dec 2013.

[49] T. Yin, R. Cohen, M. M. Morse, G. Sarid, Y. Chetrit, D. Rubin, and M. J. Paniccia, "31 GHz Ge n-i-p waveguide photodetectors on Silicon-on-Insulator substrate," *Optics Express*, vol. 15, no. 21, p. 13965, 2007.

[50] L. Vivien, A. Polzer, D. Marris-Morini, J. Osmond, J. M. Hartmann, P. Crozat, E. Cassan, C. Kopp, H. Zimmermann, and J. M. Fédéli, "Zero-bias 40Gbit/s germanium waveguide photodetector on silicon," *Optics Express*, vol. 20, no. 2, p. 1096, 2012.

[51] Y. Kang, H.-D. Liu, M. Morse, M. J. Paniccia, M. Zadka, S. Litski, G. Sarid, A. Pauchard, Y.-H. Kuo, H.-W. Chen, W. S. Zaoui, J. E. Bowers, A. Beling, D. C. McIntosh, X. Zheng, and J. C. Campbell, "Monolithic germanium/silicon avalanche photodiodes with 340 GHz gain–bandwidth product," *Nature Photonics*, vol. 3, pp. 59–63, jan 2009.

[52] M. Huang, S. Li, P. Cai, G. Hou, T. I. Su, W. Chen, C. Y. Hong, and D. Pan, "Germanium on silicon avalanche photodiode," *IEEE Journal of Selected Topics in Quantum Electronics*, vol. 24, no. 2, 2018.

[53] D. Liang, G. Roelkens, R. Baets, and J. Bowers, "Hybrid Integrated Platforms for Silicon Photonics," *Materials*, vol. 3, pp. 1782–1802, mar 2010.

[54] B. F. Levine, A. R. Hawkins, S. Hiu, B. J. Tseng, C. A. King, L. A. Gruezke, R. W. Johnson, D. R. Zolnowski, and J. E. Bowers, "20 GHz high performance planar Si/InGaAs p-i-n photodetector," *Applied Physics Letters*, vol. 70, pp. 2449–2451, may 1997.

[55] A. Salvador, F. Huang, B. Sverdlov, A. Botchkarev, and H. Morcoç, "InP/InGaAs resonant cavity enhanced photodetector and light emitting diode with external mirrors on Si," *Electronics Letters*, vol. 30, pp. 1527–1529, sep 1994.

[56] A. R. Hawkins, W. Wu, P. Abraham, K. Streubel, and J. E. Bowers, "High gain-bandwidth-product silicon heterointerface photodetector," *Applied Physics Letters*, vol. 70, no. 3, pp. 303–305, 1997.

[57] D. Pasquariello and K. Hjort, "Plasma-assisted InP-to-Si low temperature wafer bonding," *IEEE Journal of Selected Topics in Quantum Electronics*, vol. 8, no. 1, pp. 118–131, 2002.

[58] Z. Bin, H. Qin, Y. Xiao-Hong, N. Hai-Qiao, H. Ji-Fang, N. Zhi-Chuan, W. Xin, W. Xiu-Ping, and W. Jie, "Metamorphic InGaAs p-i-n Photodetectors with 1.75 µm Cut-Off Wavelength Grown on GaAs," *Chinese Physics Letters*, vol. 27, p. 038504, mar 2010.

[59] J. Jang, G. Cueva, D. Dumka, W. Hoke, P. Lemonias, and I. Adesida, "Long-wavelength $In_{0.53}Ga_{0.47}As$ metamorphic p-i-n photodiodes on GaAs substrates," *IEEE Photonics Technology Letters*, vol. 13, no. 2, pp. 151–153, 2001.

[60] S. Huang, G. Balakrishnan, and D. L. Huffaker, "Interfacial misfit array formation for GaSb growth on GaAs," *Journal of Applied Physics*, vol. 105, p. 103104, may 2009.

[61] S. H. Huang, G. Balakrishnan, A. Khoshakhlagh, A. Jallipalli, L. R. Dawson, and D. L. Huffaker, "Strain relief by periodic misfit arrays for low defect density GaSb on GaAs," *Applied Physics Letters*, vol. 88, no. 13, 2006.

[62] A. P. Craig, C. J. Reyner, A. R. J. Marshall, and D. L. Huffaker, "Excess noise in GaAs and AlGaAs avalanche photodiodes with GaSb absorption regions—composite structures grown using interfacial misfit arrays," *Applied Physics Letters*, vol. 104, p. 213502, may 2014.

[63] M. Kondow, K. Uomi, A. Niwa, T. Kitatani, S. Watahiki, and Y. Yazawa, "GaInNAs: A novel material for long-wavelength-range laser diodes with excellent high-temperature performance," *Japanese Journal of Applied Physics, Part 1: Regular Papers and Short Notes and Review Papers*, vol. 35, no. 2 SUPPL. B, pp. 1273–1275, 1996.

[64] M. Guina, S. M. Wang, and A. Aho, "Molecular Beam Epitaxy of Dilute Nitride Optoelectronic Devices," in *Molecular Beam Epitaxy*, pp. 73–94, Elsevier, 2018.

[65] J. Harris, H. Yuen, S. Bank, M. Wistey, V. Lordi, T. Gugov, H. Bae, and L. Goddard, "MBE Growth and Characterization of Long Wavelength Dilute Nitride III–V Alloys," in *Dilute Nitride Semiconductors*, pp. 1–92, 2005.

[66] M. A. Wistey, S. R. Bank, H. B. Yuen, H. Bae, and J. S. Harris, "Nitrogen plasma optimization for high-quality dilute nitrides," *Journal of Crystal Growth*, vol. 278, pp. 229–233, may 2005.

[67] V. Lordi, V. Gambin, S. Friedrich, T. Funk, T. Takizawa, K. Uno, and J. S. Harris, "Nearest-Neighbor Configuration in (GaIn)(NAs) Probed by X-Ray Absorption Spectroscopy," *Physical Review Letters*, vol. 90, no. 14, p. 145505, 2003.

[68] S. Kurtz, J. Webb, L. Gedvilas, D. Friedman, J. Geisz, J. Olson, R. King, D. Joslin, and N. Karam, "Structural changes during annealing of GaInAsN," *Applied Physics Letters*, vol. 78, no. 6, pp. 748–750, 2001.

[69] V. Riede, H. Neumann, H. Sobotta, R. Schwabe, W. Seifert, and S. Schwetlick, "The Localized Vibrational Mode of Nitrogen in GaAs," *physica status solidi (a)*, vol. 93, pp. K151–K156, feb 1986.

[70] W. K. Loke, S. F. Yoon, S. Z. Wang, T. K. Ng, and W. J. Fan, "Rapid thermal annealing of GaN_xAs_{1-x} grown by radio-frequency plasma assisted molecular beam epitaxy and its effect on photoluminescence," *Journal of Applied Physics*, vol. 91, pp. 4900–4903, apr 2002.

[71] E. Tournié and M. A. Pinault, "Mechanisms affecting the photoluminescence spectra of GaInNAs after post-growth annealing," *Applied Physics Letters*, vol. 80, no. 22, pp. 4148–4150, 2002.

[72] Y. Sun, Z. Cheng, Q. Zhou, Y. Sun, J. Sun, Y. Liu, M. Wang, Z. Cao, Z. Ye, M. Xu, Y. Ding, P. Chen, M. Heuken, and T. Egawa, "Redshift and blueshift of GaNAs/GaAs multiple quantum wells induced by rapid thermal annealing," *Journal of Crystal Growth*, vol. 483, pp. 190–194, 2018.

[73] H. Luo, J. A. Gupta, and H. C. Liu, "1.55 µm GaNAsSb photodetector on GaAs," *Applied Physics Letters*, vol. 86, p. 211121, may 2005.

[74] T. Garrod, J. Kirch, P. Dudley, S. Kim, L. Mawst, and T. Kuech, "Narrow band gap GaInNAsSb material grown by metal organic vapor phase epitaxy (MOVPE) for solar cell applications," *Journal of Crystal Growth*, vol. 315, pp. 68–73, jan 2011.

[75] X. Yang, J. B. Heroux, M. J. Jurkovic, and W. I. Wang, "High-temperature characteristics of 1.3 µm InGaAsN:Sb/GaAs multiple-quantum-well lasers grown by molecular-beam epitaxy," *Applied Physics Letters*, vol. 76, pp. 795–797, feb 2000.

[76] X. Yang, M. J. Jurkovic, J. B. Heroux, and W. I. Wang, "Molecular beam epitaxial growth of InGaAsN:Sb/GaAs quantum wells for long-wavelength semiconductor lasers," *Applied Physics Letters*, vol. 75, pp. 178–180, jul 1999.

[77] H. B. Yuen, S. R. Bank, H. Bae, M. A. Wistey, and J. S. Harris, "The role of antimony on properties of widely varying GaInNAsSb compositions," *Journal of Applied Physics*, vol. 99, p. 093504, may 2006.

[78] R. Isoaho, A. Aho, A. Tukiainen, T. Aho, M. Raappana, T. Salminen, J. Reuna, and M. Guina, "Photovoltaic properties of low-bandgap (0.7-0.9 eV) lattice-matched GaInNAsSb solar junctions grown by molecular beam epitaxy on GaAs," *Solar Energy Materials and Solar Cells*, vol. 195, pp. 198–203, jun 2019.

[79] J. S. Harris, R. Kudrawiec, H. B. Yuen, S. R. Bank, H. P. Bae, M. A. Wistey, D. Jackrel, E. R. Pickett, T. Sarmiento, L. L. Goddard, V. Lordi, and T. Gugov, "Development of GaInNAsSb alloys: Growth, band structure, optical properties and applications," *physica status solidi (b)*, vol. 244, pp. 2707–2729, aug 2007.

[80] J. Geisz, D. Friedman, J. Olson, S. Kurtz, and B. Keyes, "Photocurrent of 1eV GaInNAs lattice-matched to GaAs," *Journal of Crystal Growth*, vol. 195, pp. 401–408, dec 1998.

[81] V. Polojärvi, A. Aho, A. Tukiainen, A. Schramm, and M. Guina, "Comparative study of defect levels in GaInNAs, GaNAsSb, and GaInNAsSb for high-efficiency solar cells," *Applied Physics Letters*, vol. 108, no. 12, pp. 1–6, 2016.

[82] A. J. Ptak, D. J. Friedman, and S. Kurtz, "Effects of temperature, nitrogen ions, and antimony on wide depletion width GaInNAs," *Journal of Vacuum Science & Technology B: Microelectronics and Nanometer Structures*, vol. 25, no. 3, p. 955, 2007.

[83] F. Langer, S. Perl, S. Höfling, and M. Kamp, "p- to n-type conductivity transition in 1.0 eV GaInNAs solar cells controlled by the V/III ratio," *Applied Physics Letters*, vol. 106, p. 063905, feb 2015.

[84] S. Kurtz, J. F. Geisz, D. J. Friedman, W. K. Metzger, R. R. King, and N. H. Karam, "Annealing-induced-type conversion of GaInNAs," *Journal of Applied Physics*, vol. 95, pp. 2505–2508, mar 2004.

[85] S. Y. Xie, S. F. Yoon, and S. Z. Wang, "Effects of thermal annealing on deep-level defects and minority-carrier electron diffusion length in Be-doped InGaAsN," *Journal of Applied Physics*, vol. 97, p. 073702, apr 2005.

[86] P. Krispin, S. G. Spruytte, J. S. Harris, and K. H. Ploog, "Electron traps in Ga(As,N) layers grown by molecular-beam epitaxy," *Applied Physics Letters*, vol. 80, pp. 2120–2122, mar 2002.

[87] J. B. Héroux, X. Yang, and W. I. Wang, "GalnNAs resonant-cavity-enhanced photodetector operating at 1.3 µm," *Applied Physics Letters*, vol. 75, no. 18, pp. 2716–2718, 1999.

[88] Q. Han, X. H. Yang, Z. C. Niu, H. Q. Ni, Y. Q. Xu, S. Y. Zhang, Y. Du, L. H. Peng, H. Zhao, C. Z. Tong, R. H. Wu, and Q. M. Wang, "1.55 µm GaInNAs resonant-cavity-enhanced photodetector grown on GaAs," *Applied Physics Letters*, vol. 87, p. 111105, sep 2005.

[89] S. L. Tan, S. Zhang, W. M. Soong, Y. L. Goh, L. J. J. Tan, J. S. Ng, J. P. R. David, I. P. Marko, A. R. Adams, S. J. Sweeney, and J. Allam, "GaInNAsSb/GaAs Photodiodes for Long-Wavelength Applications," *IEEE Electron Device Letters*, vol. 32, pp. 919–921, jul 2011.

[90] W. K. Loke, S. F. Yoon, Z. Xu, K. H. Tan, T. K. Ng, Y. K. Sim, S. Wicaksono, N. Saadsaoud, D. Decoster, and J. Chazelas, "GaNAsSb/GaAs waveguide photodetector with response up to 1.6 µm grown by molecular beam epitaxy," *Applied Physics Letters*, vol. 93, p. 081102, aug 2008.

[91] Z. Xu, N. Saadsaoud, M. Zegaoui, W. K. Loke, K. H. Tan, S. Wicaksono, S. F. Yoon, C. Legrand, D. Decoster, and J. Chazelas, "DC Performance of High-Quantum-Efficiency 1.3 µm GaNAsSb / GaAs Waveguide Photodetector," *IEEE Electron Device Letters*, vol. 31, no. 5, pp. 449–451, 2010.

[92] M. Zegaoui, Z. Xu, N. Saadsaoud, K. H. Tan, W. K. Loke, S. Wicaksono, S. F. Yoon, C. Legrand, D. Decoster, and J. Chazelas, "High-Speed 1.3 µm p-i-n GaNAsSb/GaAs Waveguide Photodetector," *IEEE Electron Device Letters*, vol. 31, pp. 704–706, jul 2010.

[93] S. L. Tan, W. M. Soong, M. J. Steer, S. Zhang, J. S. Ng, and J. P. R. David, "Dilute nitride GaInNAs and GaInNAsSb for solar cell applications," *Spie Opto*, vol. 8256, p. 82561E, 2012.

[94] K. H. Tan, S. F. Yoon, W. K. Loke, S. Wicaksono, K. L. Lew, A. Stöhr, O. Ecin, A. Poloczek, A. Malcoci, and D. Jäger, "High-speed picosecond pulse response GaNAsSb p-i-n photodetectors grown by rf plasma-assisted nitrogen molecular beam epitaxy," *Applied Physics Letters*, vol. 90, p. 183515, apr 2007.

[95] L. J. J. Tan, W. M. Soong, J. P. R. David, and J. S. Ng, "Dark Current Mechanism in Bulk GaInNAs Lattice Matched to GaAs," *IEEE Transactions on Electron Devices*, vol. 58, pp. 103–106, jan 2011.

[96] A. R. Adams, "Band-structure engineering to control impact ionisation and related high-field processes," *Electronics Letters*, vol. 40, no. 17, 2004.

[97] G. S. Kinsey, D. W. Gotthold, A. L. Holmes, B. G. Streetman, and J. C. Campbell, "GaNAs avalanche photodiode operating at 0.94 µm," *Applied Physics Letters*, vol. 76, pp. 2824–2825, may 2000.

[98] S. L. Tan, W. M. Soong, J. E. Green, M. J. Steer, S. Zhang, L. J. J. Tan, J. S. Ng, I. P. Marko, S. J. Sweeney, A. R. Adams, J. Allam, and J. P. R. David, "Experimental evaluation of impact ionization in dilute nitride GaInNAs diodes," *Applied Physics Letters*, vol. 103, p. 102101, sep 2013.

[99] X. G. Zheng, X. Sun, S. Wang, P. Yuan, G. S. Kinsey, A. L. Holmes, B. G. Streetman, and J. C. Campbell, "Multiplication noise of $Al_xGa_{1-x}As$ avalanche photodiodes with high Al concentration and thin multiplication region," *Applied Physics Letters*, vol. 78, pp. 3833–3835, jun 2001.

[100] B. Ng, J. David, R. Tozer, M. Hopkinson, G. Hill, and G. Rees, "Excess noise characteristics of $Al_{0.8}Ga_{0.2}As$ avalanche photodiodes," *IEEE Photonics Technology Letters*, vol. 14, pp. 522–524, apr 2002.

[101] Y. Lu, T. Kalkur, and C. Paz de Araujo, "Rapid thermal alloyed ohmic contacts to p-type GaAs," *Journal of the Electrochemical Society*, vol. 136, no. 10, pp. 3123–3129, 1989.

[102] Y. C. Shih, M. Murakami, E. L. Wilkie, and A. C. Callegari, "Effects of interfacial microstructure on uniformity and thermal stability of AuNiGe ohmic contact to n-type GaAs," *Journal of Applied Physics*, vol. 62, no. 2, pp. 582–590, 1987.

[103] A. Baca, F. Ren, J. Zolper, R. Briggs, and S. Pearton, "A survey of ohmic contacts to III-V compound semiconductors," *Thin Solid Films*, vol. 308, pp. 599–606, 1997.

[104] H. J. Bühlmann and M. Ilegems, "Characterization of AuGe/Ni/Au Contacts on GaAs/AlGaAs Heterostructures for Low-Temperature Applications," *Journal of The Electrochemical Society*, vol. 138, no. 9, p. 2795, 1991.

[105] D. W. Shaw, "Localized GaAs Etching with Acidic Hydrogen Peroxide Solutions," *Journal of The Electrochemical Society*, vol. 128, no. 4, p. 874, 1981.

[106] Bruker, *VERTEX 70 User Manual*. 6th ed., 2013.

[107] J. Martín and M. Sánchez, "Refractive index expressions for $Ga_{1-x}ln_xAs$, $GaAs_{1-x}N_x$ and $Ga_{1-x}ln_xN_yAs_{1-y}$ alloys," *Revista Mexicana de Fisica*, vol. 61, no. August, pp. 245–253, 2015.

[108] T. Kitatani, M. Kondow, K. Shinoda, Y. Yazawa, and M. Okai, "Characterization of the Refractive Index of Strained GaInNAs Layers by Spectroscopic Ellipsometry," *Japanese Journal of Applied Physics*, vol. 37, no. 1, 1998.

[109] Y. P. Varshni, "Temperature dependence of the energy gap in semiconductors," *Physica*, vol. 34, no. 1, pp. 149–154, 1967.

[110] L. Gupta, S. Rath, S. C. Abbi, and F. C. Jain, "Temperature dependence of the fundamental band gap parameters in cadmium-rich $Zn_xCd_{1-x}Se$ using photoluminescence spectroscopy," *Pramana - Journal of Physics*, vol. 61, no. 4, pp. 729–737, 2003.

[111] D. K. Schroder, *Semiconductor Material and Device Characterization*. Wiley - IEEE, Wiley, 2015.

[112] D. L. Losee, "Admittance spectroscopy of impurity levels in Schottky barriers," *Journal of Applied Physics*, vol. 46, pp. 2204–2214, may 1975.

[113] T. Walter, R. Herberholz, C. Müller, and H. W. Schock, "Determination of defect distributions from admittance measurements and application to $Cu(In,Ga)Se_2$

based heterojunctions," *Journal of Applied Physics*, vol. 80, pp. 4411–4420, oct 1996.

[114] Y. He, N. Miyashita, and Y. Okada, "N–H-related deep-level defects in dilute nitride semiconductor GaInNAs for four-junction solar cells," *Japanese Journal of Applied Physics*, vol. 57, p. 08RD11, aug 2018.

[115] M. Monirul Islam, N. Miyashita, N. Ahsan, T. Sakurai, K. Akimoto, and Y. Okada, "Identification of defect types in moderately Si-doped GaInNAsSb layer in p-GaAs/n- GaInNAsSb/n-GaAs solar cell structure using admittance spectroscopy," *Journal of Applied Physics*, vol. 112, no. 11, 2012.

[116] H. C. Casey, D. D. Sell, and K. W. Wecht, "Concentration dependence of the absorption coefficient for n- and p-type GaAs between 1.3 and 1.6 eV," *Journal of Applied Physics*, vol. 46, no. 1, pp. 250–257, 1975.

[117] D. J. Massey, J. P. David, and G. J. Rees, "Temperature dependence of avalanche multiplication in submicron silicon devices," *Proceedings of ESSDERC 2005: 35th European Solid-State Device Research Conference*, vol. 2005, pp. 245–248, 2005.

[118] M. H. Woods, W. C. Johnson, and M. A. Lampert, "Use of a Schottky-Barrier To Measure Impact Ionization Coefficients in Semiconductors," *Solid-State Electronics*, vol. 16, no. 3, pp. 381–394, 1973.

[119] N. Miyashita, Y. He, N. Ahsan, and Y. Okada, "Anneal mediated deep-level dynamics in GaInNAsSb dilute nitrides lattice-matched to GaAs," *Journal of Applied Physics*, vol. 126, p. 143104, oct 2019.

[120] S. L. Tan, C. J. Hunter, S. Zhang, L. J. J. Tan, Y. L. Goh, J. S. Ng, I. P. Marko, S. J. Sweeney, A. R. Adams, J. Allam, and J. P. R. David, "Improved optoelectronic properties of rapid thermally annealed dilute nitride GaInNAs photodetectors," *Journal of Electronic Materials*, vol. 41, no. 12, pp. 3393–3401, 2012.

[121] W. Loke, S. Yoon, S. Wicaksono, and B. Ng, "Characteristics of non-annealed λ=1.35μm closely lattice-matched GaInNAs/GaAs p-i-n photodetector structures grown by solid-source molecular beam epitaxy," *Materials Science and Engineering: B*, vol. 131, pp. 40–44, jul 2006.

[122] U. Tisch, E. Finkman, and J. Salzman, "The anomalous bandgap bowing in GaAsN," *Applied Physics Letters*, vol. 81, no. 3, pp. 463–465, 2002.

[123] B. Bansal, V. K. Dixit, V. Venkataraman, and H. L. Bhat, "Alloying induced degradation of the absorption edge of $InAs_xSb_{1-x}$," *Applied Physics Letters*, vol. 90, no. 10, 2007.

[124] S. Mazzucato, R. Potter, A. Erol, N. Balkan, P. Chalker, T. Joyce, T. Bullough, X. Marie, H. Carrère, E. Bedel, G. Lacoste, A. Arnoult, and C. Fontaine, "S-shaped behaviour of the temperature-dependent energy band gap in dilute nitrides," *Physica E: Low-dimensional Systems and Nanostructures*, vol. 17, pp. 242–244, apr 2003.

[125] K. Nunna, S. Iyer, L. Wu, J. Li, S. Bharatan, X. Wei, R. T. Senger, and K. K. Bajaj, "Nitrogen incorporation and optical studies of GaAsSbN / GaAs single quantum well heterostructures," *Journal of Applied Physics*, vol. 102, p. 053106, sep 2007.

[126] D. K. Gaskill, N. Bottka, L. Aina, and M. Mattingly, "Band-gap determination by photoreflectance of InGaAs and InAlAs lattice matched to InP," *Applied Physics Letters*, vol. 56, no. 13, pp. 1269–1271, 1990.

[127] K. Uesugi, I. Suemune, T. Hasegawa, T. Akutagawa, and T. Nakamura, "Temperature dependence of band gap energies of GaAsN alloys," *Applied Physics Letters*, vol. 76, pp. 1285–1287, mar 2000.

[128] N. Li, X. Li, S. Demiguel, X. Zheng, J. Campbell, D. Tulchinsky, K. Williams, T. Isshiki, G. Kinsey, and R. Sudharsansan, "High-Saturation-Current Charge-Compensated InGaAs–InP Uni-Traveling-Carrier Photodiode," *IEEE Photonics Technology Letters*, vol. 16, pp. 864–866, mar 2004.

[129] A. J. Ptak, S. W. Johnston, S. Kurtz, D. J. Friedman, and W. K. Metzger, "A comparison of MBE- and MOCVD-grown GaInNAs," *Journal of Crystal Growth*, vol. 251, pp. 392–398, 2003.

[130] S. R. Kurtz, J. F. Klem, A. A. Allerman, R. M. Sieg, C. H. Seager, and E. D. Jones, "Minority carrier diffusion and defects in InGaAsN grown by molecular beam epitaxy," *Applied Physics Letters*, vol. 80, no. 8, pp. 1379–1381, 2002.

[131] K. Yasuda, T. Shirai, Y. Kishi, S. Yamazaki, and T. Kaneda, "Heterojunction effect on spectral and frequency responses in InP/InGaAsP/InGaAs APD," *Japanese Journal of Applied Physics*, vol. 22, pp. 291–294, 1983.

[132] A. R. J. Marshall, C. H. Tan, J. P. R. David, J. S. Ng, and M. Hopkinson, "Fabrication of InAs photodiodes with reduced surface leakage current," in *Optical Materials in Defence Systems Technology IV* (J. G. Grote, F. Kajzar, and M. Lindgren, eds.), vol. 6740, p. 67400H, oct 2007.

[133] S. Wicaksono, S. F. Yoon, W. K. Loke, K. H. Tan, K. L. Lew, M. Zegaoui, J. P. Vilcot, D. Decoster, and J. Chazelas, "Effect of growth temperature on defect states of GaAsSbN intrinsic layer in GaAs/GaAsSbN/GaAs photodiode for 1.3 µm application," *Journal of Applied Physics*, vol. 102, p. 044505, aug 2007.

[134] D. B. Jackrel, S. R. Bank, H. B. Yuen, M. A. Wistey, J. S. Harris, A. J. Ptak, S. W. Johnston, D. J. Friedman, and S. R. Kurtz, "Dilute nitride GaInNAs and GaInNAsSb solar cells by molecular beam epitaxy," *Journal of Applied Physics*, vol. 101, no. 11, 2007.

[135] K. Decock, S. Khelifi, and M. Burgelman, "Accuracy of defect distributions measured by bias dependent admittance spectroscopy on thin film solar cells," in *2011 37th IEEE Photovoltaic Specialists Conference*, no. June 2011, pp. 001691–001694, IEEE, jun 2011.

[136] M. Seifikar, E. P. O'Reilly, and S. Fahy, "Theory of intermediate- and high-field mobility in dilute nitride alloys," *Physical Review B - Condensed Matter and Materials Physics*, vol. 84, no. 16, pp. 1–13, 2011.

[137] J. S. Ng, C. H. Tan, J. P. David, and G. J. Rees, "Effect of impact ionization in the InGaAs absorber on excess noise of avalanche photodiodes," *IEEE Journal of Quantum Electronics*, vol. 41, pp. 1092–1096, aug 2005.

[138] S. Fahy and E. P. O'Reilly, "Theory of electron mobility in dilute nitride semiconductors," *Physica E: Low-Dimensional Systems and Nanostructures*, vol. 21, no. 2-4, pp. 881–885, 2004.

[139] N. Miyashita, Y. Shimizu, and Y. Okada, "Carrier mobility characteristics in GaInNAs dilute nitride films grown by atomic hydrogen-assisted molecular beam epitaxy," *Journal of Applied Physics*, vol. 102, p. 044904, aug 2007.

[140] G. S. Kinsey, C. C. Hansing, A. L. Holmes, B. G. Streetman, J. C. Campbell, and A. G. Dentai, "Waveguide InGaAs–InAlAs Avalanche Photodiode," *IEEE Photonics Technology Letters*, vol. 12, no. 4, pp. 416–418, 2000.

[141] X. Collins, A. P. Craig, T. Roblin, and A. R. Marshall, "Impact ionisation in $Al_{0.9}Ga_{0.1}As_{0.08}Sb_{0.92}$ for Sb-based avalanche photodiodes," *Applied Physics Letters*, vol. 112, no. 2, pp. 0–4, 2018.

[142] J. S. Ng, C. H. Tan, J. P. R. David, G. Hill, and G. J. Rees, "Field Dependence of Impact Ionization Coefficients in $In_{0.53}Ga_{0.47}As$," *Ieee Transactions on Electron Devices*, vol. 50, no. 4, 2003.

[143] D. Ji, B. Ercan, and S. Chowdhury, "Experimental determination of impact ionization coefficients of electrons and holes in gallium nitride using homojunction structures," *Applied Physics Letters*, vol. 115, no. 7, 2019.

[144] L. W. Aukerman, M. F. Millea, and M. McColl, "Diffusion lengths of electrons and holes in GaAs," *Journal of Applied Physics*, vol. 38, no. 2, pp. 685–690, 1967.

[145] M. Ren, S. Maddox, Y. Chen, M. Woodson, J. C. Campbell, and S. Bank, "AlInAsSb/GaSb staircase avalanche photodiode," *Applied Physics Letters*, vol. 108, no. 8, 2016.